UNIVERSIDADE ESTADUAL PAULISTA
"JÚLIO DE MESQUITA FILHO"
CAMPUS DE GUARATINGUETÁ

MATEUS DIAS RIBEIRO

ENGINE LES WITH FUEL-SPRAY MODELING

Guaratinguetá
2015

MATEUS DIAS RIBEIRO

ENGINE LES WITH FUEL-SPRAY MODELING

Dissertação apresentada à Faculdade de Engenharia do Campus de Guaratinguetá, Universidade Estadual Paulista, para obtenção do título de Mestre em Engenharia Mecânica na área de Transmissão e Conversão de Energia.

Orientadores: Prof. Dr. Maurício Araújo Zanardi
Prof. Dr. José Antônio Perella Balestieri
Prof. Dr.-Ing. Andreas Kempf

Guaratinguetá
2015

Ribeiro, Mateus Dias

B484e

Engine LES with fuel-spray modeling / Mateus Dias Ribeiro. - Guaratinguetá, 2015

118 f .: il.
Bibliografia: f. 111-113

Dissertação (Mestrado) – Universidade Estadual Paulista, Faculdade de Engenharia de Guaratinguetá, 2015.

Orientador: Prof. Dr. Maurício Araújo Zanardi

Co-orientador: Prof. Dr. José Antônio Perrella Balestieri; Prof. Dr. Andreas Kempf

1. Motores de combustão interna 2. Atomização 3. Fluidodinâmica computacional 4. Aerossois I. Título

CDU 621.43

unesp

UNIVERSIDADE ESTADUAL PAULISTA
CAMPUS DE GUARATINGUETÁ

MATEUS DIAS RIBEIRO

ESTA DISSERTAÇÃO FOI JULGADA ADEQUADA PARA A OBTENÇÃO DO TÍTULO DE
"MESTRE EM ENGENHARIA MECÂNICA"

PROGRAMA: ENGENHARIA MECÂNICA
ÁREA: ENERGIA

APROVADA EM SUA FORMA FINAL PELO PROGRAMA DE PÓS-GRADUAÇÃO

Prof. Dr. Edson Cocchieri Botelho
Coordenador

BANCA EXAMINADORA:

Prof. Dr. MAURICIO ARAUJO ZANARDI
Orientador / Unesp-Feg

Prof. Dr. ALEX MENDONÇA BIMBATO
Unesp-Feg

Prof. Dr. MARCIO TEIXEIRA MENDONÇA
IAE/APA

Junho de 2015

DADOS CURRICULARES

MATEUS DIAS RIBEIRO

NASCIMENTO	08/11/1989 – FRUTAL / MG
FILIAÇÃO	UBIRATÃ LEAL RIBEIRO
	LILIANE DE MELO RIBEIRO
2008/2013	Curso de Graduação em Engenharia Mecânica, na Faculdade de Engenharia do Campus de Guaratinguetá da Universidade Estadual Paulista.
2013/2015	Curso de Pós-Graduação em Engenharia Mecânica, nível de mestrado, na Faculdade de Engenharia do Campus de Guaratinguetá da Universidade Estadual Paulista.

To my family

ACKNOWLEDGMENTS

First of all, I wish to deeply thank my research advisors in Brazil at UNESP, Prof. Maurício Araújo Zanardi and Prof. José Antônio Perrella Balestieri, for their valuable guidance and teaching. They are responsible for most of my interest in fluid dynamics and internal combustion engines, which led me to start this dissertation.

Also a huge thanks to my research advisors in Germany at the University of Duisburg-Essen, Prof. Andreas Kempf and Peter Janas, who shared their knowledge and computational resources, leading to a brilliant guidance, without which I would never be able to conduct this work.

Thanks to the colleagues at the Chair of Fluid Dynamics in Duisburg, for being always so kind, friendly and ready to help when I needed.

Thanks to Thyssenkrupp, especially to the engineers Rafael Aguera and Alex Rodrigues, for the guidance within this project and the financial support.

A special thanks to my parents, Ubiratã and Liliane, for supporting my decision of finishing my master studies in Germany and the education they gave me.

Last but not least, to everyone not mentioned here but who helped someway: Thanks for your support and for being part of my life.

“What we know is a drop, what we don’t know is an ocean.”

Sir Isaac Newton

RIBEIRO, M. D. **LES de Motor de Combustão Interna com Spray-Combustível.** 2015. 118 f. Dissertação (Mestrado em Engenharia Mecânica) – Faculdade de Engenharia do Campus de Guaratinguetá, Universidade Estadual Paulista, Guaratinguetá, 2015.

RESUMO

O motor de combustão interna é a principal fonte de energia de automóveis, sendo de grande importância para o setor de energia no mundo. Com o aparecimento de problemas relacionados com a emissão exagerada de poluentes e gases de efeito estufa, o desenvolvimento de modelos que corretamente descrevem os fenômenos físicos que ocorrem no interior da câmara de combustão de motores tornou-se relevante. Assim, na primeira parte deste trabalho a biblioteca de modelos de fonte aberta de dinâmica de fluidos computacional (CFD) OpenFOAM com módulos desenvolvidos na Universidade de Duisburg-Essen foi utilizada para investigar o efeito do volume das fendas no desenvolvimento da combustão em motores convencionais com ignição por centelha. As simulações de grandes escalas (LES, *large eddy simulation*) realizadas foram validadas com visualizações de câmeras de alta velocidade obtidas do motor óptico de Duisburg, que mostraram a presença de uma frente luminosa no interior da fenda anular que poderia ser associada a uma chama se propagando. Os resultados apresentados mostraram boa concordância qualitativa com os dados experimentais, o que permitiu concluir que no caso do motor de Duisburg, a chama é realmente capaz de penetrar no volume da fenda. Em seguida, um estudo sobre sprays combustíveis foi realizado, por se tratar de uma tendência muito promissora em motores modernos. Atenção especial foi dada aos fenômenos de conservação de momento, ruptura, evaporação e mistura do caso de teste "Spray G" da rede de combustão em motores (ECN, *engine combustion network*). Os processos de ruptura e evaporação foram investigados e simulados, sendo os resultados interpretados de acordo com os modelos utilizados. O comprimento de penetração foi validado com experimentos e uma boa concordância foi atingida. Finalmente, um estudo de sensibilidade da malha foi realizado e seus resultados apresentados e discutidos.

PALAVRAS-CHAVE: CFD, LES, Motor de Combustão Interna, Combustão, Spray, OpenFOAM.

RIBEIRO, M. D. **Engine LES with Fuel-Spray Modeling.** 2015. 118 p. Dissertation (Master in Mechanical Engineering) – Faculdade de Engenharia do Campus de Guaratinguetá, Universidade Estadual Paulista, Guaratinguetá, 2015.

ABSTRACT

The internal combustion engine is the major energy source of automobiles and is of large importance for the energy sector worldwide. As problems related to exaggerated pollutant and greenhouse gases emissions emerged, the development of models to correctly describe the physical phenomena taking place inside the combustion chamber of engines became relevant. Thus, in the first part of this work the open source CFD library OpenFOAM with modules developed at the University of Duisburg-Essen was used to investigate the effect of the crevice volume on the performance of the combustion in port fuel injection spark ignition engines. The LES (large eddy simulation) simulations were validated against high speed flame visualization obtained from the Duisburg optical engine, which showed the presence of a luminous front inside the top land crevice that could be a wrinkled flame. The presented results showed good qualitative agreement with the experimental data, which allowed the conclusion that in the case of the Duisburg engine, the flame indeed penetrates into the crevice volume. Furthermore, a study on fuel sprays was performed, since this is a very promising trend related to modern engines. Special attention was given to the phenomena of momentum exchange, droplet breakup, evaporation and mixture from the test case "Spray G" provided by the Engine Combustion Network (ECN). The processes of droplet breakup and evaporation were investigated and simulated, being the results interpreted according to the models used. The penetration length was validated against experiments and good agreement was obtained. Finally, a mesh sensitivity study was performed and the results presented and discussed.

KEYWORDS: CFD, LES, Internal Combustion Engine, Combustion, Spray, OpenFOAM.

LIST OF FIGURES

LIST OF TABLES

LIST OF FRAMES

LIST OF ABBREVIATIONS AND SYMBOLS

Abbreviations:

ASOI – After start of injection
BDC – Bottom dead center
CAD – Crank angle degree
CDF – Cumulative probability density function
CDS – Central differencing scheme
CFD – Computation Fluid Dynamics
CFL – Courant-Friedrichs-Lewy number
DISI – Direct injection spark ignition
DNS – Direct numerical simulation
ECN – Engine Combustion Network
FDM – Finite difference method
FSD – Flame Surface Density
FVM – Finite volume method
HC – Hydrocarbon
HCCI – Homogeneous charge combustion ignition
ICE – Internal combustion engine
IVG – Institut für Verbrennungs und Gasdynamik
JANAF – Joint-Army-Navy-Air-Force
LES – Large eddy simulation
LPT – Lagrangian particle tracking
OpenFOAM – Open field and manipulation
PISO – Pressure implicit with splitting of operator
PIV – Particle image velocimetry
PLIF – Planar laser induced fluorescence
RANS – Reynolds averaged Navier-Stokes
SG-SIDI – Spray guided spark ignition direct injection
SIMPLE – Semi-implicit method for pressure linked equations
SMD – Sauter mean diameter (d32)
STL – Stereolithograpy
TDC – Top dead center
TVD – Total variation diminishing
UDS – Upwind differencing scheme
WG-SIDI – Wall guided spark ignition direct injection

Latin characters:

a – Discretised transport term
A – Surface area (m^2)
c – Combustion progress variable

c_D – Drag coefficient
c_{dis} – Discharge coefficient
c_p – Specific heat capacity at constant pressure (J/mol.K)
C_s – Smagorinsky constant
d_q – Two-wall quench distance (m)
D,d – Diameter (m)
e – Internal energy (J)
ft – Fuel mass fraction
h – Enthalpy (J)
K – Kinetic energy (J)
Nu – Nusselt number
p – Pressure (Pa)
P_{max} – Maximum in-cylinder pressure (bar)
Pr – Prandtl number
Re – Reynolds number
s – Entropy (J/K)
S – Penetration length (m)
S_{ij} – Rate of strain tensor
t – Time (s)
T_W – Crevice wall temperature (K)
u,v,z – Velocity (m/s)
V – Volume (m^3)
We_l – Liquid Weber number
We_g – Gas phase Weber number
Y_i – Mass fraction of species i
Z – Ohnesorge number

Greek characters:
α – Themal diffusivity (m^2/s)
δ – Kronecker delta
ε – Energy dissipation (m^2/ s^3)
λ_s – Stoichiometric air to fuel ratio
μ – Viscosity (Pa.s)
ν – Kinematic viscosity (m/s^2)
ρ – Density (kg/m^3)
Σ – Summation
ζ – Surface tension (J/m^2)
ς – Heat transfer correction
η – Reynolds stresses (m^2/ s^2)
Φ – Spray cone angle (°)
ω – Angular velocity (rad/s)

CONTENTS

1 INTRODUCTION

The internal combustion engine is an engine that transforms the energy provided by the combustion of the air-fuel mixture inside a combustion chamber into useful mechanical energy. Since its appearance in the second half of the nineteenth century, it has been used for many different applications in the industry and also in the everyday life. From all these applications, it must be pointed out the high potential of such engines for transport purposes with its vast utilization as the motoring machine of automobiles worldwide.

From the very beginning of its development until the current time, the internal combustion engine was modified and improved very often, having the first primitive engines a huge difference in efficiency and maximum power in comparison to the new state of art modern ones. They are distinguished in a bunch of ways, regarding the construction type, number of strokes per cycle, fuel and thermodynamic process.

However, with the good popularity of engines in the transport sector, problems related to exaggerated pollutant and greenhouse gases emissions emerged, compromising people's health and causing severe damages to the environment in a global manner. To avoid these problems, alternatives to internal combustion engines were proposed, from which we can highlight electrical engines and fuel cells. As these alternatives are still not cost effective and unable to cover wide ranges, strict legislations were created for the engine manufacturing sector to guarantee a sustainable development in the near future. One of the main challenges for engineers and researchers around the world is to develop new models that correctly represent the physical phenomena taking place inside engines and thereby design new technologies to achieve these legislations. An approach to investigate the in-cylinder phenomena is the development of research engines, which have normally one single cylinder and a glass liner in order to allow optical access. In these, different experimental techniques can be applied to obtain information about the flow within the entire cycle and chemical reactions during combustion. However, due to the difficulty of setting up those experiments, the costs may become too high and some regions may be impossible to be accessed. To overcome these shortcomings, numerical simulations can be used, giving reliable results with much reduced cost and resolving different physical phenomena within the whole domain geometry, in three dimensions and high resolution. The results of numerical simulations can be then validated against experimental results, where optical access can be achieved.

Research engines have normally much larger crevice volumes than production engines. First, because the distance between the piston crown and the first seal ring must be enlarged to allow optical access through the liner and second, because the clearance between the piston and the glass liner must be increased so that the glass is not damaged due to the piston's movement. Thus, optically accessible engines have a much bigger top land crevice volume, giving researchers a good opportunity to study its effect on the combustion process. Because of the air-fuel mixture trapped inside the crevices, part of it may not be completely burned and therefore the crevice volumes are believed to be the major cause of HC emissions in engines.

Besides the importance of investigating the crevices and their impact in emissions, stratified-charge combustion became also a trend in engine research towards the achievement of optimized specific fuel consumption. Therefore models must be developed to describe the physics of fuel droplets being injected in combustion chambers, so that the phenomena of momentum and heat exchange, evaporation and combustion of fuel sprays can be predicted with accuracy and implemented in engines. These models can give researchers important insights, which perhaps allow a change from the standard port-fuel injection to modern state of art direct-injection engines.

The next subsection will introduce the structure of the present work and after this the aims of the work will be presented.

1.1 Structure of the current work

In chapter 2, a literature review on the development of engine research, exposing both experimental and numerical techniques, will be presented. Furthermore in chapter 3, the relevant numerical methods used within this work are addressed. There, basic concepts of large-eddy simulation and the filtered governing equations will be explained, as well the numerical schemes and details of the numerical solver used in the engine and spray simulations conducted in the current work. In chapter 4, the theory of internal combustion engines and the special difficulty of modeling the crevice volume in engine simulations are discussed, introducing after this the engine test-bench used for data validation and the numerical setup of the simulations, ending with the results for cold-flow and combustion and validation. In chapter 5, the theory of fuel-sprays and spray modeling is also presented, together with its test-case, the numerical setup, results and validation. Finally, in chapter 6 the presented results are discussed.

1.2 Aims of the current work

The aim of the current work is the modeling of a spark ignition optical engine and fuel-sprays using large eddy simulation and open CFD 3D tools. In the first part, a study of the effect of the crevice volume on the performance of the combustion will be presented and the results validated against experimental data obtained from the Duisburg optical engine. The results of the cold flow will be also studied in detail. In the second part, the test-case Spray-G from the engine combustion network (ECN) will be introduced and the results obtained from the simulations performed in this work will be presented and also validated against experimental results.

The specific goals of the current work are:

- Analysis of the flow properties of the Duisburg optical engine in motored conditions;
- Comparison of the flame front propagation during combustion of the LES results vs. experiments;
- Investigation of the flame behavior in the top land crevice volume;
- Study and testing of different spray sub-models (momentum exchange, heat transfer, evaporation) using the Spray G test-case (ECN);
- Validation of the simulated penetration length with experimental results.

2 LITERATURE REVIEW

The legislation on the pollutant and noise emissions of internal combustion engines (ICEs) has severely changed in the last decades, becoming much more restrictive. (GALINDO et al., 2010). Moreover, recent observations show that problems related to the climate change are linked to human activities, motivating more frequent researches with the aim to reduce the emission of greenhouse gases and increase the performance of engines in automobiles. In order to assist such research efforts, computational fluid dynamics (CFD) codes are employed, simulating the flame kernel propagation and in-cylinder phenomena as heat and mass transfer processes in great detail. (KOSMADAKIS; PARIOTIS; RAKOPOULOS, 2013).

The motivation highlighted by Kosmadakis and his collaborators is also present in the current work. The main idea is that CFD simulations are able to support the development of new technologies that meet the legislations and positively impact the society by the reduction in the emission of harmful substances to the human's health and to the environment.

In addition to numerical simulations, more precise and accurate experimental techniques in internal combustion engines such planar laser induced fluorescence (PLIF) and particle image velocimetry (PIV) have been used from different groups and shall work together with simulations to develop new trends in the field. In the work of Peterson et al. (2014), for example, these techniques were used to investigate the causes of rare misfire and partial combustion in spray guided direct injection engines (SG-SIDI), which provide good potential to improve the specific fuel consumption in gasoline engines. The authors showed that such problems were mainly caused by improper flame development due to slow flame propagation and identified the mechanisms of lean mixture, external dilution and convection velocities impeding transport of the flame into the fuel as reasons. (PETERSON; REUSS; SICK, 2014).

Even longer time ago, the Laser Doppler velocimetry technique has also been applied in engines, as shown in the work of Liu et al. (1990). The authors measured the flow in the coolant passages of an engine cylinder using an acrylic model and their results allowed the design of new cylinder heads. However, experimental investigations of the flow field and combustion phenomena are difficult to realize in combustion engines, which require thereby optical access. In optical research engines, the cylinder liner is replaced by a quartz glass. Due to the existence of shortcomings in experimentation techniques, many researchers have turned

their attention to the use of computational methods for the development of models to describe the in-cylinder phenomena in engines.

As pointed out by Westbrook et al. (2005), the numerical simulation of engines before mid-1970s was a little explored subject of research, mostly because of the lack of computer resources. The ability of computers in resolving practical problems as the ones related to in-cylinder flows and combustion can be measured by Moore's law, which states that the number of transistors (or the number of floating operations per seconds - flops) in a dense integrated circuit doubles approximately every two years. At the very beginning, the interest came from American governmental research groups, which firstly identified the difficulties and the problems related to engine in-cylinder events at the Workshop on the Numerical Simulation of Combustion for Application to Spark and Compression Ignition Engines in La Jolla, California, in 1975. After this, great advances were achieved, when some of these interested scientists persuaded the American government and automotive companies like GM, Ford and Chrysler, that only a joint effort of government, universities and industry would be able to address important problems, like laminar pre-mixed and diffusion flames at elevated pressures, flame quenching on engine surfaces, burning of individual fuel droplets, soot kinetics, radiation transport in engine and furnaces, influences of fuel variability, effects of the complex composition of gasoline and diesel fuel, flows through intake and exhaust ports and turbulent coupling between fluid mechanics and chemical kinetics. The idea was reproduced in Europe, where exceptional results were also achieved. (WESTBROOK et al., 2005).

The advances obtained within the joint cooperation described above resulted in the development of the most spread internal combustion engine simulation code, called KIVA. During its beginning, the primary versions of the KIVA code carried simplified reaction sub-models, spray evolution sub-models, simplified wall heat models and the Reynolds Averaged Navier-Stokes (RANS) k-epsilon turbulence model. Despite this limitations, the code was already able to simulate with good prediction capability stratified charge combustion and engine emissions. The code evolved since then, carrying up to date sub-models and providing even better mesh solutions and predictions for different engine technologies. (AMSDEN; AMSDEN, 1993).

In parallel, other achievements were obtained by different researchers towards the direction of improving numerical methods in internal combustion engines. Ahmadi-Befrui, Gosman, Issa and Watkins (1990) applied extensions to the implicit non-iterative PISO solution procedure in order to simulate flows in motored reciprocating engines. Using

orthogonal curvilinear meshes to handle complex geometries and the k-epsilon turbulence model, the authors could increase the speed of the velocity-pressure coupling algorithm by nearly an order of magnitude faster than the SIMPLE procedure.

For a long time the standard simulation framework to describe the turbulent motion of the in-cylinder charge was the Reynolds Averaged Navier-Stokes (RANS) approach, in which the governing equations are averaged and the mean fluctuations of all the interest quantities are neglected. This technique saves computational resources but introduces the disadvantage of modeling the entire range of turbulent scales. Resolving all the turbulent scales exactly as described by the governing equations would be very expensive because capturing the smallest structures requires very high grid resolution. At the moment, this is only feasible for physical phenomena involving smaller Reynolds numbers than that related to engine flows and this is known as Direct Numerical Simulation (DNS).

In order to be a compromise between the accuracy of exactly resolving the large scales of turbulence and the use of reasonable computational resources by modeling the smallest ones, Large-eddy Simulation (LES) was created. With LES, instead of averaging, a filter is applied to the governing equations to distinguish between large and small vortices. The idea is to resolve the turbulent scales exactly as described by the Navier-Stokes equations until a certain length scale. The smaller scales are modeled by considering the dissipation of kinetic energy at sub-grid scales analogous to molecular diffusion and representing its effect with the eddy viscosity approach. In comparison to RANS, LES brings the advantage of resolving the dynamic of the process by not neglecting the mean fluctuations, capturing smaller structures and achieving more accuracy. Moreover, LES is able to capture the cycle-to-cycle variations in internal combustion engines, which cannot be predicted by RANS models.

Moving on to recent work in this field, Enaux et al. (2011) performed multi-cycle large eddy simulations (LES) of a spark ignition engine to study the reasons of cycle-to-cycle variations (CCV) during combustion. The fully compressible and explicit AVBP code was used to cover 25 consecutive cycles and it was shown that variations are related to changes of the tumble residual motion at spark timing for different cycles.

In the work of Nguyen et al. (2014), LES of a spark ignition engine was performed using two different approaches: the open source code OpenFOAM and the efficient in-house code PsiPhi. OpenFOAM is an open coded library written in C++ for solving partial differential equations, widely used for the solution of CFD problems either in the academia as in the industry. The advantage of using OpenFOAM is the open access to the source code maintained by a wide community of researchers with excellent background on fluid dynamics

and its high flexibility for modifications and creation of own libraries and solvers under the GNU General Public License. PsiPhi, on the other hand, is an efficient in-house CFD code, which uses immersed boundaries and Lagrangian particles to describe the moving walls of an equidistant cartesian grid. The code combines high computational accuracy with good parallel scalling and parallelization techniques. The code focuses on LES for handling the turbulent scales and has proven good ability on the solution of several combustion problems. (NGUYEN et al., 2014). The advantages and weaknesses of each approach were compared and discussed. Further on, the results were validated against published experimental data from an optical engine.

Recently, Misdariis, Vermorel and Poinsot (2015) proposed a simple model to predict auto-ignition in order to account for abnormal combustion in internal combustion engines, also using LES. Their methodology uses a single two-reaction reduced scheme and proposes some parameter modifications in the equations that account for the reaction rate in the chamber to consider auto-ignition. The authors investigated the sensibility of the model at different temperature ranges and successfully applied their methodology to laminar configurations and to configurations similar to engines.

As introduced in the previous chapter, the crevice volume in an internal combustion engine is one of the major contributors for the hydrocarbon (HC) emissions and should also be considered to achieve the emission standards. During the compression stroke, the high pressure inside the combustion chamber forces the air-fuel mixture to get into the crevice volumes. As the combustion in these regions may not take place due to flame quenching, the efficiency of the whole combustion process may be compromised. Studies have been conducted by different researchers and some of them will be summarized in the next lines.

In the paper of Alkidas (1999), a review of different studies about the influence of the crevice volume on the combustion and the source of engine-out hydrocarbon under fully warmed conditions was made. He pointed out that when the piston is at top dead center, the combustion chamber crevices account for about 3.5% of the total combustion chamber volume. However, because of the relatively lower temperature of the trapped gases in the crevices, its corresponding mass fraction is much higher.

Following Alkidas (1999), the mass ratio of crevice gas to total combustion chamber gas is about 7% for a part load engine condition. He concluded, after extensive literature review, that in the case of no propagating flame into the crevice the engine-out HC emissions are linearly related to top-land radial clearances. That means that a decrease in crevice volume decreases engine-out HC emissions. Besides, the crevice gas composition depends on the

position of the spark-plug, the variation of HC emissions with radial clearance reaches a maximum value at a certain critical value and an increase of the charge dilution dramatically increases the two-wall quench distance due to the reduced laminar flame speed. He also pointed out that the chamfering of the piston crown is a very effective way to reduce engine-out HC emissions.

Later on, Rakopoulos et al. (2011) implemented a simple crevice model into an in-house CFD code to investigate the effect of crevice flow in internal combustion engines. They observed that the normal approach to overcome the over estimation of the cylinder pressure due to the omission of the crevice volume is the introduction of a calibration factor to increase the heat fluxes through the walls. As this approach affects the properties of the in-cylinder charge, a simple crevice model was proposed. In this model, there is no need to take the exact geometry of the ring-pack configuration by using isentropic compressible flow equations to calculate the mass flow and pressure in different regions of the piston crevice.

Their results were then validated against experimental data from a diesel and a spark-ignition engine. They concluded that the developed crevice model was able to predict with accuracy the mean cylinder pressure, having little effect on the cylinder velocity field and turbulent kinetic energy inside the chamber and with no need of detailed information. (RAKOPOULOS et al., 2011).

The main difficulty of simulating internal combustion engines lies on the handling of moving boundaries together with the description of complex phenomena like turbulence and combustion. For this, detailed studies of each of these phenomena are needed for a complete understanding of the whole problem. OpenFOAM is a suitable tool for the simulation of internal combustion engines and their related processes, what justifies its choice together with LES to model turbulence in this work. Furthermore, another research subject should also be highlighted since the use of direct injection in production cars became an important trend in the last years. This research subject, which is also a relevant part of the current work, is the study of fuel sprays.

Following Baumgarten (2005), a extensive amount of research efforts is nowadays spent on developing state of art CFD models for the characterization of spray and mixture formation for direct injection of gasoline and diesel engines. (BAUMGARTEN, 2005). That being mentioned, it is important to look at the literature and see what was already made in the field and analyze what kind of contribution the current work can provide.

The work of Drake et al. (2005) presents a numerical and experimental study on spray-guided direct-injected spark-ignition (SG-SIDI) engines, which offer better fuel economy and

considerably reduced hydrocarbon and soot emissions compared to present wall-guided (WG-SIDI) engines. (DRAKE; FANSLER; LIPPERT, 2005).

The authors used a commercial CFD code with standard k-epsilon model and Lagrangian particle approach for simulating a four-valve single-cylinder with pentroof head engine, from which experimental data for the flow field, ignition timing and spray development was obtained. It was observed similar results for the spray structure and liquid penetration for both CFD simulations and experiment. Furthermore, it was shown that the ignition timing and the swirl flow affect the combustion quality. The spray sub-models simulated the processes of penetration, vaporization and mixing adequately and it was pointed out that the CFD calculations combined with high-speed imaging experiments provided better scientific understanding for the optimization of such engines.

Vuorinen et al. (2011) performed a study on the effect of the droplet size and atomization on spray formation using LES and OpenFOAM. They claim that the major framework at the time of their work within the community in this field is the Reynolds Averaged Navier-Stokes (RANS) approach together with the Lagrangian Particle Tracking (LPT) method. In fact, their work is one of the first studies where high resolution LES/LPT diesel spray is considered. (VUORINEN et al., 2011).

First of all, extensive literature review about sub-models for modeling Lagrangian particles was made, giving special attention to breakup models. Vuorinen et al. (2011) argue that even for small Weber number (relation between the aero-dynamical forces acting on a fluid particle and its surface tension) flows ($We < 13$), the use of LES is able to show certain weaknesses in the current models. Hence, a new model based on LES/LPT was proposed and tested to consider the particle breakup with a natural resonance time rate. Their results showed that the droplet size effects on the mixing process and that attention should be paid on the breakup model, pointing out the importance of modeling resonance breakup even for low We.

Goryntsev et al. (2010) performed an investigation of the influence of cycle-to-cycle variations on the mixture phenomenon in direct injection spark ignition (DISI) engines. In this work the LES approach was also combined with LPT for the particle tracking in the spray jet, since RANS is not able to predict cycle-to-cycle variations. One of the most recurrent problems in the development of DISI engines are the cyclic variations of the flow, mixing and combustion processes. (GORYNTSEV et al., 2010).

The authors extended the KIVA-3V code with the standard Smagorinsky LES model and validated the code with a fully developed turbulent flow in a square duct. After finding good agreement of their results with DNS and LES data, motored engine simulations were

conducted and the cycle-to-cycle fluctuations of the in-cylinder flow field analyzed. They concluded in the paper that the cyclic fluctuations have a big impact on the fuel spray injection and in the mixture process. It affected parameters as the jet penetration length and the vapor cloud in the vicinity of the spark plug.

Summarizing this literature review, it is clear that much of the research effort for reducing the pollutant and greenhouse gases emissions as well for improving the efficiency of engines is in the field of direct injection engines. Thus, detailed studies still must be performed and improved to create new sub models for characterizing the correct physical phenomena of spray injection and their implementation in engines. As the computer power evolves over the years, CFD simulations became a crucial tool to describe these phenomena in great detail and accuracy. The present work aims then to contribute with the scientific community by studying in detail the phenomena of the flow and combustion inside engines and the detailed sub models associated with fuel spray injection.

3 NUMERICAL METHODS

Computational fluid dynamics (CFD) has been often used to solve complex fluid flows by applying numerical methods to the Navier-Stokes equations. For this purpose the finite volume method (FVM) must be applied to solve the partial differential equations accounting for the physics of the studied flow. The idea is to approximate the partial derivatives by discrete differences, so that the partial differential equations can be solved as algebraic equations. Similar as in finite difference methods (FDM), one must only know the initial and boundary conditions to deal with the problem. In FVM however, a control volume is defined around every single grid point and the conservation laws must be respected if fluxes from any quantity are calculated through the interface between two different volumes. Due to this conservation property, FVM is more stable and hence chosen for solving CFD problems.

Figure 1 – Details of discretised control volume (OpenFOAM user's guide)

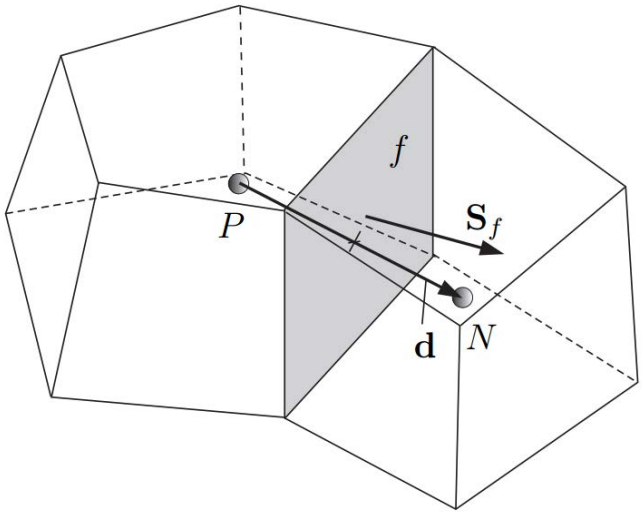

The figure 1 shows in detail how a control volume used by FVM methods looks like. In the figure, P represents the center of an ordinary control volume, where the different quantities regarding the properties of the flow are stored. N represents the center of a neighbor control volume to P, while the gray surface f separating the two volumes represents the interface between the two volumes. The fluxes of momentum, temperature or any other interest quantity are calculated over all that interfaces for each control volume. The flux entering an element should have exactly the same value of the flux leaving the adjacent element, so that the method is conservative.

Now that the CFD approach was introduced, the relevant governing equations to describe the behavior of a fluid flow will be presented in the next subsection.

3.1 LES and the filtered Navier-Stokes equations

In the present work, large eddy simulation (LES) is going to be used for the simulation of complex physical phenomena taking place inside the combustion chamber of an internal combustion engine, as turbulent flow and turbulent combustion. Turbulent flows present a range of tri-dimensional random structures, which can be distinguished by their length scale, characteristic life time and level of order. The larger scales or large eddies are generated by the mean flow and are highly influenced by the geometry. They own most of the energy and thereby last longer, having a big influence on the mixing process. The energy contained in these large eddies are transferred to smaller eddies according to the so called energy cascade.

Figure 2 – Energy cascade, Turbulent Flows lecture (Prof. Andreas Kempf)

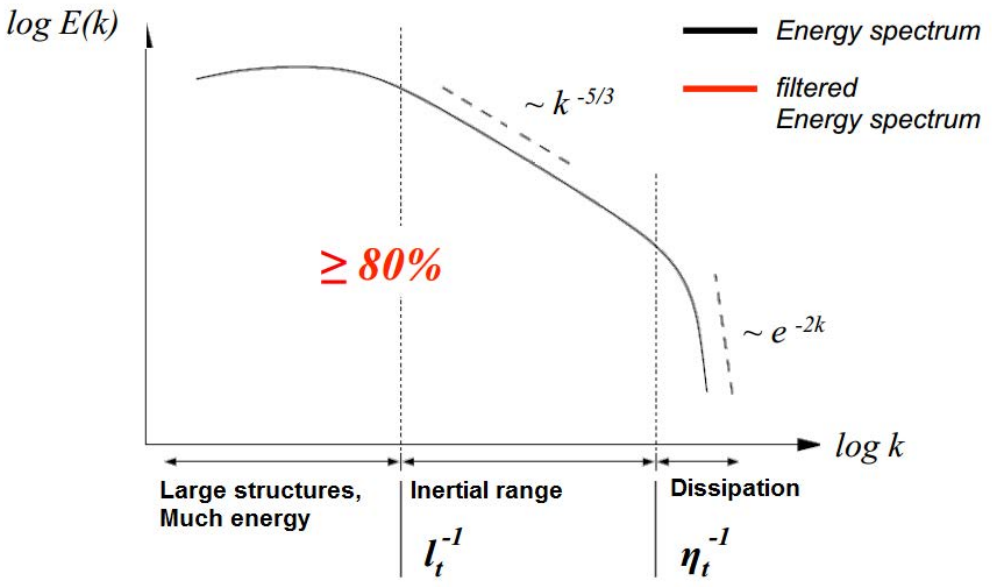

in which, E(k) is the total energy contained in the turbulent eddies, k is the turbulent kinetic energy, l_t is the turbulent length scale and η_t the Kolmogorov length scale. The small turbulent scales generated by the bigger vortices (figure 2), on the other hand, have little energy and dissipate it into heat. That makes them much easier to model, since their life time is also very short and they are isotropic.

Resolving all the turbulent scales exactly as described by the Navier-Stokes equations would be very expensive due to the point of view of computational resources (because to capture the smallest scales require very high grid resolution and thereby extreme fine meshes, which require small time steps). Nowadays, it can be made for physical phenomena involving smaller Reynolds numbers than that related to engine flows and this is known as direct numerical simulation (DNS). Alternatively, one can also use the RANS approach for modeling the turbulence, where the governing equations are averaged and the mean fluctuations neglected. In this case, the computational requirement is much reduced but one has now the disadvantage of applying models to describe the whole turbulent motion.

Although the current RANS models are well established and in many cases able to describe the turbulence accurately, much information is lost by neglecting the mean fluctuations. The idea behind LES is then quite simple. If one applies a filter to the Navier-Stokes equations in such a way that we can distinguish between two different turbulent scales (large and small), the flow properties can be resolved exactly from a range containing the hard to model large scales until a certain smaller length scale. This last length scale would be as big as the filter width and the turbulent kinetic energy contained within this range would reach at least 80% of the total turbulent kinetic energy. This would require higher grid resolution than RANS but still much lower than DNS. The rest or the sub-grid turbulent kinetic energy would be subject of models, which would be much less complicated than regular RANS models since the eddies to be modeled in this case would be much smaller and isotropic. Different LES models have been developed in the literature, from which we can highlight the standard Smagorinsky that will be used in this work.

The filtered governing equations read for the balance of mass in equation (1), the balance of momentum in equation (2) and the balance of total energy in equation (3):

$$\frac{\partial \bar{\rho}}{\partial t} + \frac{\partial (\bar{\rho}\tilde{u}_j)}{\partial x_j} = 0 \tag{1}$$

$$\frac{\partial}{\partial t}(\bar{\rho}\tilde{u}_i) + \frac{\partial}{\partial x_j}(\bar{\rho}\tilde{u}_i\tilde{u}_j) = \frac{\partial}{\partial x_j}\left[\bar{\rho}\bar{\nu}\left(\frac{\partial \tilde{u}_j}{\partial x_i} + \frac{\partial \tilde{u}_i}{\partial x_j}\right) - \frac{2}{3}\bar{\rho}\bar{\nu}\frac{\partial \tilde{u}_k}{\partial x_k}\delta_{ij} - \bar{\rho}\tau_{ij}^{sgs}\right] - \frac{\partial \bar{p}}{\partial x_i} + \bar{\rho}g_i \tag{2}$$

$$\frac{\partial}{\partial t}(\bar{\rho}\tilde{h}) + \frac{\partial}{\partial x_j}(\bar{\rho}\tilde{h}\tilde{u}_j) + \frac{\partial}{\partial t}(\bar{\rho}\tilde{K}) + \frac{\partial}{\partial x_j}(\bar{\rho}\tilde{K}\tilde{u}_j) = \frac{\partial}{\partial x_j}\left(\alpha_{eff}\frac{\partial \tilde{h}}{\partial x_j}\right) + \frac{\partial \bar{p}}{\partial t} \tag{3}$$

in which, ρ is the fluid density, u is the velocity, p is the pressure, ν is the kinematic viscosity, g the gravitational acceleration, h the enthalpy, K the kinetic energy and α_{eff} the effective thermal diffusivity.

In the continuity equation (1), the first and second terms are the density accumulation and mass conservation terms. In the left side of the momentum equation (2), the first and second terms are the momentum accumulation and convection terms. In the right side, the first term represents the stress tensor with the resolved and unresolved (sub-grid) parts, followed by the pressure term and the term accounting for the gravity force. In the energy equation (3), the left side shows the accumulation and convective enthalpy and kinetic energy terms. Finally, in the right side are the thermal diffusion and the pressure terms. The tilde over the quantities implies that these equations are operating over the filtered quantities of the fluid of interest and the bar sign means averaging.

The sub-grid stresses η_{ij}^{sgs} show up in the momentum equation and represent the unresolved part of the Reynolds stresses. In LES, the dissipation of kinetic energy at sub-grid scales is considered to be analogous to molecular diffusion and thus a turbulent viscosity is introduced. The influence of the sub-grid scales on the fluid is therefore represented by an increase of viscosity.

Joseph Smagorinsky, an American meteorologist, developed one of the first successful LES approaches, which was named after his name. The classical Smagorinsky model of 1963 was a result of his studies about large-scale atmospheric motions and is based on the idea that the unresolved scales increase the stresses, being compared to the effect of viscosity.

An effective viscosity is then defined to model these sub-grid stresses, adding a turbulent contribution ν_t to the molecular viscosity ν ($\nu_{eff.} = \nu + \nu_t$). Equation (4) shows how the sub-grid stresses η_{ij}^{sgs} are modeled:

$$\tau_{ij}^{sgs} - \frac{1}{3}\tau_{kk}^{sgs}\delta_{ij} = -2(C_s\Delta)^2|\bar{S}|S_{ij} \tag{4}$$

In the last equation, the turbulent or eddy viscosity is represented by the term $(C_s\Delta)^2|\bar{S}|$ and S_{ij} is the rate-of-strain tensor, calculated as shown in equation (5).

$$S_{ij} = \frac{1}{2}\left(\frac{\partial \bar{u}_j}{\partial x_i} + \frac{\partial \bar{u}_i}{\partial x_j}\right), \quad |\bar{S}| = \sqrt{2S_{ij}S_{ij}} \tag{5}$$

For completeness, Δ is the filter width and C_s is the Smagorinsky constant. They are used to derive a length scale ($l_s = C_s\Delta$) for the LES model, equivalent to a zero-equation model in RANS. Suitable Smagorinsky constants vary in a range from 0.05 to 0.173 (Turbulent Flows lecture by Prof. Andreas Kempf) and in this work the value 0.062 is going to be used.

Information regarding the numerical schemes and the code used will be presented in the next subsections.

3.2 Numerical schemes

As CFD numerical codes are based on the finite volume method, spatial and temporal discretisation of the governing equations is required.

For those who are interested in obtaining information about numerical schemes for CFD, Patankar (1980) and Versteeg & Malalasekera (1995) are highly recommended. Here only the most important schemes regarding the discretisation of the convective terms of the governing equations will be summarized.

The Central Differencing Scheme (CDS) is second-order accurate and based on linear interpolation between the value stored in an arbitrary cell and each one of the adjacent elements. The scheme is said to be second-order because it takes the values stored in both the cell and its neighbor into account for calculating the value at the interface between them. For instance, if one wants to calculate the value of a certain quantity Φ at the interface w separating the points P and W of a computational grid, the subsequent result Φ_w will be calculated as shown in equation (6):

$$\Phi_w = \frac{1}{2}\left(\Phi_W + \Phi_P\right) \tag{6}$$

The weakness of this scheme is that it is not bounded, i.e. it doesn't account for the direction of the flow. Therefore, stability problems may arise if low order time integration schemes are used or if regions with high gradients are present, generating wiggles in the solution.

To overcome the problem of unboundedness, the Upwind Differencing Scheme (UDS) was proposed. The UDS scheme assumes for a certain interface the value of the variable in the upwind direction of the flow. This means that the scheme considers the direction of the flow and therefore is bounded but has the weakness of being only first-order accurate in

contrast with the CDS scheme. So if again the two grid points P and W are considered, the value at the interface w will be obtained as in equation (7):

$\Phi_w = \Phi_W$, if the fluid is flowing from W to P (7)

$\Phi_w = \Phi_P$, if the fluid is flowing from P to W

The advantage of using UDS is the gain in stability in comparison to CDS. However, the scheme is very diffusive, grid dependent and thus less accurate than a second-order scheme. So pursuing a commitment between the accuracy of the CDS scheme and the stability of the upwind scheme, the so called higher-order Total Variation Diminishing (TVD) schemes were created. The idea of the TVD scheme is to work as a hybrid between CDS and UDS, according to the flow behavior by the use of a limiter function.

The name TVD comes from the fact that in such schemes the total variation of a scalar field must never increase, as described in equation (8).

$$\frac{\partial}{\partial t} TV = \frac{\partial}{\partial t} \int_{V_1} \left| \frac{\partial \phi}{\partial \xi} \right| d\xi \leq 0 \quad (8)$$

The general form of a TVD as well its gradient ratio needed as input for the B limiter function is shown in equation (9).

$$\Phi_e = \Phi_C + \frac{B}{2} (\Phi_C - \Phi_U) \quad (9\text{-A})$$

$$r = \frac{\phi_D - \phi_C}{\phi_C - \phi_U} \quad (9\text{-B})$$

in which Φ are desired properties, B the limiter function and r is the gradient ratio.

Several limiter functions were proposed in the literature and implemented like different TVD schemes, from which Van Leer, Quick, Super-bee and Charm can be mentioned. Although such schemes have a good compromise between accuracy and stability, they are still dissipative and thus may not be advisable for LES.

Too much dissipation would have a negative effect on the simulation of internal combustion engines since the combustion depends on high turbulence inside the combustion chamber to take place effectively. The presence of small structures in the flame front is necessary so that the combustion happens in the right pace and the mixture can be burned in a

reasonable rate. However, very high velocities are expected in engines and the use of CDS scheme in regions where very high gradients are present would be very unstable.

So in order that a compromise between accuracy and stability can be met without using a still too much dissipative TVD scheme for LES, Nguyen et al. (2014) developed a hybrid scheme between CDS and TVD based on the local Mach-number for the convective term of the momentum equation. This differencing scheme was implemented into the current code, so that the engine simulations become more stable without compromising the accuracy of the solution with a full TVD scheme. The idea is to calculate the Mach-number for every single element of the computational domain and locally apply the TVD scheme only in the regions where the Mach-number is higher than 0.5. This strategy (Nguyen et al.) has been working very well for the engine simulations and to our knowledge the present idea was never proposed before.

3.3 Numerical code

The OpenFOAM code version 2.3.x will be used for the LES of engines and fuel-sprays in the current work. OpenFOAM stands for Field Operation and Manipulation, which is an open coded C++ library applicable for the solution of partial differential equations. Thus, it has been widely used for the solution of CFD problems by a big community of researchers and engineers around the world.

The code itself is maintained by the OpenFOAM Foundation, which provides a list of CFD solvers for different applications at each new version. Among its capabilities, one can name the solutions of incompressible and compressible flows, multiphase flows, combustion, buoyancy-driven flows, heat transfer, Lagrangian particle tracking and so on. Besides, meshing tools are also provided for the creation of structured and unstructured hexahedral grids and information about the code and further tools are well documented in the user's and programmer's guide distributed with it.

Not enough, one can also create its own solvers or modify the high level code to reach specific purposes. The code is free and open, since it is distributed under the terms of the GNU Generical Public License published by the Free Software Foundation. This enables the user to develop new models for several physical phenomena in the area of fluid dynamics and combustion. If problems are faced, support can be obtained by the vast OpenFOAM community, composed of people with very good CFD backgrounds.

4 ENGINE MODELING

In this chapter, the model developed in this work for the LES of internal combustion engines will be presented. First, the theory of the four stroke reciprocal engine will be introduced, as well the special difficulty of considering the crevice volume. Then, the numerical solver is going to be explained in detail, highlighting the moving mesh capabilities and the combustion model. After this, the engine test-bench, which is going to be simulated and used for the code validation will be introduced. Finally, after description of the simulation case setup, the results for the cold flow and also for the combustion case will be presented.

4.1 Four stroke reciprocal engine

The object of study of the present work is the four stroke reciprocating engine, which is widely used in the automotive industry. In these engines, the vertical alternative movement of the piston inside the engine cylinder is converted into a rotational movement to the crankshaft by the crankshaft and connecting rod system.

Figure 3 - BMW Z4 Roadster Engine (Copyright BMW)

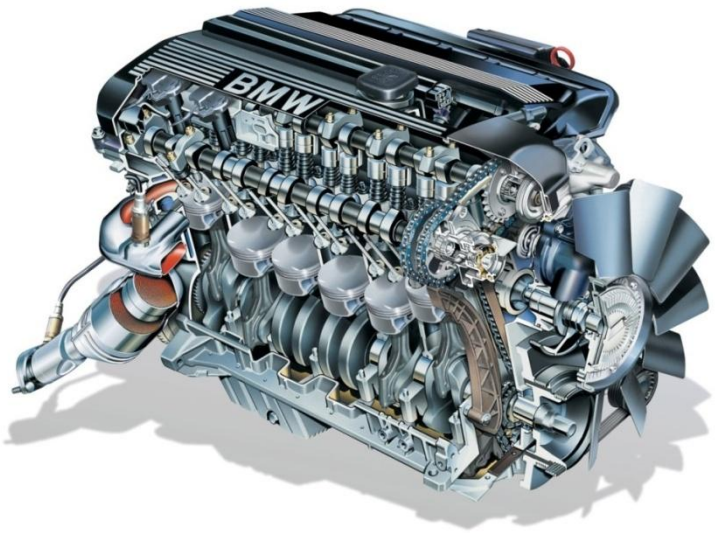

It is called a four stroke engine (figure 3) because of its operation characteristics, where one complete cycle is divided in four stages or strokes: admission, compression, expansion and exhaust. The complete cycle comprehends two rotations and the time definition normally used in such applications is measured in crank angle degrees (CAD), where one CAD

represents one degree rotation of the crankshaft. The time in crank angle degree is linked to the physical time in seconds by the equation (10):

$$CAD = 360\left(\frac{\omega}{2\pi}\right)t\ [degree] \tag{10}$$

in which ω is the crankshaft angular velocity in rad/s and t the time in seconds. The air intake and exhaust flow is controlled by poppet valves located at the top of the cylinder head, which by the action of cam lobes mechanically connected to the crankshaft are opened and closed according to the position of the piston within the cycle. The four stroke cycle will be explained now in detail.

Admission: During admission, the intake valves remain opened and the exhaust valves closed so that the cylinder is filled with a fresh air charge, which may be mixed with fuel in the case of standard port-fuel gasoline engines. It starts with the piston at the top dead center, i.e. in the highest position. The piston then rapidly moves downwards, creating a negative pressure inside the cylinder that pushes that air into its interior.

Compression: When the piston reaches the minimum position or bottom dead center, the compression stroke is started. The intake valves close and the charge is compressed until the piston is found again at the top dead center, completing one entire rotation. In diesel or direct-injection gasoline engines the fuel is added and mixed to the charge inside the combustion chamber during the intake or compression stroke, whilst in port-fuel gasoline engines the mixture process takes place before the admission in the cylinder. Still during the compression stroke, a few crank angle degrees before the piston reaches the top, the mixture is ignited using the energy released by a spark in sparked ignition engines or auto ignited due to the high pressure and temperature in the combustion chamber in the case of diesel engines.

Expansion: The energy produced by the combustion of the air-fuel mixture is then transferred to the piston, which rapidly moves downwards again expanding the burnt mixture inside the cylinder until reaching the bottom dead center. This is the only stroke where work is effectively done over the piston.

Exhaust: To complete the cycle, the exhaust valves open and the burnt mixture is then expelled as the piston moves in the upward direction. When the top dead center is reached, the engine completes its second rotation and the cycle starts again from the beginning.

4.2 Special difficulty: The crevice volume

A special difficulty in the simulation of internal combustion engines is the modeling of the combustion chamber crevices. These crevices are small volumes inside the chamber delimited by narrow surfaces, where due to the relative low temperatures compared to the rest of the domain the combustion may not take place. The figure 4 summarizes the different kinds of crevices in an engine.

Figure 4 – Combustion-chamber crevices (ALKIDAS, 1999)

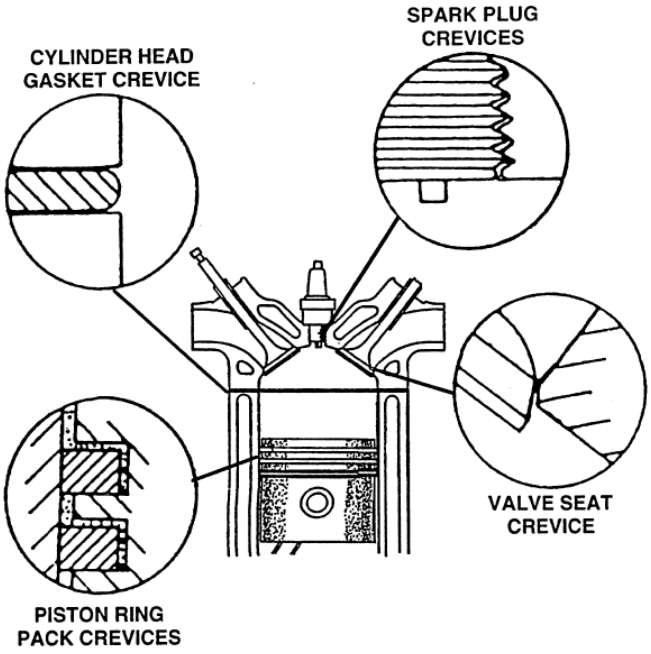

Alkidas (1999) states that the crevices are believed to be the main contributor of the hydrocarbon (HC) emissions under fully warmed conditions in engines. They are represented by the piston ring pack crevices, which are the spaces between different seal rings and the cylinder and piston walls; the cylinder head gasket crevice; the spark plug crevices, which are the spaces between the spark plug body and its seat; and the valve seat crevices, defined as the spaces between the valve top surfaces and the valve seat.

The reason of this high contribution in HC emissions can be explained by the flame quenching, which occurs at the walls of the combustion chamber due to their relative low temperatures. “The cool walls of the chamber act as a sink for heat and the active radical species generated within the flame” (HEYWOOD, 1988).

The quenching of a flame can occur in several distinct configurations and in the case of the crevices it occurs in their narrow entrances. This phenomenon can be studied with a very

simple configuration named two-plate quench process, where the minimum distance between two parallel plates for which the flame propagates through is determined. This minimum spacing is called two-wall quench distance.

In the literature it can be found different empirical equations for the two-wall quench distance, as for example the one developed by Ishizawa (1996), in equation (11):

$$d_q = 14.8\,(P_{max})^{-0.9}(T_W)^{-0.5} \tag{11}$$

in which, d_q is the two-wall quench distance, P_{max} is the in-cylinder maximum pressure and T_w is the wall temperature.

The HC emission phenomenon can be described as follows. As the piston goes up and the in-cylinder pressure increases, five to ten percent of the cylinder charge moves towards the crevice volumes. When the mixture ignites, the flame starts to propagate towards the combustion chamber walls until it reaches the entrance of each one of these crevice regions. At this time and for each crevice, the flame may enter the narrow region and fully burn its content. Another possibility would be entering that region but only partially burn the mixture inside it due to the low wall temperatures. However, if the two-wall quench distance is too small for enabling the flame to propagate, the flame will quench at the entrance of the crevice volume. After the flame arriving and quenching, the burnt mixture will flow into the crevices. As their volumes are very small, the density in these regions increase rapidly and during the expansion stroke the pressure inside them become high enough to expulse their contents to the combustion chamber again. “Depending on spark plug location in relation to the position of the top ring gap, well above 50 percent of this gas can be unburned fuel-air mixture. Its potential contribution to unburned HC emissions is obvious.”(HEYWOOD, 1988).

Very clear evidences of the crevices as main contributors to unburned HC emission come from experimental setups. Different construction techniques and modifications to original engine geometries were made by different groups. For instance, Wentworth (1971) reported reductions of between 47 and 74 percent in HC levels for different operation conditions after almost completely removing the crevice volumes by moving the position of the piston rings so close to the piston head surface as possible. Further literature review on the subject was presented in chapter 2.

Figure 5 – HC emissions against cylinder clearance (HEYWOOD, 1988)

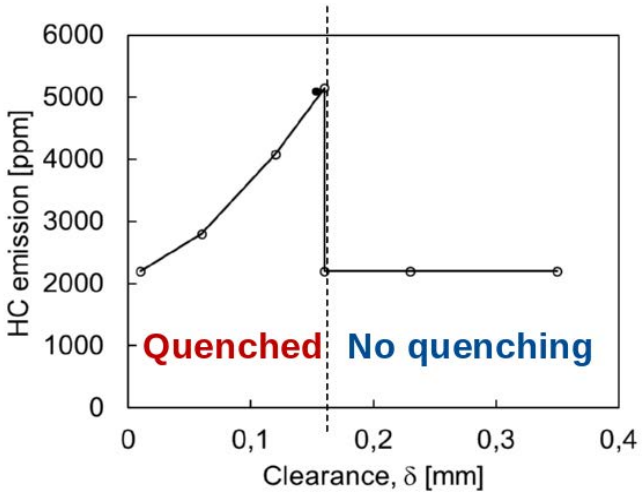

Figure 5 was adapted from Heywood (1988) and illustrates the flame quenching according to the piston top-land clearance. It was demonstrated by different experimental groups that HC emissions increase linearly with increasing clearance as the crevice volume becomes bigger. However, when the clearance becomes as big as the calculated two-wall quench distance, the flame is able to penetrate into the crevice volume and consume much of the HC inside it.

This subsection introduced the importance of studying the crevice volume. In the case of optical engines, the need of a big optical access via glass liner imposes that the first seal ring must be in a much lower position then in the case of production engines. In production engines the distance between the piston crown and the seal ring as well as the top-land clearance is much smaller than in optical engines. Thus, optically accessible engines have a much bigger total crevice volume, giving researchers a good opportunity to study its effect on the combustion process.

4.3 Numerical solver

The solver used for the engine simulation is a modified version of standard solvers for transient trans-sonic/supersonic in laminar and turbulent compressible flows and for turbulent combustion based on the evolution of a combustion progress variable.

For the solution of the governing equations, the solver uses the so called PIMPLE algorithm for the pressure-velocity coupling. The PIMPLE algorithm is a hybrid between the

SIMPLE algorithm developed by Patankar and Spalding (1972) and the PISO algorithm developed by Issa (1985).

The acronym SIMPLE stands for Semi-Implicit Method for Pressure Linked Equations. In this method, the velocities at the cell faces are stored in different grids than scalar variables like pressure and mass fraction with a so called staggered grid. A staggered grid avoids the problem of an oscillating pressure field returning zero gradient values as output. This would imply a zero pressure source in the momentum equation although oscillations are present on the field, what is off course no physical behavior.

In the method, the governing equations are discretised and their solution is provided by iteratively correcting a guessed pressure field from the divergence of its resultant velocity field. The guessed pressure field p* is denoted with a star superscript, as well the velocity field components u*, v* and w* calculated from it. This means that the correct pressure field was still not employed and the resulting velocity field doesn't satisfy the continuity equation. Thus, more iterations are needed to achieve convergence.

The discretised momentum equation for each velocity component is shown in equations (12):

$$a_e u_e^* = \sum a_{nb} u_{nb}^* + b + (p_P^* - p_E^*) A_e \quad \text{(12-A)}$$

$$a_n v_n^* = \sum a_{nb} v_{nb}^* + b + (p_P^* - p_N^*) A_n \quad \text{(12-B)}$$

$$a_t w_t^* = \sum a_{nb} w_{nb}^* + b + (p_P^* - p_T^*) A_t \quad \text{(12-C)}$$

in which coefficients "a_e", "a_n" and "a_t" represent the discretised convective and diffusive transport terms of the momentum equation at the cell faces for the x, y and z components. The subscript P means that the value should be taken from the cell center, the capital A is the area of the cell face and b represents the source term.

The goal now is to derive a pressure correction p' for the pressure field in such a way that the resulting starred velocity field iteration by iteration gets closer of satisfying the continuity equation. The corrected pressure p will be achieved by adding p' to the starred p field (p = p* + p'). This operation will have an effect on the value of each velocity component, which can be represented by adding the velocity correction u', v' and w' to the starred velocities u*, v* and w*.

The authors of the SIMPLE algorithm then decide to drop the terms $\sum a_{nb} u_{nb}^*$ of the discretised momentum equations, so that corrections of the velocity fields and consequently

of the pressure field can be derived. These terms are the neighbor influence in the momentum equation for each cell element. If they were retained, they would result in an unsolvable pressure correction equation, since the neighbors of a cell would bring also the effect of their neighbors and so on. The authors argue that the omission of these terms does not avoid the SIMPLE algorithm of obtaining a converged solution for the pressure and velocity fields, which does not contain any error.

Hence, the resulting velocity correction equations are (13):

$$a_e u_e^{'} = (p_P^{'} - p_E^{'}) A_e / a_e \quad (13\text{-A})$$

$$a_n v_n^{'} = (p_P^{'} - p_N^{'}) A_n / a_n \quad (13\text{-B})$$

$$a_t w_t^{'} = (p_P^{'} - p_T^{'}) A_t / a_t \quad (13\text{-C})$$

In order to satisfy the continuity equation, the pressure correction equation (14) must be solved:

$$a_p p_p^{'} = a_E p_E^{'} + a_W p_W^{'} + a_N p_N^{'} + a_S p_S^{'} + a_T p_T^{'} + a_B p_B^{'} + b \quad (14)$$

in which the term $a_E = \rho_e d_e A_e$, $a_W = \rho_w d_w A_w$, $a_N = \rho_n d_n A_n$ and so on are the mass fluxes through each cell face. The term b represents a "mass source" in the continuity equation (15).

$$b = \frac{(\rho_P^0 - \rho_P)V}{\Delta t} + [(\rho u^*)_w - (\rho u^*)_e] A_x + \\ + [(\rho v^*)_s - (\rho v^*)_n] A_y + [(\rho w^*)_b - (\rho w^*)_t] A_z \quad (15)$$

in which V is the volume of the control volume, ρ_P the density at the cell center and Δt the time step. After deriving the equations above, the SIMPLE algorithm can be applied, which step-by-step is described as follows:

1 – Guess a pressure field p*;

2 – Solve the discretised momentum equations (12) for u*, v* and w* from the pressure field p*;

3 – Solve the pressure correction equation p' (14);

4 – Correct pressure field by adding p' to p*. Under-relaxation factor may be necessary;

5 – Correct velocity fields by using the velocity-correction equations (13);

6 – Solve the transport equation for all other variables;

7 – Check if there is convergence. If not, treat the new calculated p as p* and start again from 2. If yes, stop solution. A good convergence criterion is checking if the "b" term (equation 15) of the pressure correction is null. This term would imply a "mass source" in the continuity equation.

The idea behind the PISO algorithm, Pressure Implicit with Splitting of Operator, is to split the pressure corrector in two or more steps, so that the first one will create a conservative field and the second or following will stabilize the pressure field. This is possible since the linear pressure-velocity correction coupling is much stronger than the non-linear coupling present in the discretised momentum equations for u*, v* and w*. It allows a big number of pressure corrections with no significant change on the value of u*, v* and w* at small time steps.

Step 4 of the SIMPLE algorithm is evaluated in two or more steps with the PISO algorithm and an under relaxation factor for the pressure is hence not necessary.

The PIMPLE algorithm is basically the PISO algorithm of Issa (1985) with the addition of eventual outer correction loops of the variables over each time step using the last iteration final value as initial guess for the next iteration, like in the SIMPLE method. For this reason, under relaxation of the variables between consequent outer iterations may be applied.

4.3.1 Thermo-physical properties

Regarding now the handling of the thermo-physical properties of the flow, the code uses the coefficients from the JANAF thermodynamic tables for the different species specified in the *thermophysicalProperties* dictionary. The species considered within this study are three: air (oxidant), iso-octane (fuel) and burnt gases.

The energy equation is resolved for the filtered internal energy $\tilde{e}$ for the cold flow and the filtered total enthalpy $\tilde{h}$ during the combustion. Correlations using the JANAF coefficients are used for obtaining the values of the specific heat capacity c_p and the entropy s, and hence the temperature can be derived.

The mass fraction for each species is calculated based on the value of the filtered combustion progress variable $\tilde{c}$, which is going to be explained in the next subsection, the fuel mass fraction f_t and the stoichiometric air to fuel ratio λ_{st}. The mass fraction for the fuel, air and burnt gases are given by equations (16), respectively.

$$Y_{fuel} = (1-\tilde{c})f_t + \tilde{c}\left(f_t - \frac{1-f_t}{\lambda_{st}}\right) \quad (16\text{-A})$$

$$Y_{air} = 1 - f_t - \left(f_t - Y_{fuel}\right)\lambda_{st} \quad (16\text{-B})$$

$$Y_{burnt} = 1 - Y_{fuel} - Y_{air} \quad (16\text{-C})$$

Finally, the viscosity of the mixture is given by the Sutherland law, presented in equation (17).

$$\mu = \frac{A_s\sqrt{T}}{1+T_s/T} \quad (17)$$

in which A_s is the Sutherland coefficient and T_s the Sutherland temperature.

4.3.2 Moving mesh capabilities

One of the main challenges of this work is the handling of moving meshes together with several complex phenomena taking place in a very short time. This subject is relevant in engines, since the movement of piston and valves must be treated. As discussed in the chapter 3, the finite volume method is applied in a control volume defined for each cell of the computational domain, where the conservation laws must be respected. However, if the boundaries of a control volume start to move, the conservation law equations must consider its displacement.

The moving mesh approach used in this work is the one developed by Jasak and Tukovic (2004) and is going to be briefly explained now. First, one has to modify the discretised conservation equation for an arbitrary property Φ over a control volume, so that it takes the boundary movement into account. This is done in equation (18):

$$\frac{(\rho_P\phi_P V_P)^n - (\rho_P\phi_P V_P)^o}{\Delta t} + \sum_f \rho_f\left(s_f \cdot u_f - s_f \cdot u_s\right)\phi_f = -\sum_f s_f \cdot \rho q_\phi + S_\phi V_P \quad (18)$$

The subscript P represents the cell center values and f the face values, while “n” and “o” in the accumulation term are labels for “new” and “old”, as the solution marches in time. The term $s_f \cdot u_f$ is the fluid flux F and $s_f \cdot u_s$ is the mesh flux F_s.

The only differences of equation (18) to the discretised conservation equation for a static control volume are the rate of change of the cell volume represented by its first term and the mesh motion flux F_s. This is clear, since as the mesh element is deformed its size may

change. Moreover, as the boundary of the control volume moves, its relative movement to the fluid must be taken into account.

The equation (19) shows the relation between the rate of change of the cell volume and mesh motion flux already in the discretised form.

$$\frac{V_P^n - V_P^o}{\Delta t} - \sum_f F_s = 0 \tag{19}$$

The equation above is known as the space conservation law. The relation shows that the mesh flux F_s is calculated from the swept volume by the surface f over a time-step, making the calculations in the control volume consistent with its movement.

With this approach, the cell points in the piston and valves surfaces can be linearly shifted within the cycle, without neglecting the effect of their movement to the charge inside the cylinder. This practice, however, should be performed with care, since it impairs in deformation to the mesh elements and techniques like re-meshing and mapping should be considered.

4.3.3 Combustion modeling

This subsection aims at the presentation of the combustion model implemented on the code used in the current work. A Flame Surface Density (FSD) model was used, which is based on the transport of a progress variable of combustion and an algebraic equation proposed by Weller (1998) for the flame wrinkling.

The progress variable of combustion c represents the evolution of the combustion process. If c is equal to zero in a certain control volume, it means that the mixture inside its interior is fully unburned and if c, on the other hand, is equal to one, the mixture contained in the cell is fully burned. Any value between 0 and 1 represents that the mixture is only partially burned.

For the Favre-filtered variable $\tilde{c}$, the following transport equation is written in (20).

$$\frac{\partial}{\partial t}(\bar{\rho}\,\tilde{c}) + \frac{\partial}{\partial x_j}(\bar{\rho}\tilde{u}_j\,\tilde{c}) + \frac{\partial}{\partial x_j}\left[\bar{\rho}\left(\widetilde{u_j c} - \tilde{u}_j\,\tilde{c}\right)\right] = \frac{\partial}{\partial x_j}\overline{\left(\rho D \frac{\partial c}{\partial x_j}\right)} + \bar{\dot{\omega}} \tag{20}$$

First and second terms in equation (20) are the accumulation and convective term of the filtered variable $\tilde{c}$, respectively. The third term represents the sub-grid scalar fluxes and the

terms in the right side are the diffusion and the reaction source term. The last two terms in the right side are modeled by the generalized surface density function (FSD), where the laminar flame velocity S_L and an algebraic equation are used for the description of the flame front evolution. Equation (21) shows how the terms are closed.

$$\frac{\partial}{\partial x_j}\overline{\left(\rho D \frac{\partial c}{\partial x_j}\right)} + \bar{\dot{\omega}} \approx S_L \rho_u \Sigma_{\text{gen}} \tag{21}$$

The flame wrinkling is described by the generalized flame surface density Σ_{gen} proposed by Weller in equation (22).

$$\Sigma_{\text{gen}} = 1 + 2\tilde{c}\left(1 + 0.62\sqrt{\frac{u'_\Delta}{S_L}}\text{Re}_\eta\right)\left|\frac{\partial \bar{c}}{\partial x_j}\right| \tag{22}$$

in which $u'_\Delta = \left(2/3\, k_{sgs}\right)^{0.5}$ is the sub-grid velocity fluctuation and $\text{Re}_\eta = u'_\Delta/\left(\tau_\eta \varepsilon_{sgs}\right)$ the Kolmogorov Reynolds number. In those equations, k_{sgs} is the sub-grid specific kinetic energy and ε_{sgs} is the sub-grid specific energy dissipation. The Kolmogorov time scale η_η is calculated as $\tau_\eta = \left(\mu_u/\left(\rho_u \varepsilon_{sgs}\right)\right)^{0.5}$, where μ_u and ρ_u are the viscosity and density of the unburned mixture, respectively. The symbol η is used to denote Kolmogorov quantities.

Regarding the modeling of the sub-grid scalar fluxes in equation (20), the gradient assumption will be employed. To represent the physical phenomenon of counter flux of the flame front, the counter gradient transport (CGT) proposed by Richard (2007) is used. Equation (23) shows how the term is closed.

$$\left[\bar{\rho}\left(\widetilde{u_j c} - \tilde{u}_j \tilde{c}\right)\right] = -\alpha_t \frac{\partial \tilde{c}}{\partial x_k} - S_L \rho_u (\bar{c} - \tilde{c}) n_j \tag{23}$$

In last equation, $\bar{c}$ is the Reynolds-filtered progress variable, while α_t is the turbulent thermal diffusivity and n_j the normal vector pointing towards the direction of the flame front propagation.

For the calculation of the laminar flame speed, the correlation proposed by Gülder (1984) will be employed, as shown in equation (24). As the fuel is iso-octane, the parameters used in this work are the following: W = 0.4658, η = -0.326, ε = 4.48, α = 1.56, γ = -0.22, and p_{ref} = 1.0131 bar, T_{ref} = 300 K and Φ, the equivalence ratio, is equal to one.

$$S_L = W\phi^{\eta}.exp(-\xi.(\phi - 1.075)^2)\left(T_u/T_{ref}\right)^{\alpha}\left(p/p_{ref}\right)^{\gamma} \quad (24)$$

in which the temperature of the unburned mixture is calculated by solving an additional energy equation (25) for the unburned absolute enthalpy $\tilde{h}_u$, during the combustion process.

$$\frac{\partial}{\partial t}\left(\bar{\rho}\tilde{h}_u\right) + \frac{\partial}{\partial x_j}\left(\bar{\rho}\tilde{h}_u\tilde{u}_j\right) + \left[\frac{\partial}{\partial t}\left(\bar{\rho}\widetilde{K}\right) + \frac{\partial}{\partial x_j}\left(\bar{\rho}\widetilde{K}\tilde{u}_j\right)\right]\left(\frac{\bar{\rho}}{\bar{\rho}_u}\right) = \frac{\partial}{\partial x_j}\left(\alpha_{eff}\frac{\partial\tilde{h}_u}{\partial x_j}\right) + \frac{\partial\bar{p}}{\partial t}\left(\frac{\bar{\rho}}{\bar{\rho}_u}\right) \quad (25)$$

Finally, it must be pointed that this work has no physical model for the ignition. In this case, the ignition is triggered by simply increasing the reaction source term to a sufficiently high value in the vicinity of the spark plug. In subsection 4.5, this value will be presented. Besides, the size of the flame kernel and its position must be also given, what is obtained from visualizations from the experiment.

Within this work, two scenarios were studied. In the first, it was considered flame propagation inside the crevice by setting $\bar{\dot{\omega}} = S_L\rho_u\Sigma_{\text{gen}}$. In the second, the flame is quenched at the crevice entrance by setting $\bar{\dot{\omega}} = 0$, considering only convective and diffusive transport inside the crevice volume.

4.4 Duisburg Engine

At the Institute of Combustion and Gas Dynamics (IVG, acronym from the German Institut für Verbrennungs und Gasdynamik) is located the Duisburg optical engine. The research gasoline single cylinder engine is spark ignited and has an optical access via glass liner, as shown in figure 6.

Figure 6 – Duisburg optical engine at IVG (left) and detail of the optical access (right)

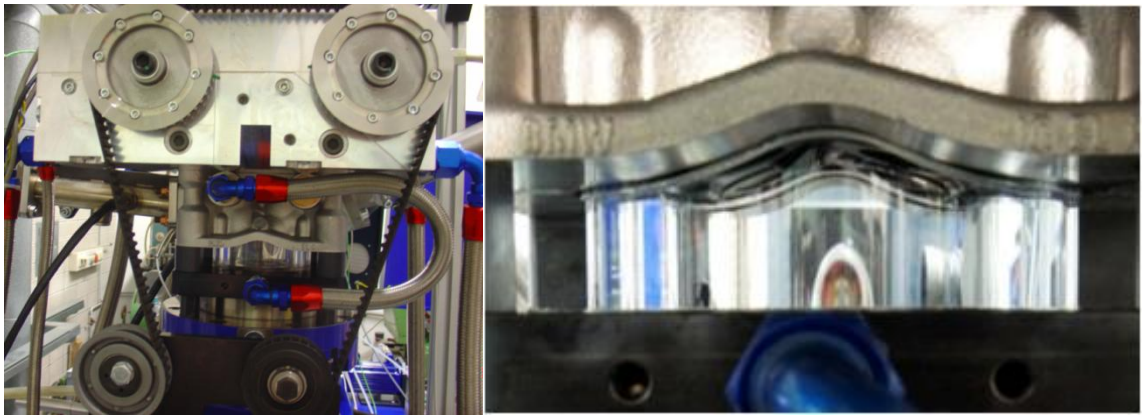

The engine has a pent-roof cylinder head with four valves and flat piston crown. The liner and a window located at the piston head surface are made out of quartz, so that the engine can be optically accessed by laser sheets and from where chemiluminescence or even PIV measurements can be obtained. The table 1 shows some characteristics of the Duisburg engine and table 2 summarizes information about the operation point used for the study in the current work.

Table 1 – Technical information of the Duisburg engine

Duisburg optical engine	
Number of cylinders	1
Bore	84 mm
Stroke	90 mm
Displacement	499 cm^3
Number of valves	4 (pent-roof cylinder head)
Compression ratio	10:1

Table 2 – Operation point investigated in the engine simulations

Operation point	
Engine speed	1500 rpm
Intake pressure	700 mbar
Ignition timing	45 CAD before TDC
Fuel	Iso-octane
Air/fuel ratio	1

The engine is operated by Prof. Kaiser's group, which can provide very reliable data from different operation points of the engine. These data are needed for the numerical setup of the simulations, as for example the pressure at the inlet and outlet boundaries for every single crank angle degree. They also performed chemiluminescence measurements to visualize the flame front propagation with a high speed camera and their results will be used for validation of the CFD code. The relative in-cylinder pressure is taken by a piezo-capacitive sensor and the intake/exhaust absolute pressure by piezo-resistive transducers.

The figure 7 (a) and (b) shows some detailed information on the crevice volume of the Duisburg Engine. In order to have an optical access, the first piston seal is located in a very low position compared to production engines. As in normal manufactured engines the height between the piston ring and the piston crown is no more than 10 mm, in the case of the Duisburg engine it is 31.5 mm. Moreover, the top-land crevice gap (the distance between the

piston and the cylinder surface) is also bigger in optical engines, to avoid that the piston hits against the quartz liner, damaging it.

Figure 7 – Detail of the crevice volume of the Duisburg engine

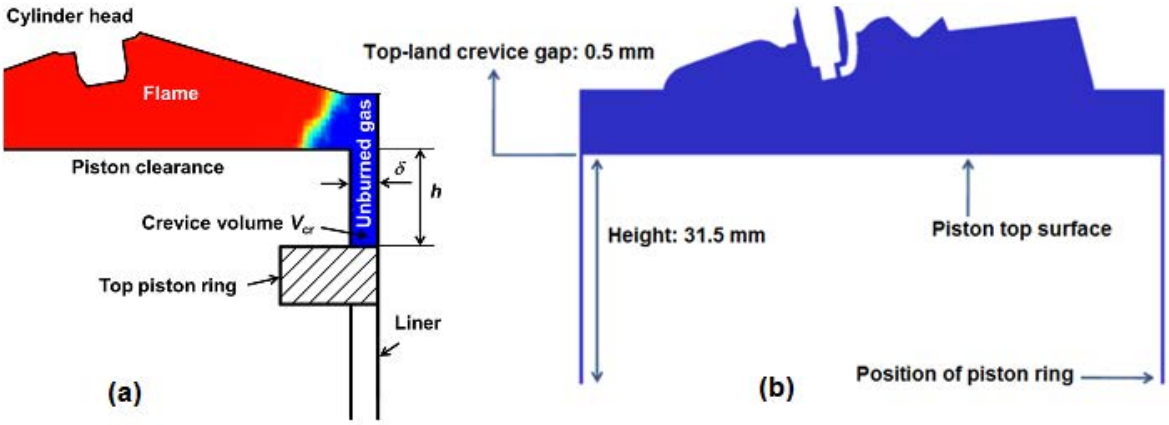

4.5 Numerical setup

This section will introduce the case setup of an engine simulation. The aim of this part is to be a guide for those who want to use OpenFOAM for this purpose, giving detailed information on the case structure, the setup of geometry, grids, boundary conditions, differencing schemes and the solver parameters.

The case setup of any CFD simulation starts providing the geometry of the problem. For this, the open source software Blender was employed. The geometry file is saved in the .stl format, so that it can be handled by the mesh generator. Besides, the boundaries have to be named consistently with their function: the inlet is named as Inlet, outlet as Outlet and so on.

As the mapping technique will be used to avoid high cell deformations, the entire four stroke cycle (720 CAD) was divided in intervals of 5 CAD. This means, it is necessary to build 144 different grids from different geometries with the engine in distinct positions within the cycle, as the piston and valves change their positions at different times.

In order to make it in an automatic manner, the *moveEngineSTL* tool was used. This C++ written tool is able to change the position of the points of a given patch from one engine geometry saved in the .stl format. So in order to build the geometries of an entire cycle at each 5 CAD, one only needs the geometry file with the piston at TDC and the valves at the positions related to the instant at the beginning of the cycle. In this work, the cycle starts at -360 CAD just at the beginning of the intake stroke. So the intake valves are starting to open, while the exhaust valves are still a bit open to simulate the valve overlap. Furthermore, it is

also necessary to inform details of the engine geometry and its rotation speed, so that it can calculate the position of the piston for each required time step. The valve lift profiles must also be given for the same reason.

With the geometries created, the meshing process can be initialized. For the meshing, the fully automatic tool *snappyHexMesh* from OpenFOAM was used. This utility generates 3-dimensional meshes mainly based on hexahedra elements automatically from triangulated surface geometries in Stereolithography (STL) format. The idea of this tool is to start from a starting mesh of perfect hexahedral elements and iteratively refine it, so that the mesh is conformed to the surfaces of a given geometry. The user can specify special refinement in smaller regions of the domain or where high derivatives are expected. The grids made by *snappyHexMesh* are therefore mainly composed of unstructured hexahedral elements. However, because the grids have to be conformed to the surfaces of the geometry and due to local refinement, some elements will split in different polygonal forms. As the described tool needs a starting mesh to work, the *blockMesh* utility will be used.

The principle of blockMesh is to generate meshes of perfect hexahedral elements by the decomposition of a domain geometry into a set of 1 or more dimensional blocks with the respective refinement in each direction. As described, the utility doesn't need much information to create high quality hexahedral grids. However, here again one has the problem of managing a large number of different domains, making the use of a shell script to automate the process necessary.

During the engine operation, only the domain within the cylinder continuously changes its size as the piston goes up or down. The parts of the domain accounting to the intake and exhaust pipes remain the same all over the cycle. Thus, the starting mesh made by *blockMesh* will always have a "T" shape, where the left and right arms cover the intake and exhaust pipes and its center the cylinder. However, as the piston moves the size of the "T" shaped domain must change and therefore one needs to track the movement of its bottom surface against the time for each one of the 5 CAD intervals. Figure 8 illustrates how the domain looks like with the piston at TDC.

The lowest points of the computational domain are located at the piston ring sealing the crevice volume. That being said, the lowest position of the starting mesh must always correspond to that location. For obtaining this position, the equation (26) is used.

$$p = p_{TDC} - \left((L_C + S/2) - S * \cos(\alpha)/2 - \sqrt{L_C^2 - (S * \sin(\alpha)/2)^2}\right) \quad (26)$$

The equation gives the location of the piston ring at every crank angle degree from the piston position at TDC and information about the engine geometry (connecting rod size L_c and stroke S). A shell script then starts the work of moving all the necessary files for the meshing (as the geometry files) from a folder named "Stock" and interval by interval, it runs the *blockMesh* utility and after it the *snappyHexMesh* utility. The closing of the valves is made using internal walls, which close the curtains between the valves and the cylinder head. The meshing process was performed in parallel using 48 processors, so that a good performance could be achieved. The number of cells at TDC is 2.2 million and at BDC it reaches 1.1 million, giving a mesh resolution of about 0.85 mm at the combustion chamber and 0.2 mm in the crevice gap. Due to special refinement in some regions, the minimum cell size reaches 0.125 mm at the valve seats during their minimum lift.

Figure 8 – Example of an starting domain created with blockMesh

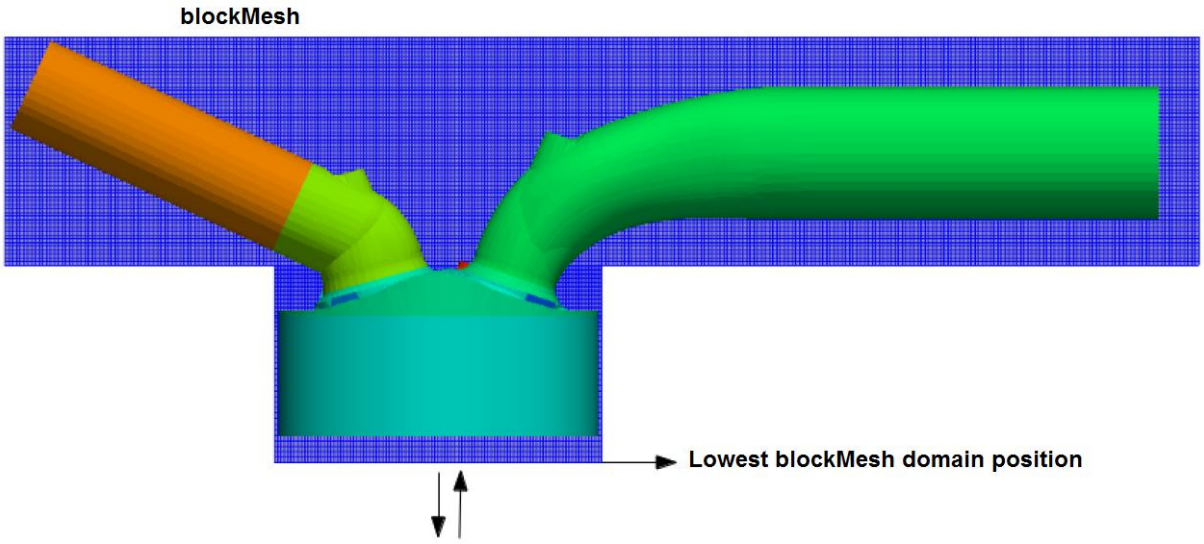

With all the grids ready, it is time to set up the simulations. For this, the structure of an OpenFOAM case (figure 9) will be presented. In OpenFOAM, a simulation case must be put in a directory with a well defined structure, which looks generally the same. A case directory always contains the system, constant and the time sub-directories.

Figure 9 – OpenFOAM case structure (OpenFOAM user's guide)

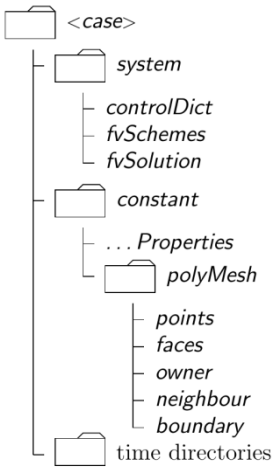

In "constant" it is located the polyMesh folder where information regarding the mesh is placed, i.e. the files defining the location of the grid points, cell surfaces and boundary faces. As OpenFOAM is able to deal with unstructured meshes, there must be also the files *owner* and *neighbour,* which contain labels to describe the connectivity between adjacent grid elements.

Furthermore, at "constant" are defined the physical properties (Appendix: frame 1) of the studied flow, parameters of the phenomenon of combustion (Appendix: frame 2), as well information regarding the engine geometry (Appendix: frame 3) and the mesh motion (Appendix: frame 4). The turbulence model and its parameters are also defined in dictionaries within this folder.

The frame 1 shows an example of the entries specified in the *thermophysicaPropeties* dictionary at the constant folder. These inputs are for simulations during the cold flow and at *thermoType* it can be seen that the energy equation is solved for the sensible internal energy, the JANAF thermodynamic tables are used for deriving the flow properties, the equation of state used is the one for a perfect gas and the Sutherland law is used for the transport properties. Besides, information regarding the mixture properties, as well the JANAF coefficients and their lower and upper limits must be provided there.

The model information on the combustion process is defined at the *combustionProperties* dictionary. Here the fuel (iso-octane) and its properties are defined and the flame kernel is specified. Its specification requires the start of the ignition (at -45 CAD), the flame kernel size, the spark duration and its strength (what in fact is the value designed to reaction source term in the c transport equation).

The frame 3 shows the information about the engine geometry provided in the *engineGeometry*. Moreover, the user has also to specify what patches are going to move, the origin, the axis and the direction of their movement in the *GDIdict* dictionary.

In the system sub-directory, there must be present the dictionaries *controlDict*, *fvSchemes* and *fvSolution*. At the *controlDict* dictionary, the user controls important parameters on the way how the solver should work during the run. There are defined the start and end time, the size of the time-step, the frequency that data are written among other important information regarding the operation of the simulation.

As already mentioned, the physical time in engine simulations is the crank angle degree. Using the definition of the current work, the cycle starts always at the beginning of the intake stroke at -360 CAD. That being said, the dictionary entries *start time* and *end time* will get as input the exact crank angle degree interval for each of the 144 time intervals available for the entire cycle. Each time interval will be put in a separate case named after the starting crank angle degree, from -360 until 355 at each 5 CAD (see figure 10). The generation of the case folders are made automatically with a shell script, which copy all the necessary files including the grids for each individual interval within the OpenFOAM structure (time folder, constant and system). The *controlDict* dictionary for the first time interval (from -360 CAD to -355 CAD) of the simulation is shown in frame 4.

As stated above, the start and end times for each case interval are given, as well the time value of the first time step. The following time steps will be automatically adjustable during the run, so that the maximum CFL number does not exceed the stability condition of 1. The CFL number is calculated as in equation (27).

Figure 10 – Engine case separated in different CAD intervals

The acronym CFL stands for Courant-Friedrichs-Lewy condition and is a necessary stability condition when performing time integration explicitly. If the CFL number is equal to one, the fluid has enough time to cross an entire control volume within one time step.

$$CFL = u\Delta t/\Delta x \tag{27}$$

in which u is the flow velocity, Δt is the time step and Δx the cell size.

After the generation of all the time directory files, the domain of each one of them must be decomposed so that parallel computing can be performed. For the domain decomposition, the dictionary *decomposeParDict* must be at the system folder, where the decomposition method and the number of cores are given. In this work, 192 cores have been used for the engine simulations and the decomposition is also made automatically with the aid of shell scripts for all intervals. Sub-folders with each decomposed domain part are added to the case folder with the processors' name plus the respective label with the decomposed part number: processor0, processor1, processor2 and so on.

The figure 11 shows a schematic representation of domain decomposition, with each color representing one processor sub-domain. Frame 5 (appendix) provides an example of the *decomposeParDict* dictionary.

Figure 11 – Domain decomposition (http://www.plasma-simulation-code.net)

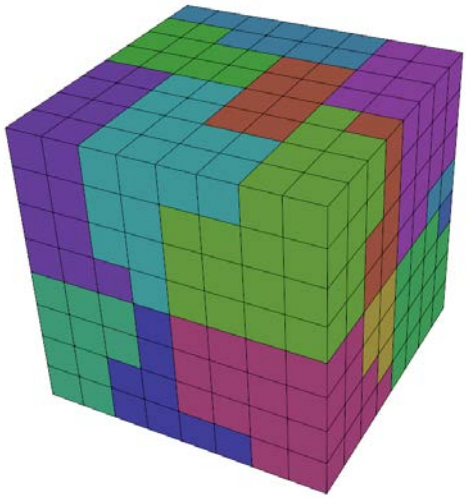

At *fvSolution*, the user should set the residuals and the linear solver for the solution of each discretised equation (velocity field U, pressure p, etc.). The available linear solvers distributed with OpenFOAM are summarized in the table 3.

Table 3 – OpenFOAM linear solvers

Solver	*Keyword*
Preconditioned (bi-)conjugate gradient	PCG/PBiCG
Solver using a smoother	smoothSolver
Generalised geometric-algebraic multi-grid	GAMG
Diagonal solver for explicit systems	diagonal

The working parameters of the algorithm used for the solution of the discretised equations as for instance the number of outer correctors during the PIMPLE loop can be defined in this dictionary. An example of the *fvSolution* is shown in frame 6 (appendix).

Finally, at *fvSchemes* the differencing schemes used for each term of the different discretised equations are chosen. They are divided in distinct categories regarding their mathematical meaning as interpolation, gradient, divergence, laplacian and time derivative schemes.

Each term of the governing equations can be discretised differently, according to the input given at each entry. An example of the *fvSchemes* dictionary is shown in frame 7 (appendix).

The new differencing scheme for the convective term of the momentum equation based on the Mach-number is defined here with the name *limitedLinearMachCreviceV*. For the scheme to work, it is necessary to create a variable called Mach, so that the Mach number is calculated for each control volume cell. Therefore, the scheme checks this variable value and apply the CDS our TVD scheme accordingly. The time integration is performed using the implicit backward scheme.

Table 4 – Boundary conditions

U field boundary conditions	
Inlet	pressureInletOutletVelocity
Outlet	pressureInletOutletVelocity
Static walls	No-slip condition
Moving walls	movingWallVelocity
p field boundary conditions	
Inlet	Pressure profile from experimental data
Outlet	Pressure profile from experimental data
Walls	zero-gradient
T field boundary conditions	
Inlet	InletOutlet (301.65 K)
Oulet	InletOutlet (301.65 K)
Intake walls	300 K
Exhaust/Cylinder walls	333 K

Now before the description of the whole engine solution, the setup of the boundary conditions will be explained. The boundary conditions for velocity, pressure, temperature and all the necessary variables are placed always at the first time directory of each time interval. The boundary condition of the variable U (velocity field) is assigned to a text file called U, for the pressure to the file p, for the temperature to the file T and so on. The computational

domain is divided into patches, so that one can assign different boundary conditions to distinct regions of the domain.

The table 4 summarizes the boundary conditions at different regions for the velocity, pressure and temperature fields.

At the walls of the domain, no-slip and constant temperature conditions are assumed. To the pressure at the inlet and outlet are assigned pressure profiles obtained by experiments. The *pressureInletOutletVelocity* boundary condition assigned to the inlet and outlet velocity boundary conditions applies *zeroGradient* on all components, except if there is inflow at the outlet or outflow at the inlet. In these cases, a fixed value condition is applied to the tangential component. The movingWallVelocity boundary condition is applied to the moving walls (piston and valves). Finally, the *inletOulet* condition for the temperature applies *zeroGradient* to the inlet if the flow there is inwards and to the outlet if the flow there is outwards. Otherwise, fixed value conditions will be applied.

The valve lifts are given also from profiles obtained by experiments. These profiles are stored in text files located at the case directory and read by the GDIdict dictionary in the constant folder. Figure 12 shows the valve lift profiles.

Figure 12 – Valve lift profiles

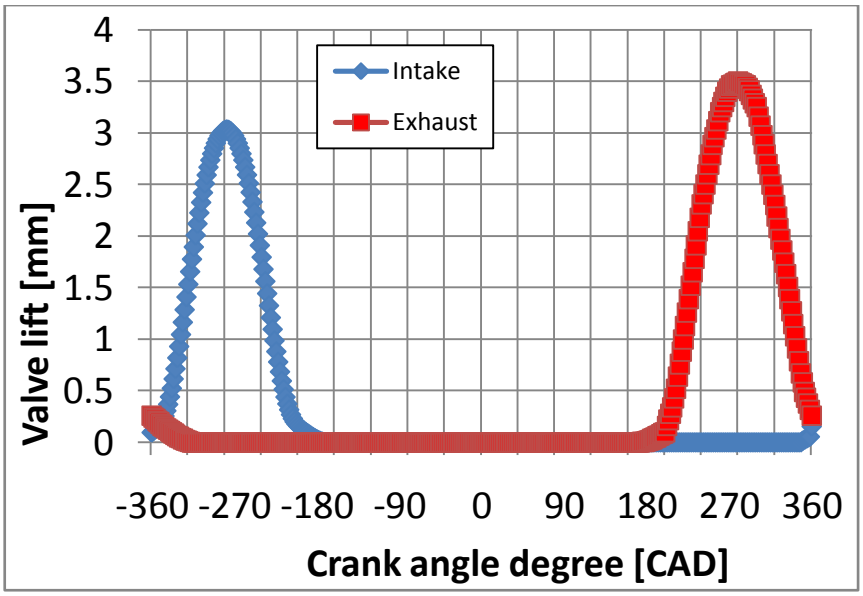

After completing all the step-by-step described above, the simulation of the cold flow can be started. For this, shell scripts are also employed to automate the process, running the solver named as *sonicDyMEngineFoam* in parallel using 192 cores. The cycle is started from the intake stroke during the valve overlapping. This means that the intake valves are opening

while the exhaust valves are still closing and air flows directly from the intake to the exhaust pipes, due to the pressure gradient created by the descendent movement of the piston. This scavenges the burned gases from the combustion chamber, cooling it down. In accordance with the current definition, the initial time step is defined as -360 CAD. After the interval of 5 CAD, the solution is stopped and its results mapped to the next case directory at -355 CAD and so on. The mapping procedure is also made in parallel, what makes the work flow very efficient.

At -320 CAD the exhaust valves fully close, as the piston continues its downward movement. Then finally at -176 CAD, only 4 CAD before the piston reaches the bottom dead center, the intake valves are also found fully shut and at -180 CAD the compression stroke begins. The domain remains fully closed until the final instants of the expansion stroke at 172 CAD, when the exhaust valves start to open. The cycle ends when the piston reaches the top dead center again at 360 CAD. In this work, two cycles of the cold flow at an engine speed of 1500 rpm were performed.

To simulate a port fuel injection condition, the variable ft (fuel mass fraction) was initialized with a value of 0.0623 (stoichiometric condition) all over the intake pipe. A transport equation for ft was added to the solver, so that the fuel mass fraction was transported by the turbulent flow induced inside the cylinder.

For the combustion, the solver named as *sonicDyMEngineFlameFoam* was used. This solver is similar to the previous one, with the addition of the combustion models described in detail in the 4.3.3 subsection.

As the present model does not have a physical ignition model, the ignition is triggered simply by increasing the value of the reaction source term of the progress variable transport equation to 8000 W in the vicinity of the spark plug during 10 CAD. The size of the combustion kernel must be also provided to the model and this was obtained by visualization of the flame from experiments just after the ignition timing (-45 CAD).

For the simulation of the combustion process, a similar shell script to the cold flow is used. The -45 CAD time folder (start of ignition) is copied to a separate directory, so that the flow at this point is assumed as initial condition for the combustion case. The maximum velocity magnitude inside the domain prior to ignition is not higher than 15 m/s, but the flow in the combustion chamber is still quite turbulent. The maximum CFL number is kept as 0.1, so that a fully CDS scheme can be applied to the convective terms of the c transport equation.

4.6 Results: Cold flow

In this work, two complete cycles under motored conditions were calculated and their results will be presented in this section. First, some probe locations are defined (figure 13), from where the variables of interest are extracted and plotted. Further, the results obtained for each stroke within the cycle are addressed, i.e. intake, compression, expansion and exhaust. Snapshots, vector and streamline plots are shown for different quantities and in order to validate the model, the pressure traces from the simulations will be compared with experimental data and analytical solutions.

Figure 13 – Probe locations

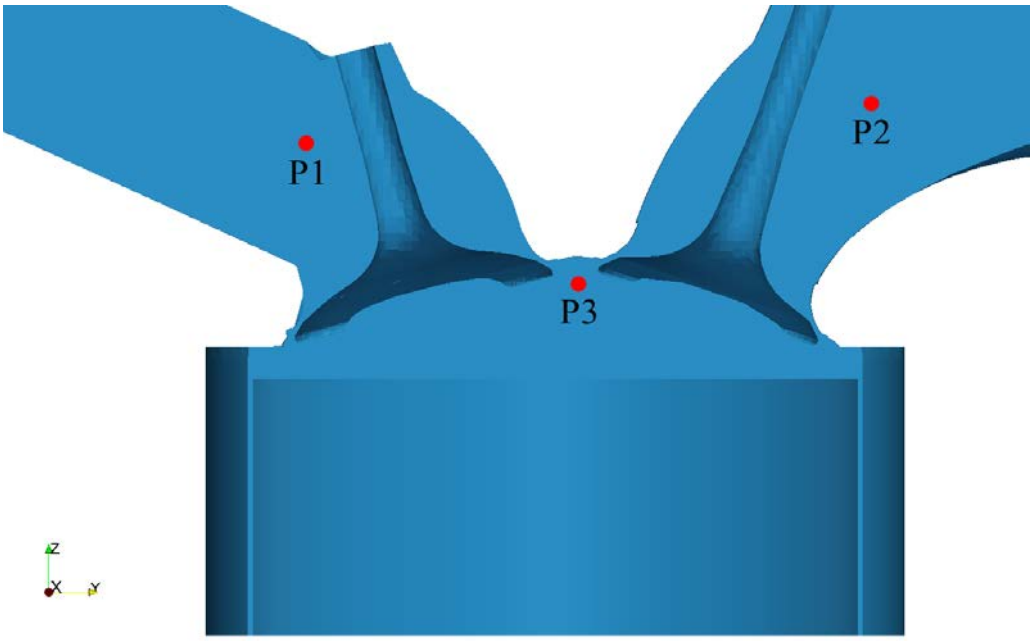

In figure 13, points P1 and P2 are located on the plane through the engine valves in the intake and exhaust pipes respectively. The point P3, on the other hand, is located at the top of the combustion chamber right in the middle of the cylinder.

Next, the results from the intake stroke will be presented. As already mentioned, following to the definition used within this work, the engine cycle begins at the valve overlap at -360 crank angle degrees, with the piston at TDC and going down, the intake valves starting to open and the exhaust valves still closing.

4.6.1 Intake stroke (from -360 CAD to -180 CAD)

The transient pressure values for every crank angle degree within the entire cycle were obtained from experiments. Figure 14 presents the comparison from the results obtained for the two different cycles against these data at the location P1.

Figure 14 – Pressure trace during the intake stroke at P1

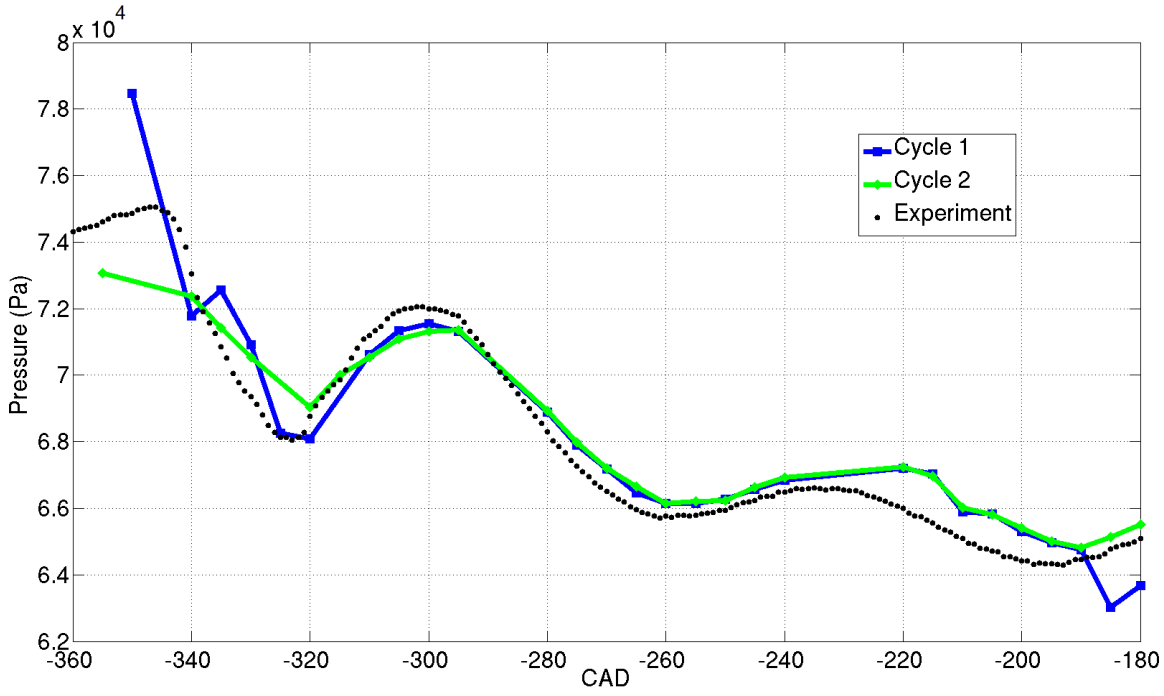

As the piston moves down, a pressure gradient is created inside the cylinder so that the mixture is pushed from the intake pipes into the combustion chamber. The pressure at the inlet/outlet patches are given by profiles obtained from experiment. The inlet pressure varies between 0.65 and 0.85 bar and the outlet pressure between 0.85 and 1bar within the entire cycle.

Due to the complexity of the intake/exhaust pipe geometries, their sizes could not be represented entirely in the numerical model. This fact has the advantage of reducing the numerical domain and thus the computational effort but it may difficult the agreement of the calculated pressures with experimental data in the intake and exhaust pipes. However, figure 14 shows that the model obtained good agreement for the pressure at the intake pipe (P1) during admission for both cycles. The pressure differences at -360 CAD and -180 CAD may be explained by oscillations generated during the simulation start (-360 CAD) and the intake valves closure (-180 CAD).

Figure 15 - Pressure trace during the intake stroke at P2

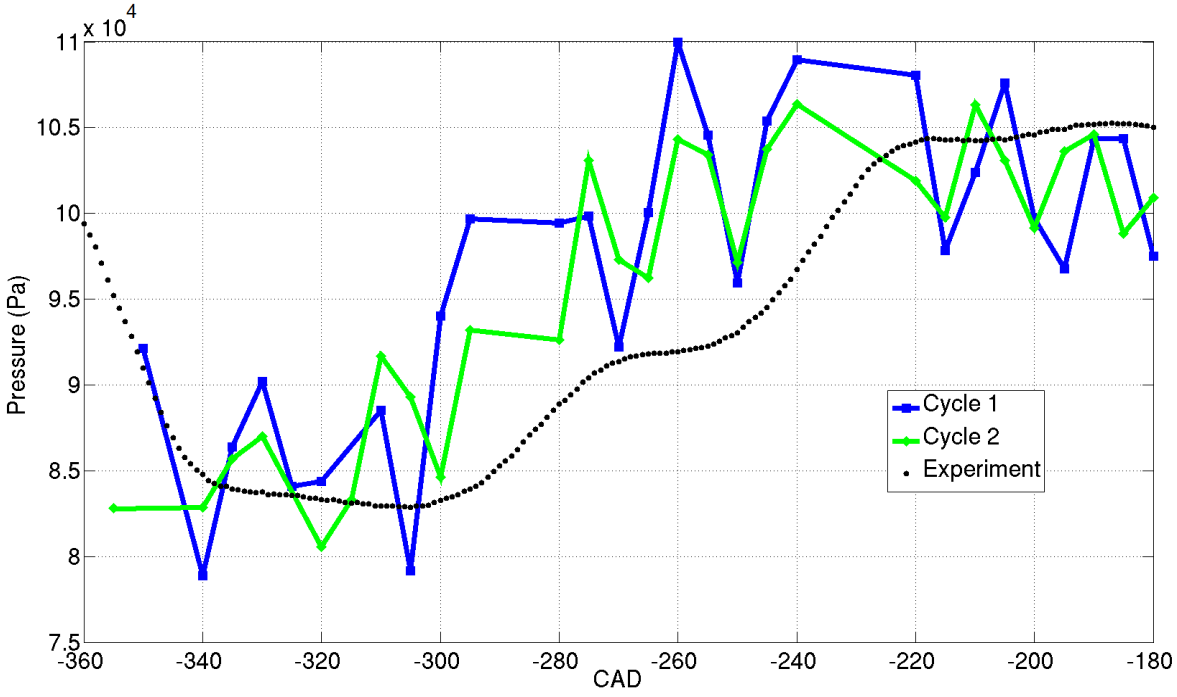

Figure 15, on the other hand, points out that at the exhaust pipe (P2) the calculated pressures oscillate around the experimental pressure trace during admission. These oscillations may be explained by the short size of the exhaust pipe, due to reflections of pressure waves at different walls of the domain and lack of grid refinement at the walls. The abrupt closure of the exhaust valves at -320 CAD (table 5 summarizes the valves opening and closing) may also introduce waves, which are transported through the entire exhaust domain.

The location P3 represents the position where the in-cylinder pressure is measured. In comparison with the experiments, both cycles slight over predicted the experimental trace as indicated by figure 16. This over prediction can be explained because the present model neglect energy losses from the engine like mechanical friction, heat and pumping losses.

Table 5 – Intake and exhaust valves opening/closing

Stroke	*Timing (opening/closing)*
Intake	350 CAD / -176 CAD
Exhaust	172 CAD / -320 CAD

Figure 16 - Pressure trace during the intake stroke at P3

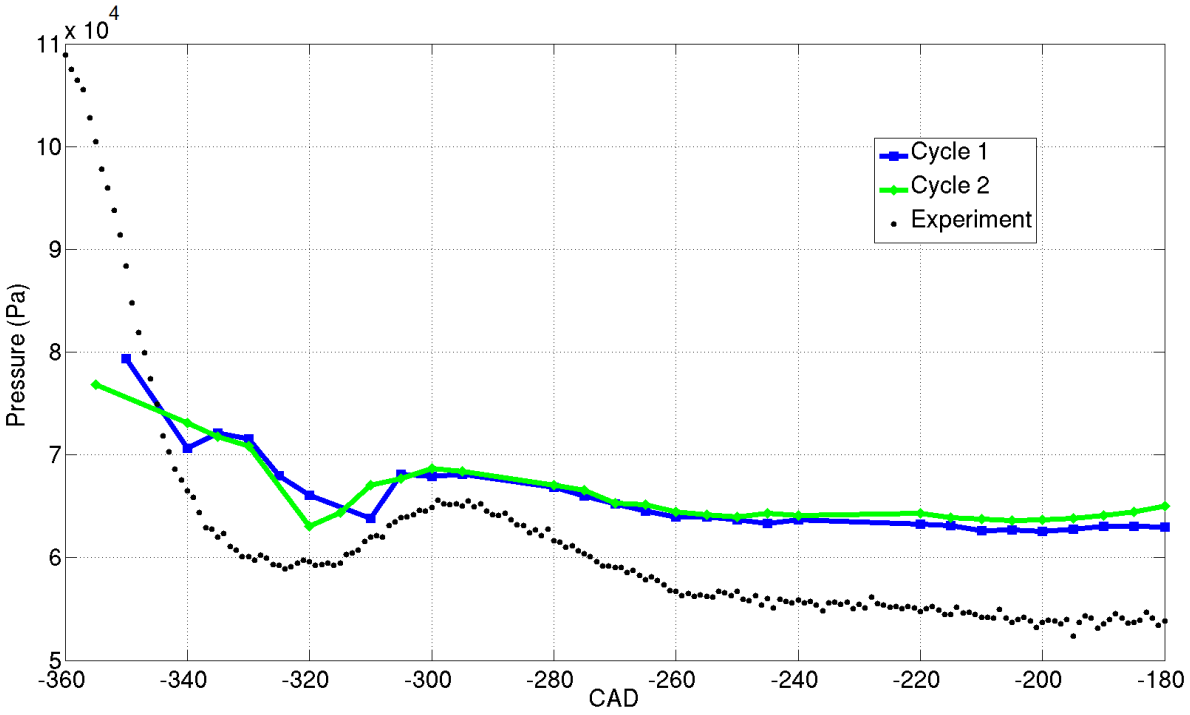

Figure 17 shows snapshots of the temperature (a) and pressure (b) from the first cycle at the maximum lift of the intake valves at -270 CAD, taken within a plane through the valves. At the same instant, velocity snapshots for magnitude (a) and all three Cartesian components (b, c and d), as well a velocity vector plot (e), are presented in figure 18.

Figure 17 – Temperature and pressure snapshots from the first cycle at -270 CAD

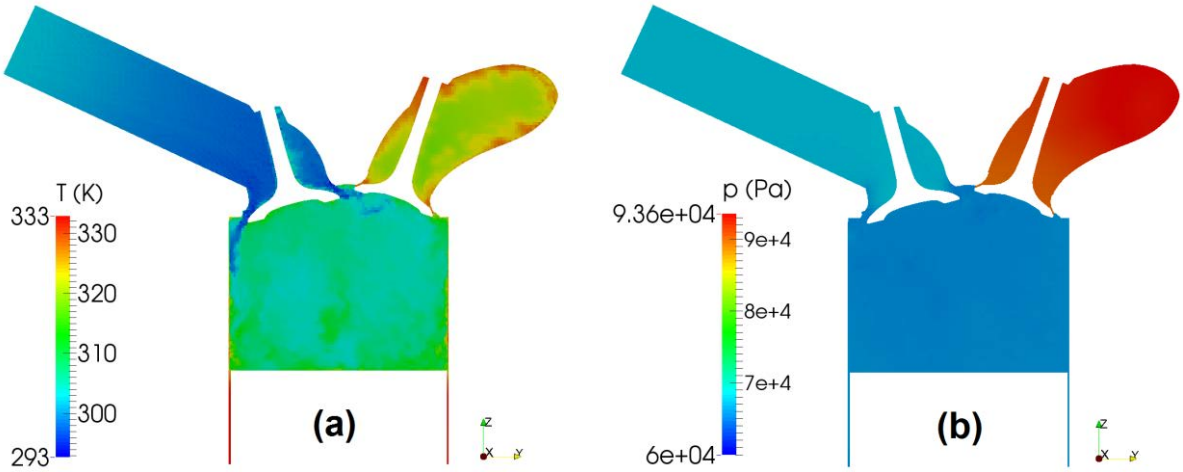

Figure 18 – Velocities snapshots and vector plot at -270 CAD

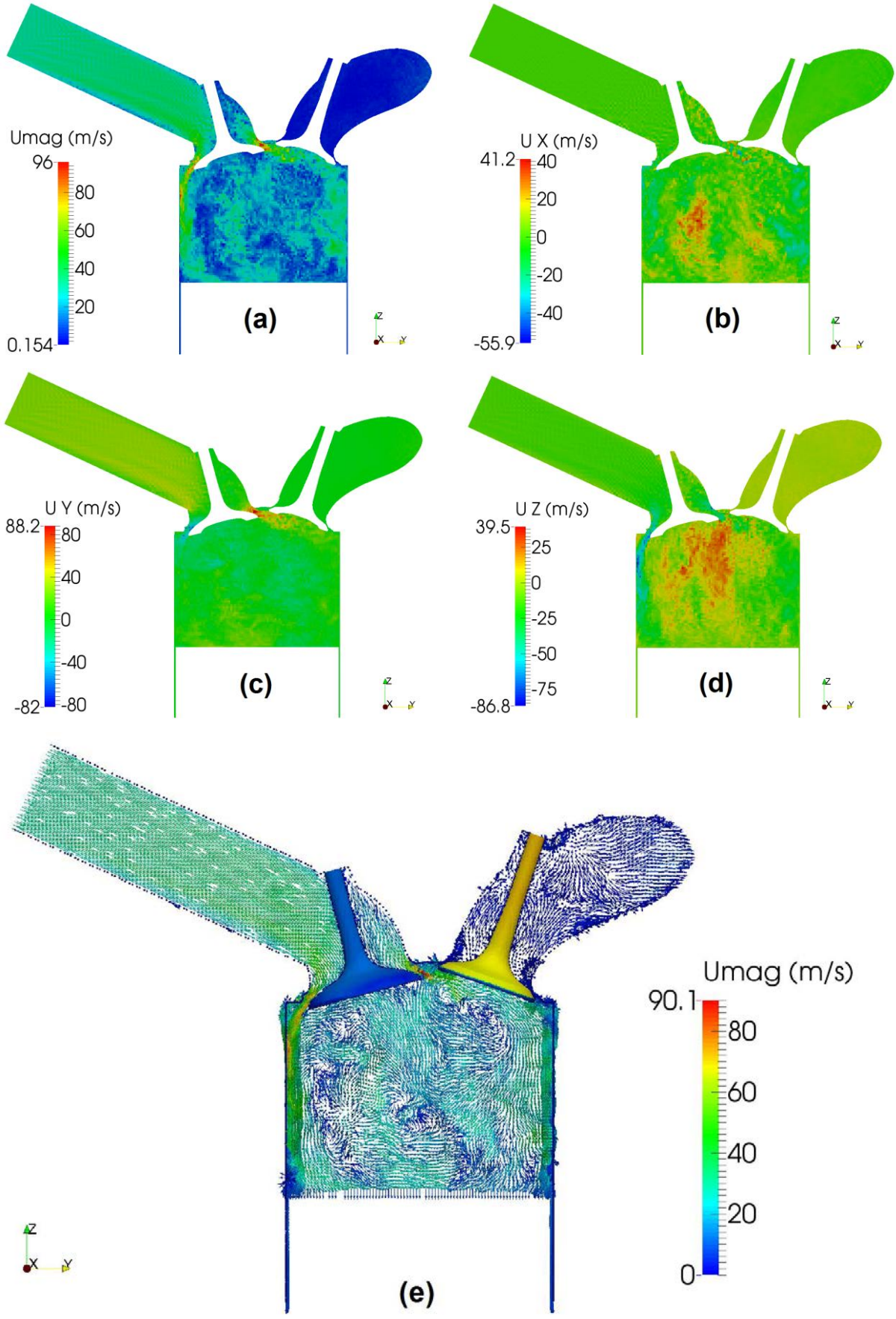

Figure 19 – Resolved Turbulent Kinetic Energy in a plane under the spark-plug

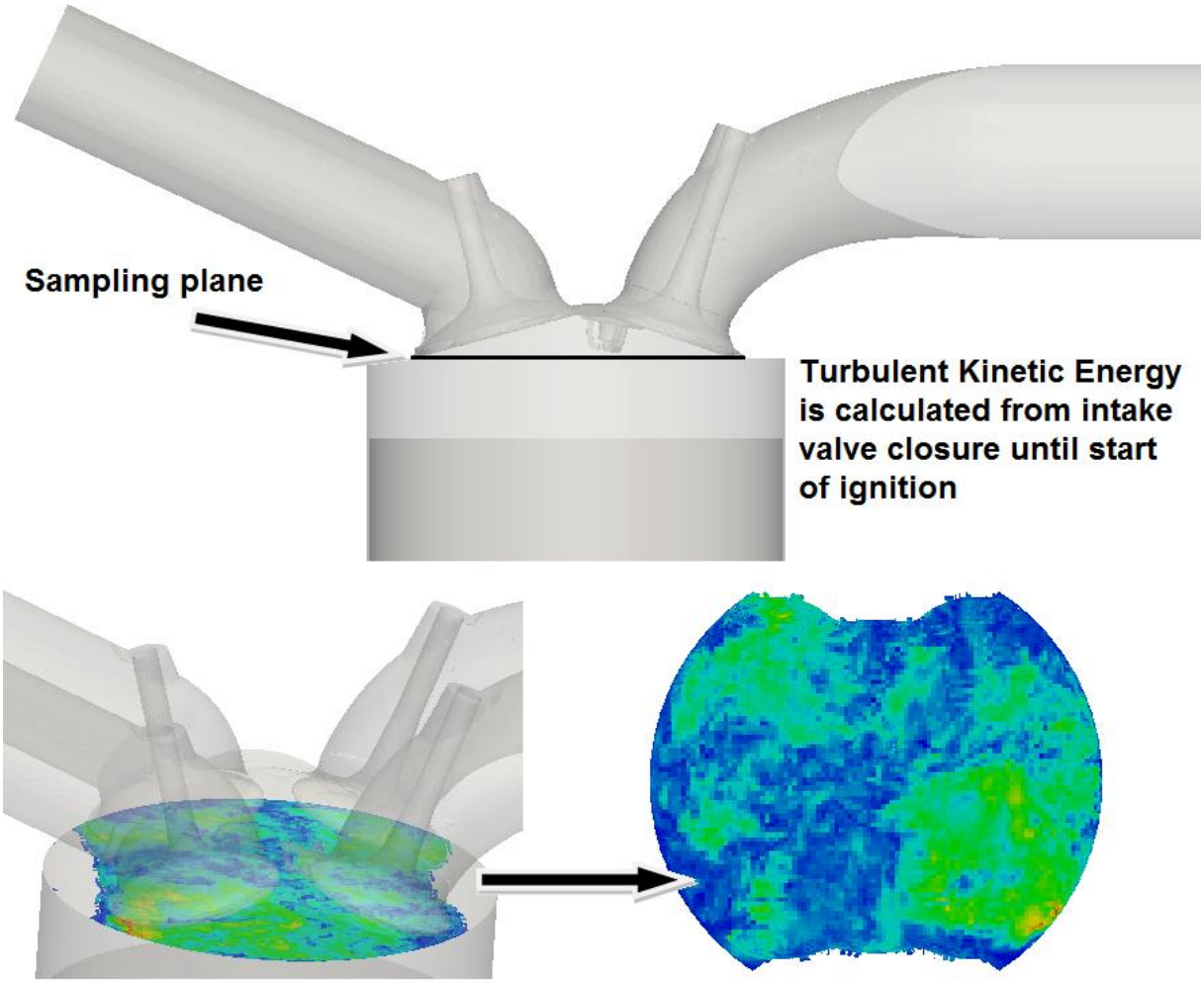

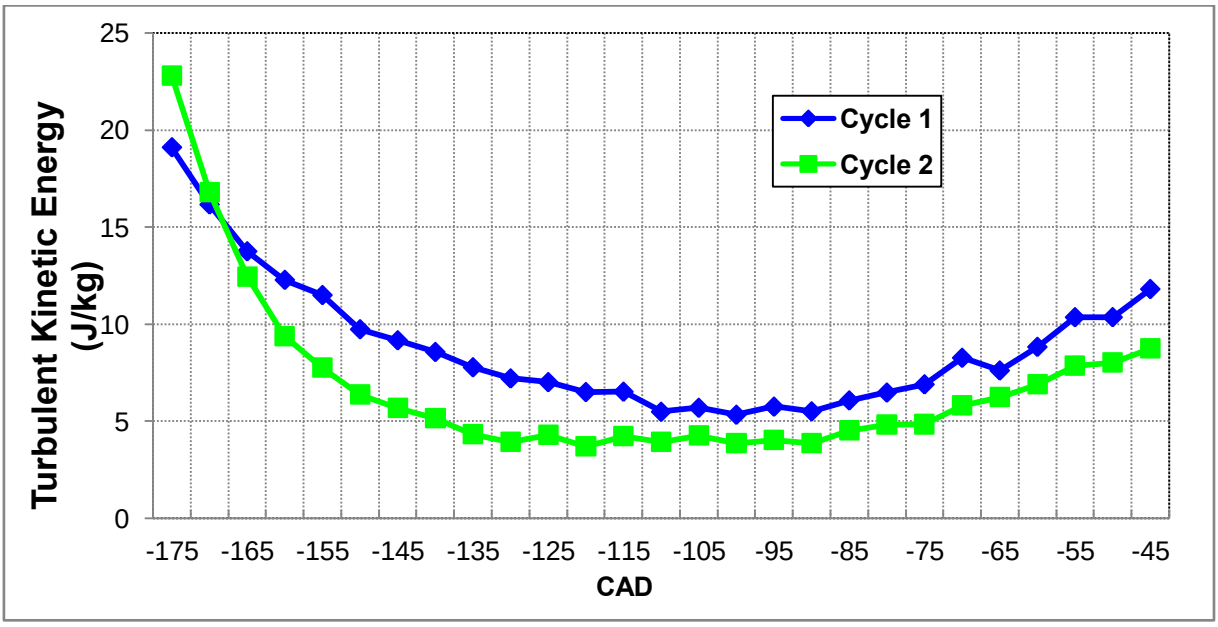

Figure 18 shows the ability of LES in capturing very small structures of the turbulent flow field due to higher resolution than those applied in RANS simulations and the direct solution of the turbulent scales bigger than the filter width. Within the intake stroke, strong tumble movement is created and much of the turbulence generated is still there (figure 19) prior to ignition, ensuring efficient mixture and good combustion quality.

4.6.2 Compression and Expansion (from -180 CAD to 180 CAD)

After the admission of the mixture into the cylinder, the cycle continues with the compression stroke. As the piston goes up towards TDC, the mixture is compressed, increasing the pressure and temperature inside the combustion chamber. The flow field at the end of the compression is still turbulent but turbulence starts to decrease since the closing of the intake valves. Because of its feature of improving the mixture process, turbulence is essential to a good combustion quality and its intensity should be kept within a minimal value prior to ignition. Therefore, special care is necessary in the choice of numerical schemes for the momentum equation, so that too dissipative schemes such as first order accurate upwind are not selected. Too much dissipation would eliminate turbulence completely and this would impact the combustion efficiency in a negative manner. Even higher order TVD schemes can be very dissipative with LES and thus the use of a hybrid CDS-TVD was advised in this work. As one can see in figures 20 and 21, the flow velocity field from the first cycle at -55 CAD (10 CAD before ignition) is still quite turbulent.

Figure 20 – Velocity plots from the first cycle at -55 CAD for magnitude (left) and x (right)

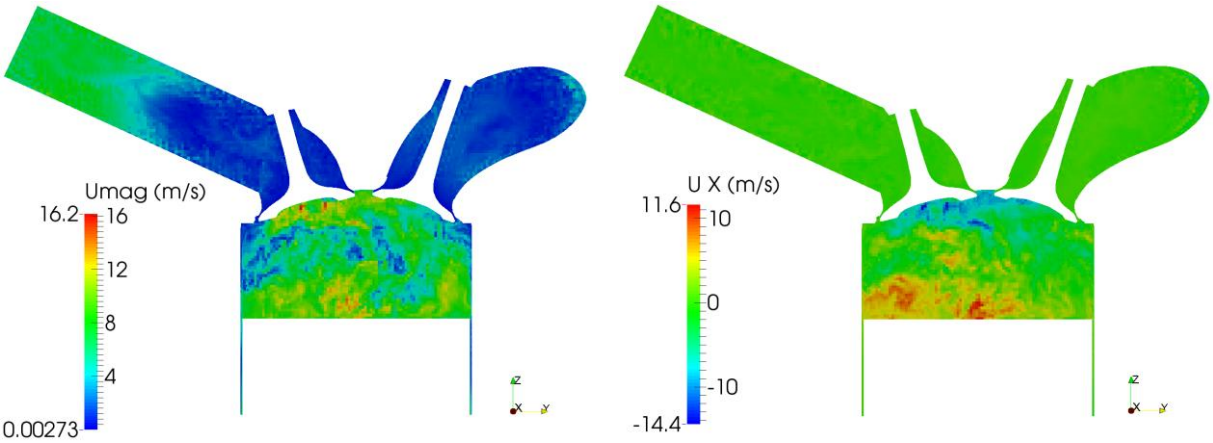

Figure 21 - Velocity plots from the first cycle at -55 CAD for y (left) and z (right)

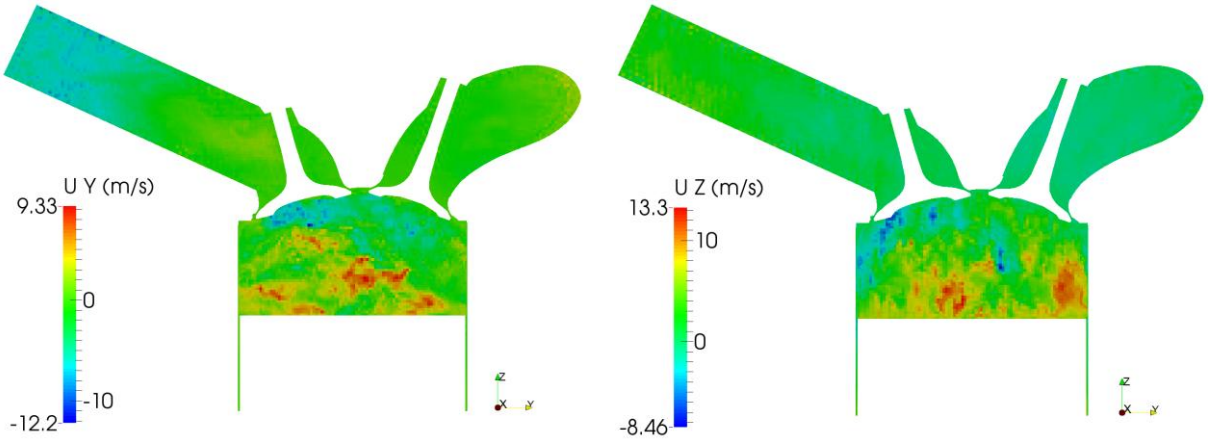

The figure 22 shows snapshots of the temperature (a) and pressure (b) for the same instant (-55 CAD). As the charge is compressed in a ratio of 10:1, temperature and pressure inside the cylinder increase.

Figure 22 – Temperature and pressure snapshots from the first cycle at -55 CAD

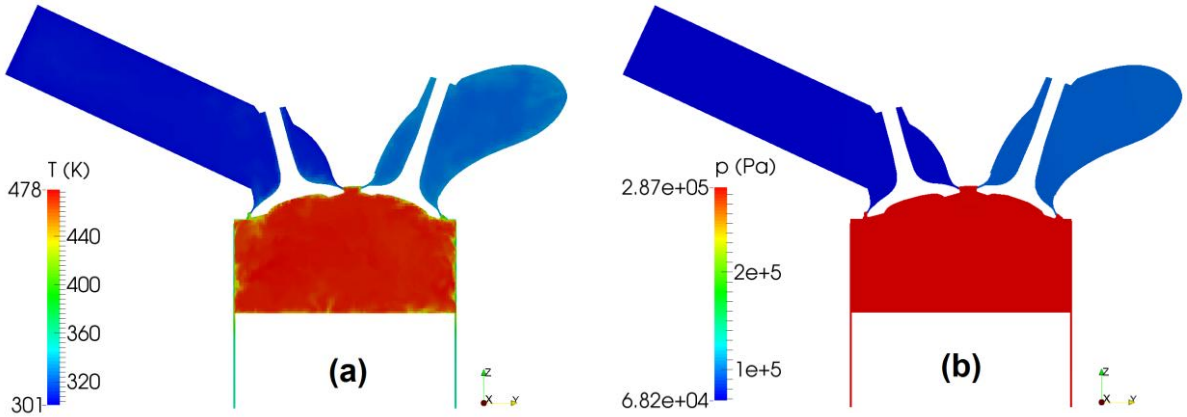

In order to validate the model, the in-cylinder pressure from -180 CAD to 180 CAD is compared with the analytical solution of the adiabatic compression of a volume domain using the same compression ratio of the engine simulations, i.e. 10:1. This comparison is shown in figure 23. The modeled peak pressure is under predicted in both cycles because the model considers heat transfer through the walls by setting constant temperatures at the domain walls. For this reason, a thermo dynamical engine 0D model developed at the University of Duisburg was also employed for comparison, in which the heat transfer through the walls can be switched on and off.

Figure 23 – In-cylinder pressure from -180 CAD to 180 CAD

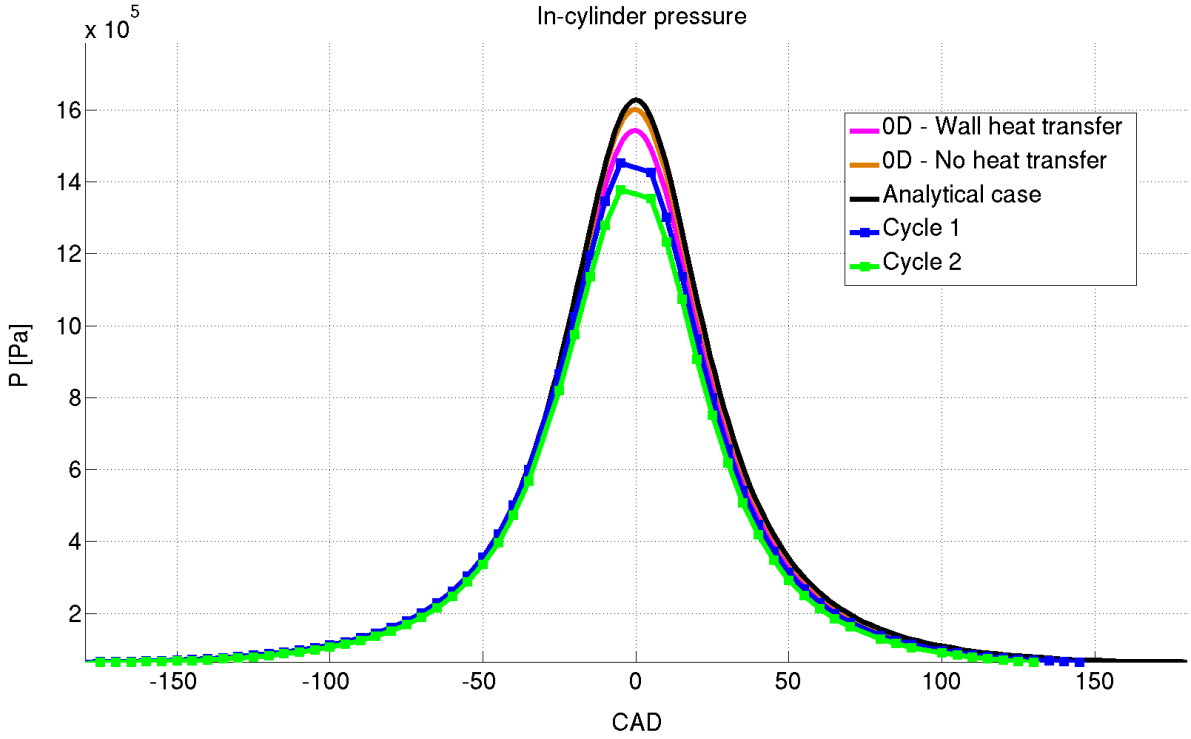

Both cycles agree well with the 0D Model with heat transfer through the walls, although the peak pressure is still slightly under predicted. This difference may be explained again by the under prediction of heat transfer at TDC due to consideration of constant wall temperatures and also due to lack of refinement at the walls.

4.6.3 Exhaust stroke (from 180 CAD to 360 CAD)

Finally, at 180 CAD the exhaust is started. The piston is found at BDC, the intake valves are closed and the exhaust valves are opening. As the piston starts to move up, the in-cylinder charge is expelled outwards the engine. Due to the higher pressures inside the exhaust pipes in comparison with the pressure in the combustion chamber prior to the opening of the valves, some back flow is observed entering the cylinder just after the valves lift.

As already done for the intake stroke, the transient pressures at the probe locations P1, P2 and P3 from the simulation are compared with the available data from the experiment. Moreover, snapshots of the flow velocity, temperature and pressure at a certain instant of the exhaust stroke are hereafter presented.

In figure 24, the pressure trace at the intake pipe (P1) during the exhaust stroke is compared with the experiment. Further in figure 25, the pressure traces of both cycles are compared at the probe location in the exhaust pipe (P2).

Figure 24 – Pressure trace during the exhaust stroke at P1

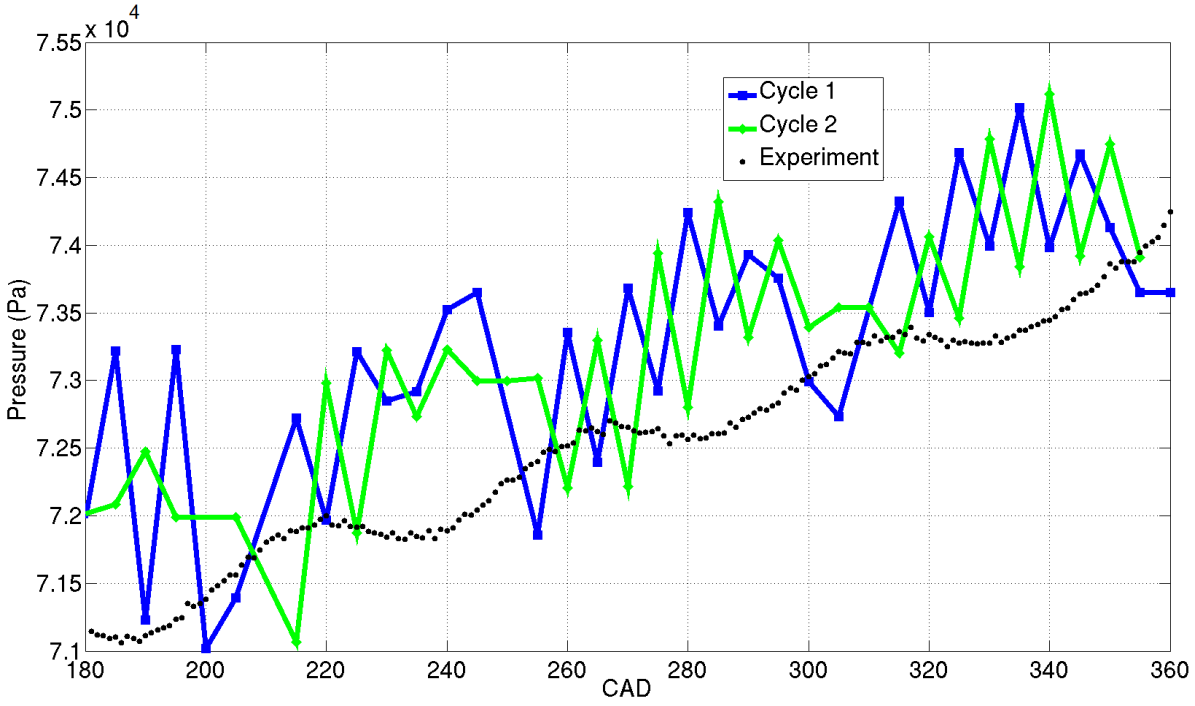

Figure 25 - Pressure trace during the exhaust stroke at P2

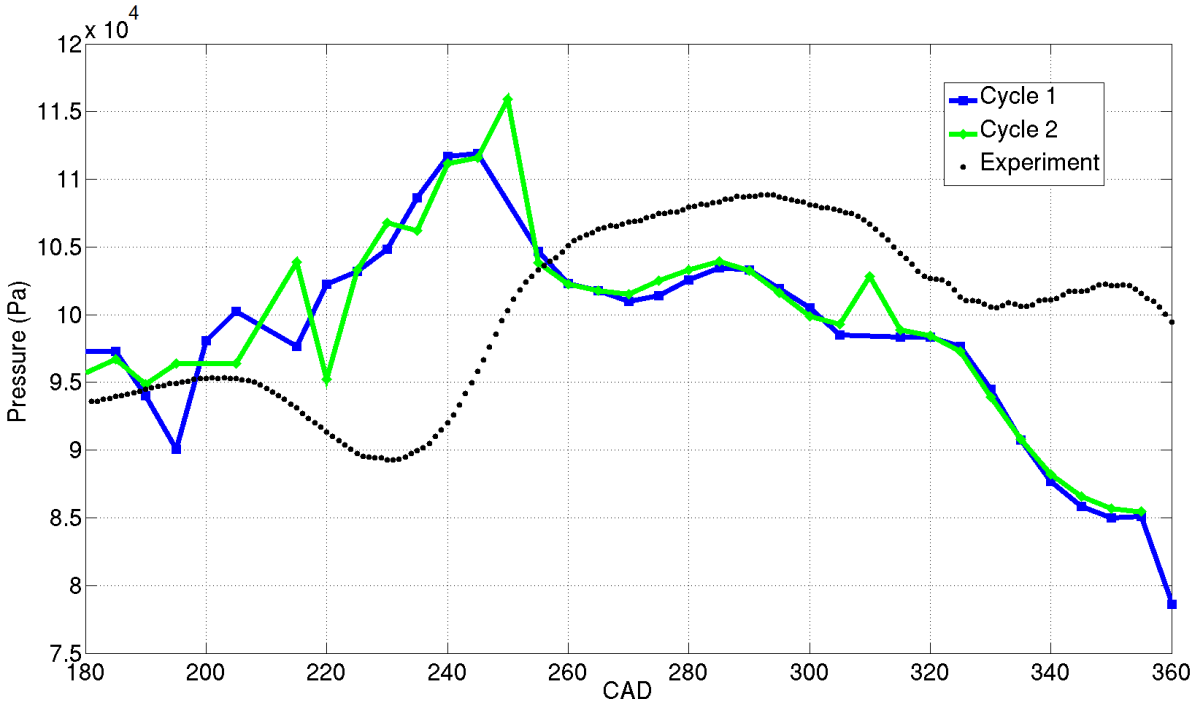

The in-cylinder pressure of both cycles is confronted against the experiment during exhaust in figure 26.

Figure 26 - Pressure trace during the exhaust stroke at P3

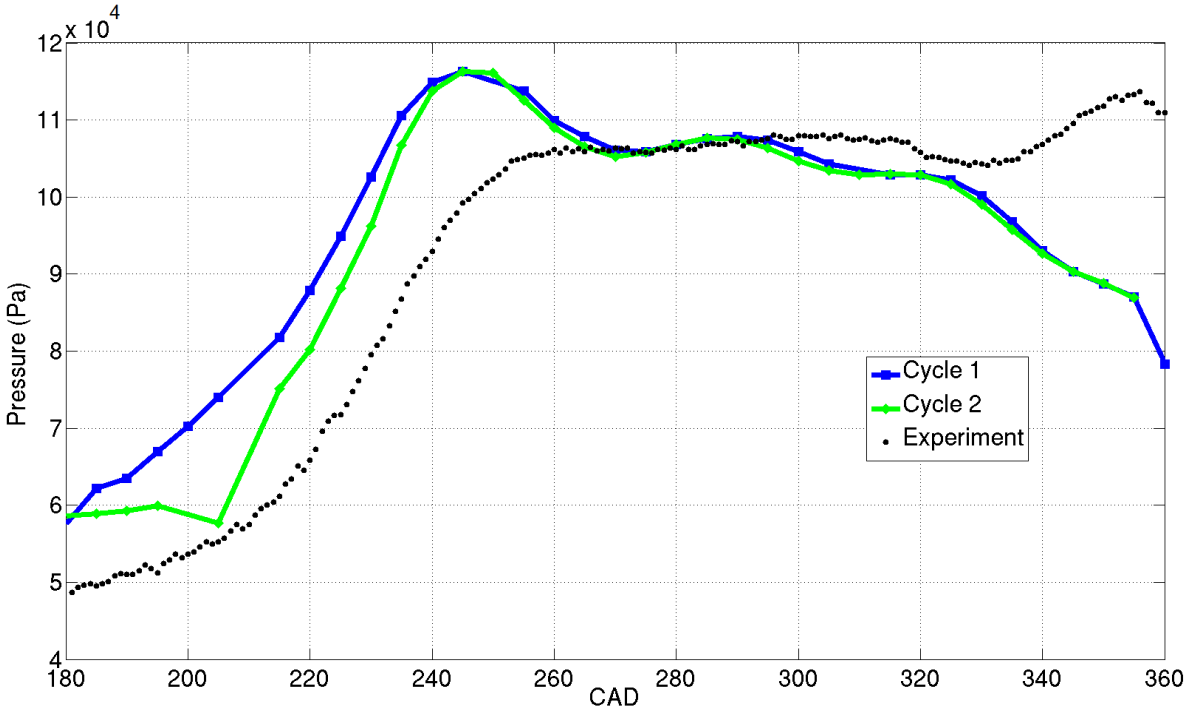

The pressure differences observed at P2 (figure 25) and P3 (figure 26) at 360 CAD may be explained by the abrupt closure of the exhaust valves.

Figure 27 shows snapshots of the temperature (a) and pressure (b) from the first cycle at the maximum lift of the exhaust valves at 270 CAD, taken within a plane through the valves. At the same instant, velocity snapshots for magnitude and all three Cartesian components are presented in figure 28.

Figure 27 – Temperature and pressure snapshots from the first cycle at 270 CAD

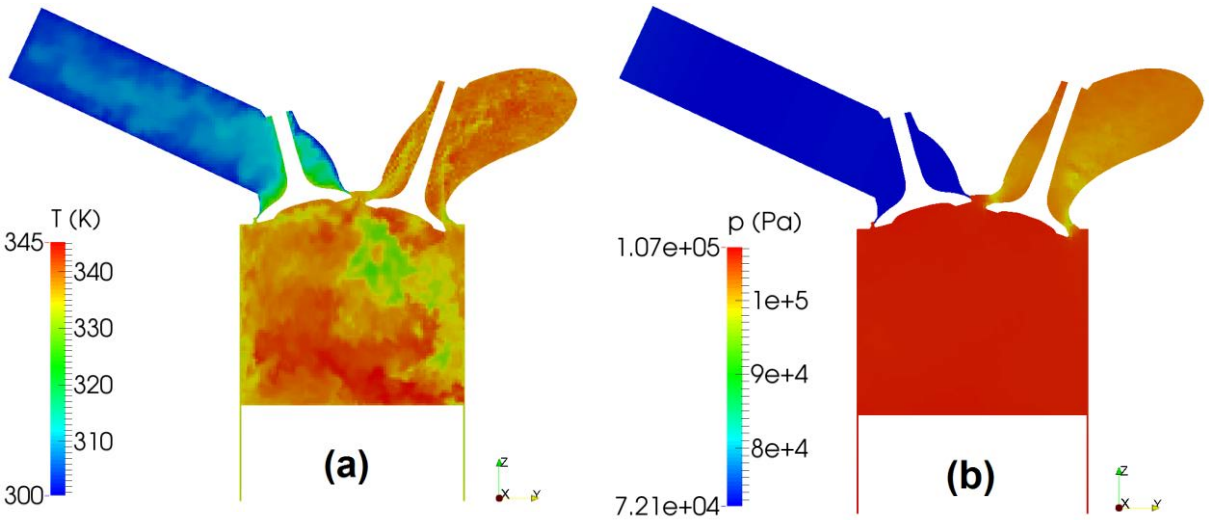

Figure 28 - Velocity plots from the first cycle at 270 CAD

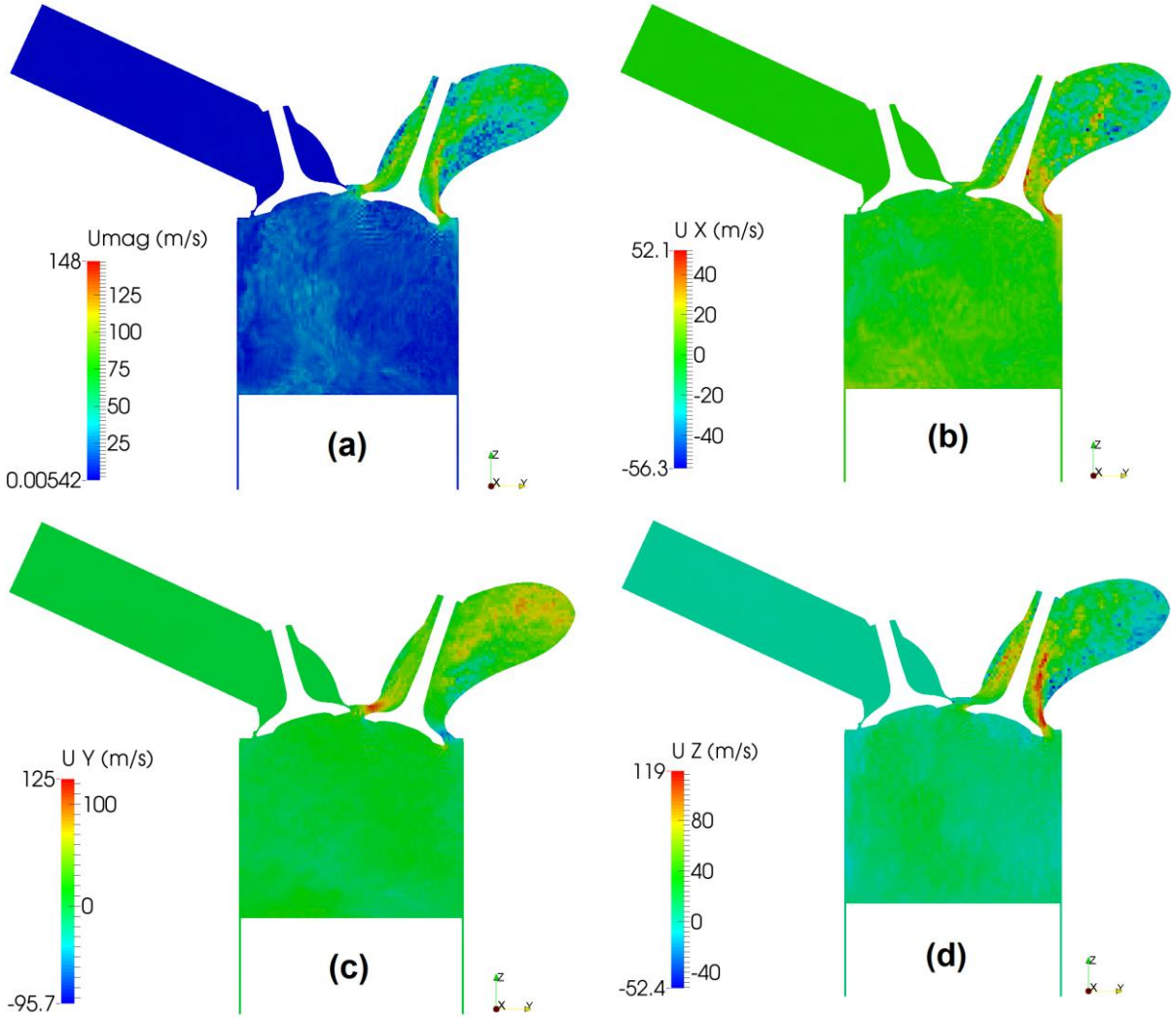

Here the results concerning the cold flow in the Duisburg engine were presented. Next, the results of the combustion process will be addressed. For this, the results obtained from the cold flow simulations at -45 CAD (ignition timing) are used as initial conditions. Details about this numerical setup were explained in section 4.5.

4.7 Results: Combustion

Now the results regarding the combustion process of the Duisburg Engine will be presented. In this work, an investigation of the effect of the crevice volume on the performance of the combustion in port fuel injection spark ignition engines was performed. From the studied engine, high speed flame visualization was obtained from experiments, showing a luminous front inside the top-land crevice volume. In order to asses if the visualized structure is a wrinkled flame instead of luminous zone of residual gases that are pushed into the crevice, large eddy simulations were conducted to study this phenomenon.

Figure 29 – LES (left) volume rendering of an iso-surface of the combustion progress variable vs. experimental (right) high speed visualization of visible chemiluminescence.

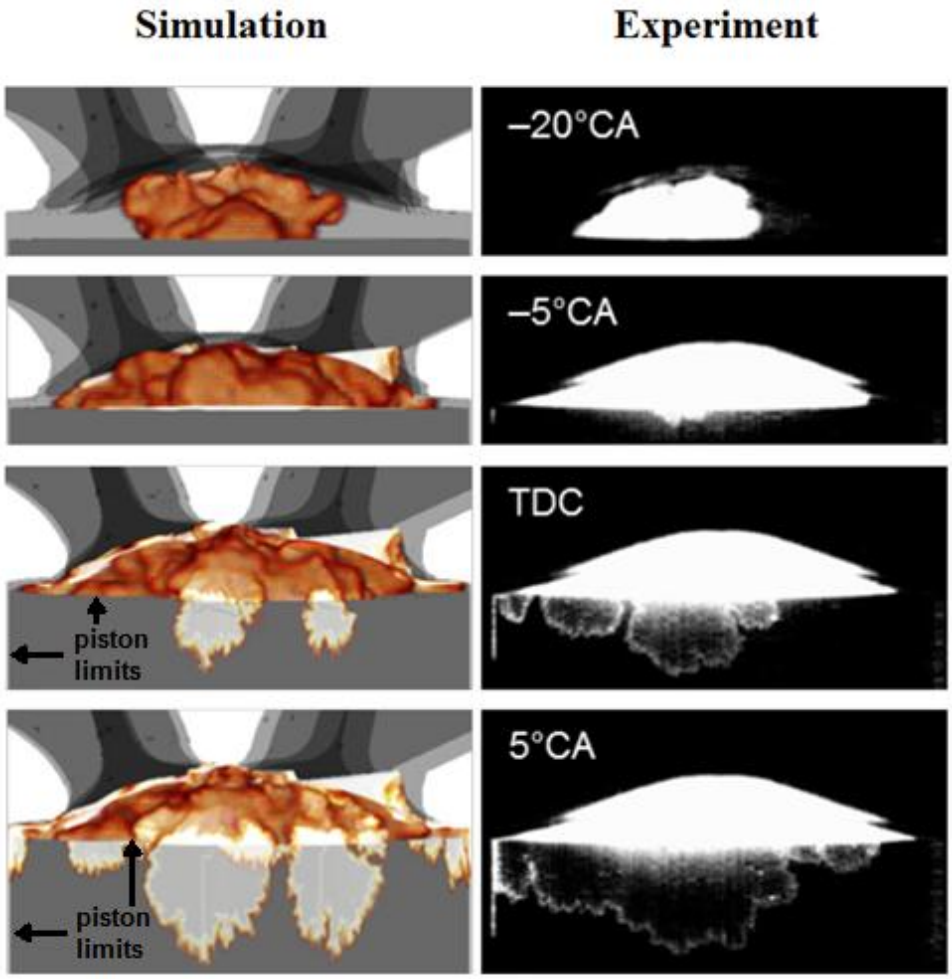

The figure 29 shows a qualitative comparison from the volume rendering of an iso-surface of the combustion progress variable obtained from the large-eddy simulation against the high speed visualization of visible chemiluminescence obtained by experiment from a

single cycle. In the simulation, the reaction source term is "switched on" ($\bar{\dot{\omega}} = S_L \rho_u \Sigma_{\text{gen}}$) inside the crevice volume in order to represent the case of a reacting flame within it.

In the simulation, the flame penetrates into the crevice approximately 5 CAD later in comparison with the experiment. However, the similarity of the flame structure in both LES and experiment is high, denoting a good qualitative agreement of the model with the experimental data. The structures show also that the wrinkled flame forms distinct single regions inside the crevice, defined here as "islands". These islands are created because the flame front reaches the top land crevice entrance at different instants and locations, as one can observe in figure 30.

Figure 30 – Volume rendering of the progress variable at -10 CAD (left) and TDC (right)

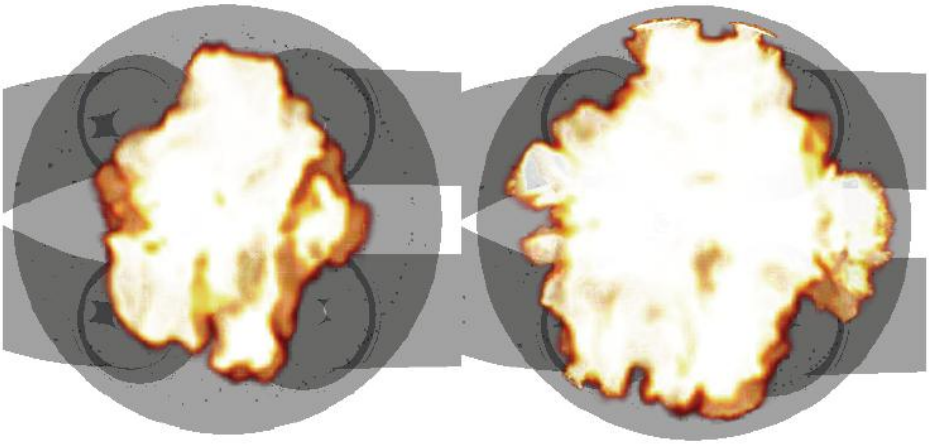

The flame evolves in a non-uniform way and thus when the piston reaches the top dead center, some regions of the flame already arrived at the crevice gap as others don't.

Figure 31 – Effect of the reaction source term on the simulation inside the crevice

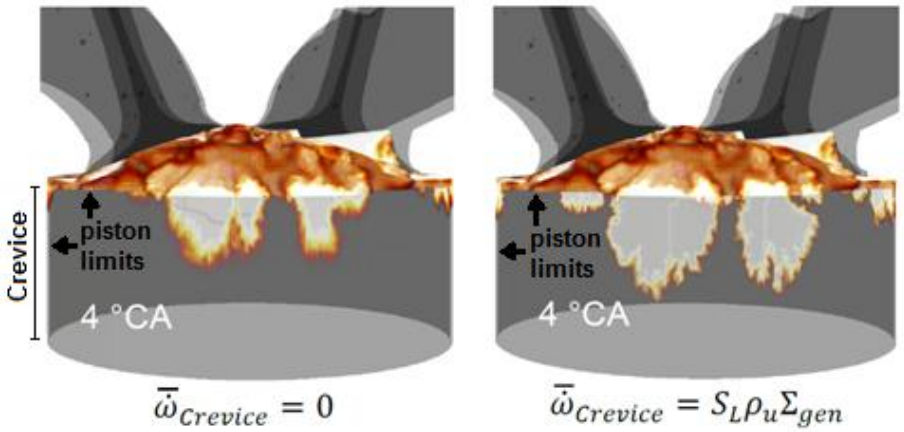

The simulation was restarted but this time with the reaction source term "switched off" by setting $\bar{\dot{\omega}} = 0$ inside the crevice volume, so that the flame penetrates into the gap only by convective and diffusive transport. This configuration aims to simulate the flame quenching at the crevice entrance with the residual gases being pushed into the gap due to the movement of the piston and the high pressure inside the combustion chamber. As expected, in the case where the reaction source term is off, smaller island structures are observed inside the crevice for a specific instant. Figure 31 compares the simulation with the reaction source term switched on with the one with reaction source term switched off inside the crevice volume.

Furthermore, the flow velocities of 25 m/s at the crevice opening at TDC push the burned/unburned frontier less deep in the case with no reaction. This boundary penetrates into the crevice by the action of any turbulent flame speed achieved at this operation point (1500 rpm) during the combustion process. The appearance of the observed structures is also consistent with a burning flame.

When the piston reaches 10 CAD, some backflow is observed from the crevice volume to the combustion chamber, as illustrated by figure 32 for the case with reaction.

Figure 32 – Vertical velocity snapshot at 10 CAD pointing out backflow to the chamber

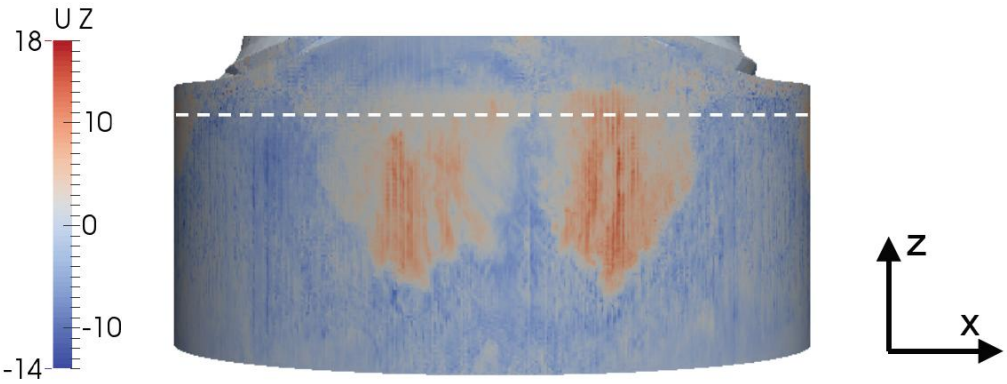

As the piston starts moving down and the pressure in the combustion chamber therefore reduces, the gases inside the clearance gap are pushed back into the cylinder. This is the phenomenon responsible for most emissions of unburned hydrocarbons in engines. A great amount of gases are trapped in the crevice during the compression stroke and because of the low temperatures of the crevice walls compared to the ones in the combustion chamber, most of this trapped charge is not burned and flows back to the cylinder.

Figure 33 shows snapshots of the combustion progress variable at the crevice outer walls.

Figure 33 – Flame penetration at 10 CAD without reaction (left) and with reaction (right)

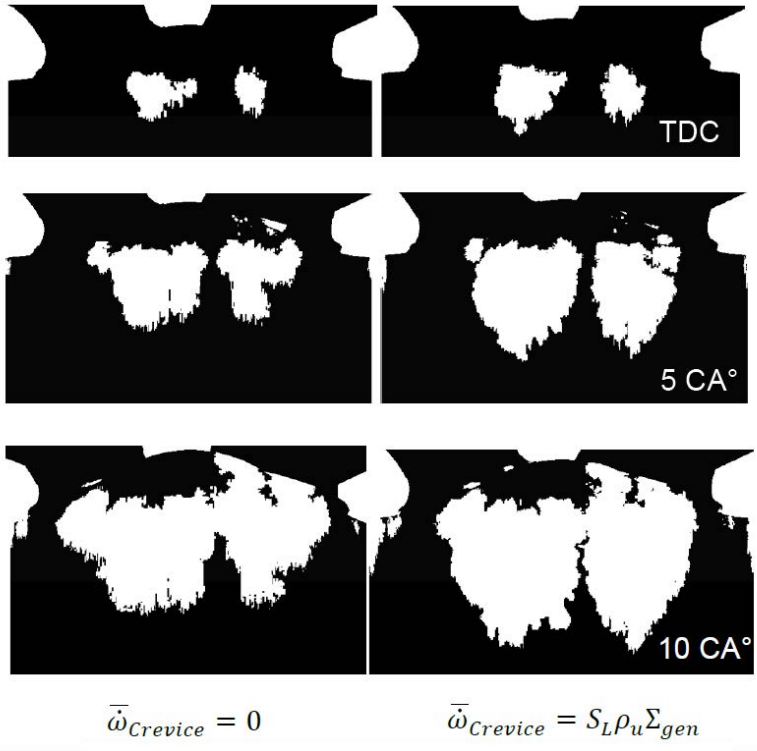

The later unification of the flame islands in the case with reaction source term switched off in comparison with the case where it is switched on, is consistent with the idea that the structures observed from the high speed visualizations from experiments are indeed an actively burning flame propagating into the crevice.

Figure 34 – Burned mass inside the crevice with and without reaction source term

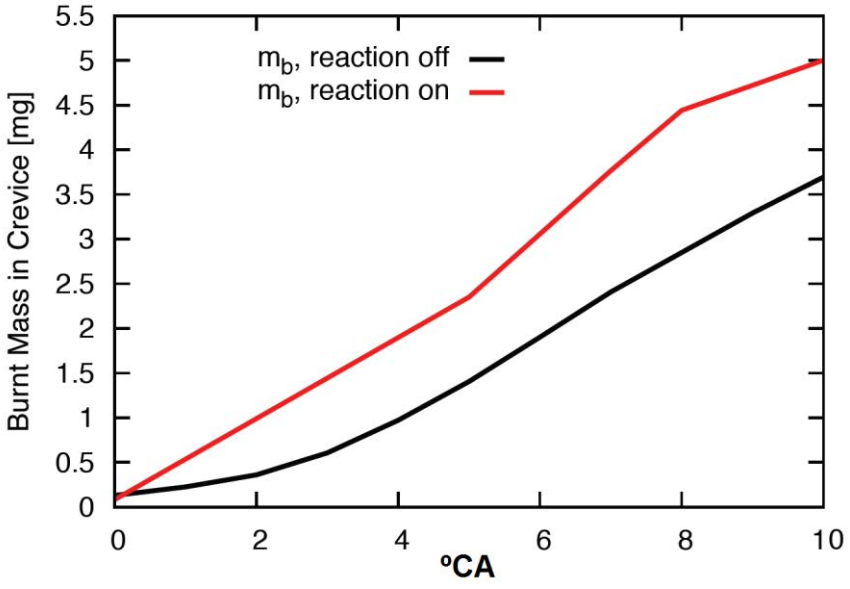

Figure 34 is a plot of the burned mass inside the crevice volume for the case without reaction (black) and for the case with reaction (red). As expected, for the case with reaction 30% more burned mass is present at 10 CAD. This is also consistent with the literature about experimental studies on engine crevices and UHC-Emissions.

Figure 35 – Flame propagation colored by progress variable (left) and temperature (right)

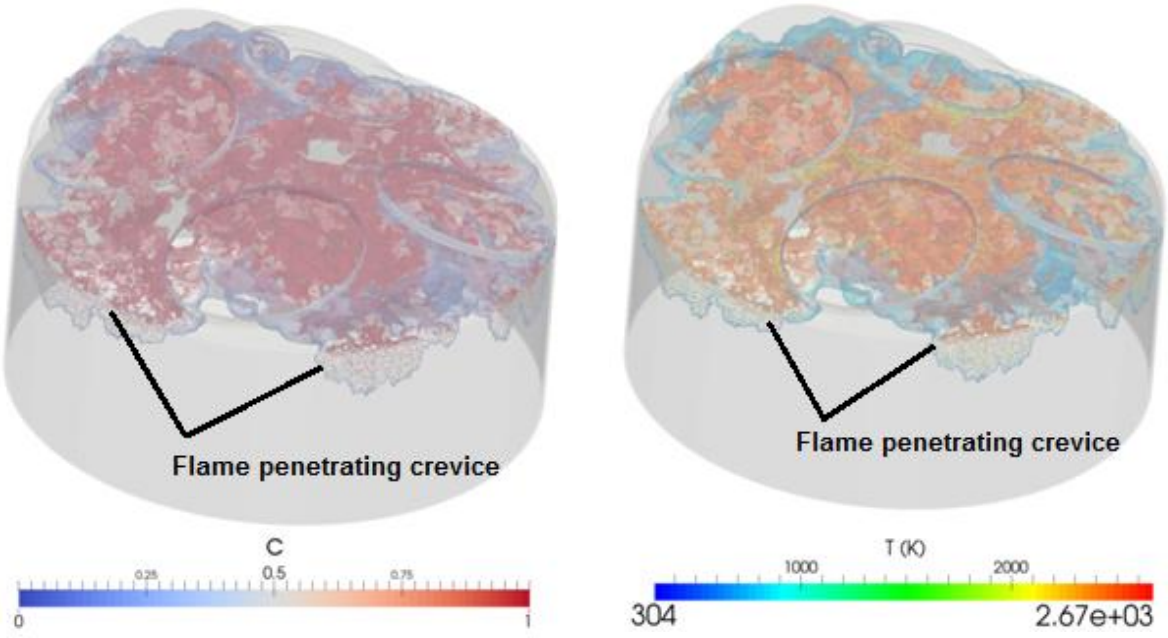

Figure 35 illustrates the flame propagating inside the combustion chamber and penetrating into the crevice gap. In the left plot, the flame is colored by the progress variable, which quantifies how much of the mixture was already burned (0 means fully unburned and 1 fully burned). On the other hand, the right plot is colored by the temperature.

The last two subsections presented the results obtained from the engine simulations conducted within this work. The next chapter will address the second part of this work, which is on the modeling of gasoline fuel sprays inside a combustion chamber. The simulation setup and results are explained and detailed.

5 SPRAY MODELING

In this chapter, the models regarding the simulation of fuel-sprays will be discussed. First, the most relevant information on the break-up of spray jets and droplet formation will be addressed. Then, the numerical solver and its mathematical models accounting to the exchange of momentum and energy transfer between the gas phase and the injected drops will be detailed. Further, the test case used for the code validation will be presented. To finish, the results will be exposed and discussed.

5.1 Fuel-sprays

Stratified-charge combustion is a promising research area to pursuit the strict legislation standards imposed to the industry in order to reduce emission in engines. Therefore, careful studies on spray formation, droplet evaporation and mixture processes are necessary to develop detailed numerical models and experimental configurations to allow a change from the standard port-fuel injection to the modern state of art direct-injection engines. These engines have the potential to improve the quality of emissions and decrease the specific fuel consumption.

The study of fuel sprays comprehends different kinds of phenomena occurring during a narrow period of time: droplet formation and breakup, exchange of momentum, heat transfer between species in different states, mass transfer from liquid to gas phase, multiphase flow, spray combustion and so on. Some of these phenomena will be addressed and explained now in detail.

5.1.1 Basic breakup concepts of liquid jets

In multiphase flows, as in the case of a liquid spray-jet being injected into a gaseous ambient, there are different kinds of mechanisms to produce the spray droplets from a round continuous liquid jet. Reitz and Bracco (1986) distinguished among four different breakup regimes, the Rayleigh regime, the first and second wind-induced regime and the atomization regime.

To study these different breakup regimes, it is necessary to define the dimensionless liquid Weber number. This number is a relation between the aero-dynamical forces tending to break up the jet into droplets and the surface tension at the liquid-gas interface, which tends to keep the jet in its original form. Equation (28) shows the liquid Weber number:

$$We_l = \frac{u^2 D \rho_l}{\sigma} \tag{28}$$

One can calculate the dimensionless Reynolds number in equation (29) and thereby derive the dimensionless Ohnesorge number in equation (30), which includes all relevant fluid properties (ζ: surface tension at the liquid-gas interface, ρ_l: density of liquid and μ_l: dynamic viscosity of liquid). The Ohnesorge diagram in figure 36 can then be constructed, describing the different regimes according to the liquid phase properties.

Figure 36 – Ohnesorge diagram: (1) Rayleigh regime (2) First Wind-induced regime (3) Second Wind-induced regime (4) Atomization regime (BAUMGARTEN, 2005)

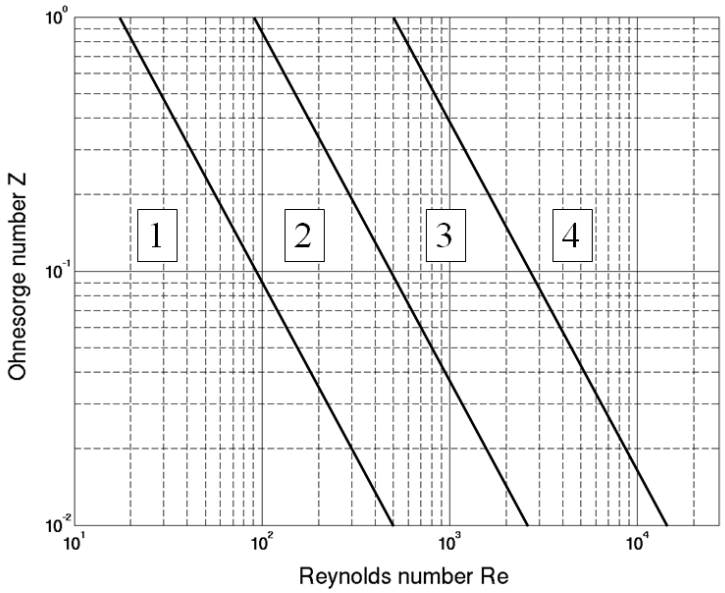

$$Re = \frac{uD\rho_l}{\mu_l} \tag{29}$$

$$Z = \frac{\sqrt{We}}{Re} = \frac{\mu_l}{\sqrt{\sigma \rho_l D}} \tag{30}$$

A jet needs to reach at least a minimum velocity to be formed, otherwise at very low velocities drip flow will occur. Increasing the velocity u, a continuous flow will start to take place during the so called Rayleigh regime (1). In this regime, the first droplets are formed due to the oscillations generated by inertia and surface tension forces and the characteristic diameters of these first drops are greater than the injector nozzle diameter.

An increase of the velocity results in a decrease of break-up length, the average droplet diameter becomes similar to the nozzle diameter but the biggest ones are still multiples of the nozzle size. This regime is the first wind-induced (2), where the gas phase Weber number $We_g = u^2_{rel} D\rho_g/\zeta$ becomes relevant to the jet description.

The next regime is the second wind-induced (3), where the flow inside the nozzle becomes turbulent. The turbulence leads to break-up, which is amplified by aerodynamic forces due to the exchange of momentum between gas and liquid phase.

For a further increase in the velocity, the atomization regime (4) takes place and the droplet surfaces reaches very small values downstream to the nozzle tip. An unbroken jet still can be found at small distances from the inlet or at least a very dense spray of very small particles. This regime is relevant for direct injection engines, since the much reduced drop diameters increase the velocity of evaporation from the liquid to the gas phase.

5.1.2 Basic breakup concepts of liquid droplets

After the primary breakup from the liquid jet into the first spray droplets summarized in the last sub section, the spray-jet particles are subject of secondary break-up. The secondary break-up can also be categorized in several regimes.

Baumgarten (2005) distinguishes among five different liquid drop break-up regimes: vibrational break-up (1), bag break-up (2), bag / streamer break-up (3), stripping break-up (4) and catastrophic break-up (5). The figure 37 illustrates each one of them.

Figure 37 – Droplet break-up according to Wierzba (1993)

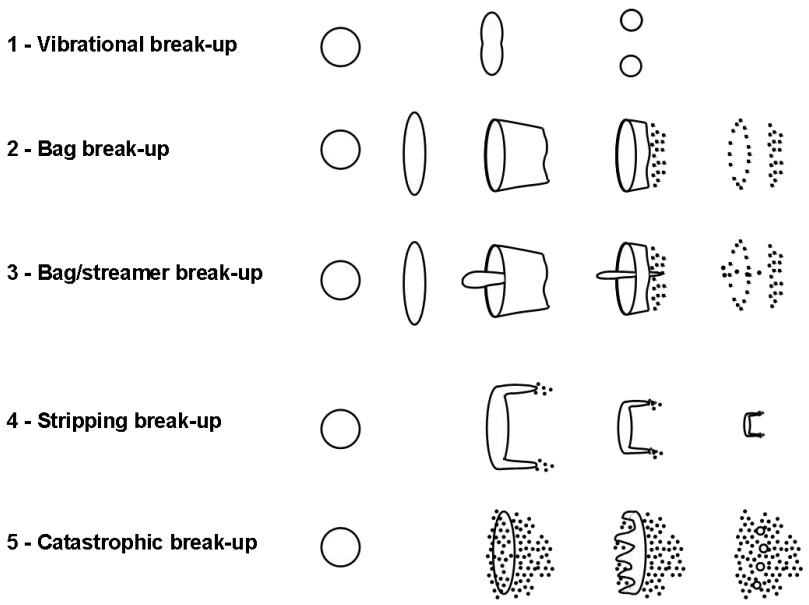

The relative velocity between the liquid and gas phase interface induces aerodynamic forces that create oscillations in the droplet surface. The growing of the amplitude of these oscillations results in droplet break-up. The gas phase Weber number $We_g = u^2_{rel} D\rho_g/\zeta$ is the relevant parameter for the mechanism of liquid drop break-up. That number is a relation between the aerodynamic force, which tends to break up the droplets into smaller particles and the surface tension force, which on the other hand tries to keep the parent droplets in their spherical shape. As the droplets become smaller, the surface tension necessary to break it up becomes bigger and therefore the relative velocity must also be bigger to disintegrate the drop.

Experimental investigations show that the distinct break-up regimes can be divided according to a range of Weber numbers. The table 6 presents the transition Weber numbers for different break-up regimes.

Table 6 – Transition Weber numbers for different regimes (BAUMGARTEN, 2005)

Wierzba	*Weber number*	*Arcoumanis et al.*	*Weber number*
1. Vibrational	≈ 12	1. Vibrational	≈ 12
2. Bag	< 20	2. Bag	< 18
3. Bag-streamer	< 50	3. Bag-streamer	< 45
4. Stripping	< 100	4. Chaotic break-up	< 100
5. Catastrophic	> 100	5. Sheet stripping	< 350
		6. Wave crest stripping	< 1000
		7. Catastrophic	> 1000

Regarding the numerical simulation of secondary break-up processes, several models have been proposed in the literature. The Reitz-Diwakar model was chosen in this work and it is going to be described in subsection 5.2.2.

5.1.3 Full-cone sprays

The figure 38 shows a schematic representation of a full-cone spray, which is the object of study of the second part of the current work. In passenger cars, the injection hole may be smaller than 1 mm and the injection pressure can vary from 100-200 bar in port-fuel injection gasoline engines until more than 1000 bar in diesel engines.

The flow inside the injector is controlled by a needle that may be mechanically coupled to the crankshaft by the operation of a spring, pushing the tip away from the injector opening seat when the fuel is to be injected. The open and close control may also be made by electrical commands with varying injection timing in modern technologies like the HCCI engines.

Figure 38 – Schematic representation of a full-cone spray

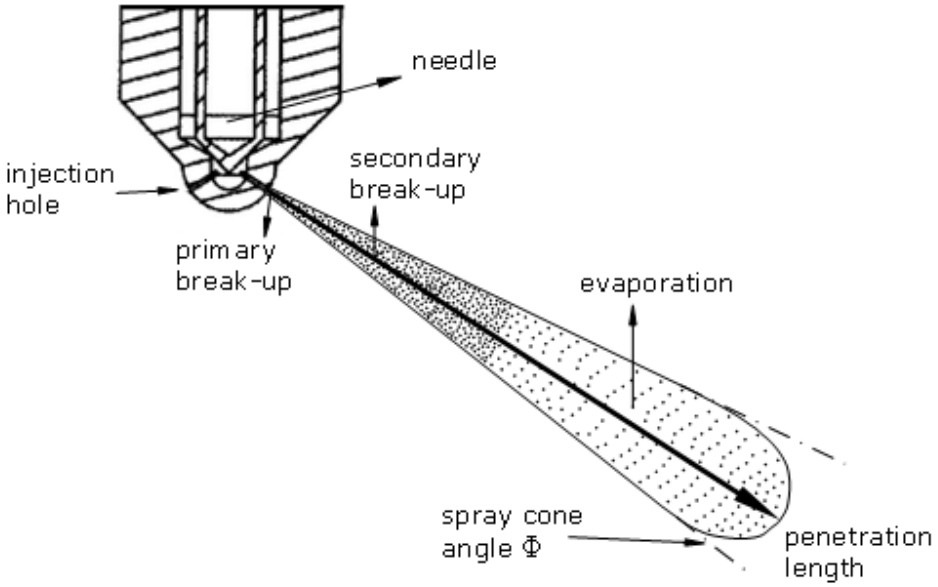

The primary break-up happens just after the injection hole exit and the first droplets formed are subject of secondary break-up further downstream in the spray jet. The spray cloud forms a spray cone angle Φ, which must be given as input parameter in numerical models, so that random distribution functions can spread the injected particles in the range of the spray cone. As the fuel travels further into the gaseous medium, it changes heat with the gas phase, evaporates and mixes with the combustion chamber charge.

In the study of fuel sprays, it is important to define some properties to describe its behavior accurately. One of these properties is the spray penetration length, which can be defined as the distance from the injection hole until the spray tip. Distinct expressions have been proposed by different authors in the literature as Hiroyasu and Arai (1990) and Dent (1971). The following equation (31) is the penetration length of a spray injected in a hot combustion chamber as proposed by Dent:

$$S = 3.07\left(\frac{\Delta p}{\rho_g}\right)^{0.25}(tD)^{0.5}\left(\frac{294}{T_g}\right)^{0.25} \quad (31)$$

in which Δp is the difference between the injection pressure and the combustion chamber pressure, ρ_g is the density of the gas phase, t is the time in seconds, D is the nozzle hole diameter and T_g is the gas temperature.

Further, Heywood (1988) provides a correlation for the spray cone angle Φ in (32).

$$\tan\left(\frac{\phi}{2}\right) = \frac{4\pi}{3+0.28\left(\frac{L}{D}\right)}\left(\frac{\rho_g}{\rho_l}\right)^{0.5} f(\Upsilon) \tag{32-A}$$

$$f(\Upsilon) = \frac{\sqrt{3}}{6}(1 - \exp(-10\Upsilon)), \qquad \Upsilon = \left(\frac{Re_l}{We_l}\right)^2 \frac{\rho_l}{\rho_g} \tag{32-B}$$

In these equations, ρ_g is the density of the gas phase, ρ_l is the density of the liquid phase, D is the nozzle hole diameter and T_g is the gas temperature. The (L/D) relation is a parameter related to the nozzle geometry, Re_l is the Reynolds number of the liquid droplets and We_l the liquid Weber number.

As long the particles are being broken during the spray injection, the spray droplets present a non uniform distribution of diameters and thus the calculation of an average of the particle size is relevant. For this, the sauter mean diameter (SMD or d_{32}) in equation (33) is employed, defined as the diameter of a model sphere that has the same volume/surface area ratio to the sum of all droplet volumes divided by the sum of all droplet surface areas in the spray cloud.

$$\frac{V_m}{A_m} = \frac{\sum_{i=1}^{n} \frac{4}{3}\pi\left(d_p/2\right)^3}{\sum_{i=1}^{n} 4\pi\left(d_p/2\right)^2} = \frac{\sum_{i=1}^{n}\left(d_p/2\right)^3}{\sum_{i=1}^{n} 3\left(d_p/2\right)^2} = \frac{d_{32}}{6} \tag{33-A}$$

$$d_{32} = 6\frac{V_m}{A_m} \tag{33-B}$$

V_m and A_m are the volume and surface area of the model sphere respectively, while d_p is the diameter of each droplet and d_{32} the sauter mean diameter.

This subsection summarized some of the most important aspects for the modeling of fuel sprays. Next, the numerical solver for spray simulations will be presented.

5.2 Numerical solver

The solver used for the spray simulations is the so called sprayFoam, which is also based on the PIMPLE algorithm described in the section 4.3 for the solution of the discretised governing equations. Differences here are the addition of Lagrangian particle tracking (LPT) for the description of fuel droplets being injected in a continuum medium and an additional transport equation for the solution of the mass fraction of the different species involved. The

solver is also capable of simulating the combustion process of the gas phase after the evaporation of the injected drops.

In order to account for the presence of the Lagrangian particles, source terms must be added to the governing equations.

The filtered governing equations read for the balance of mass in equation (34), the balance of momentum in equation (35) and the balance of total energy in equation (36):

$$\frac{\partial \bar{\rho}}{\partial t} + \frac{\partial(\bar{\rho}\tilde{u}_j)}{\partial x_j} = S_\rho \tag{34}$$

$$\frac{\partial}{\partial t}(\bar{\rho}\tilde{u}_i) + \frac{\partial}{\partial x_j}(\bar{\rho}\tilde{u}_i\tilde{u}_j) = \frac{\partial}{\partial x_j}\left[\bar{\rho}\bar{\nu}\left(\frac{\partial \tilde{u}_j}{\partial x_i} + \frac{\partial \tilde{u}_i}{\partial x_j}\right) - \frac{2}{3}\bar{\rho}\bar{\nu}\frac{\partial \tilde{u}_k}{\partial x_k}\delta_{ij} - \bar{\rho}\tau_{ij}^{sgs}\right] - \frac{\partial \bar{p}}{\partial x_i} + \bar{\rho}g_i + S_u \tag{35}$$

$$\frac{\partial}{\partial t}(\bar{\rho}\tilde{h}) + \frac{\partial}{\partial x_j}(\bar{\rho}\tilde{h}\tilde{u}_j) + \frac{\partial}{\partial t}(\bar{\rho}\tilde{K}) + \frac{\partial}{\partial x_j}(\bar{\rho}\tilde{K}\tilde{u}_j) = \frac{\partial}{\partial x_j}\left(\alpha_{eff}\frac{\partial \tilde{h}}{\partial x_j}\right) + \frac{\partial \bar{p}}{\partial t} + S_h \tag{36}$$

As mentioned, an additional transport equation of mass fraction for the species involved must also be added, as equation (37) denotes:

$$\frac{\partial}{\partial t}(\bar{\rho}\tilde{Y}_i) + \frac{\partial}{\partial x_j}(\bar{\rho}\tilde{Y}_i\tilde{u}_j) = \frac{\partial}{\partial x_j}\left(\mu_{eff}\frac{\partial \tilde{h}}{\partial x_j}\right) + S_{Yi} \tag{37}$$

In order to reduce the computational effort, in this work the parcel approach will be used. A spray is composed of a large number of particles of different diameters and handling each one of them would be very expensive computationally. To avoid it, one can define a parcel as a group of droplets with the same properties, reducing a lot the number of particles to be treated. Another reasonable assumption is to consider that all parcels are perfectly spherical, having a diameter d. These assumptions enable the handling of a big amount of particles and their related phenomena with reasonable computational resources.

The Navier-Stokes equations in (34), (35) and (36) are exactly the same equations defined in chapter 3, with the difference that the changes in density, momentum and energy due to the interaction with parcels are addressed by the addition of the source terms S_ρ, S_u and S_h, respectively.

The additional transport equation for Y_i in (37) owns also a source term S_{Yi}, so that the mass fraction of each species can be updated as long the parcels are being evaporated.

Now, with respect to the size distribution of the injected droplets, the cumulative probability density function (CDF) Rosin-Rammer as shown in equation (38) will be employed:

$$F(x,n,d) = 1 - e^{-(x/d)^n} \tag{38}$$

In the simulations performed in this work, it was assumed n = 3 and the maximum and minimum droplet diameters were defined as 1.5E-4 m and 1E-6 m, respectively.

The sprayFoam solver owns different models to describe spray injectors. In each of them, there are different manners of specifying the characteristics of the injection based on properties like pressure, mass flow rate, number of injection holes, number of parcels, etc. The injection model used here is called *ConeNozzleInjection* and its properties are defined hereafter.

The velocity of the injected parcels can be defined in two particular types, with the pressure driven velocity or by specifying a mass flow rate and a discharge coefficient C_{dis}. When the pressure driven velocity type is used, the Bernoulli equations are used to derive the velocity of the injected particles, as presented in equation (39):

$$U_{inj} = \sqrt{\frac{2\Delta p_{inj}}{\rho_l}} \tag{39}$$

in which Δp_{inj} is the difference between the sac hole and combustion chamber pressures and ρ_l is the density of the injected parcel. However, the Bernoulli equation does not consider the friction and this value may be over estimated.

Another way of specifying the velocity is providing the mass flow rate and the discharge coefficient of the injection hole, as in equation (40):

$$U_{inj} = \frac{\dot{m}}{\rho C_{dis} A} \tag{40}$$

in which $\dot{m}$ is mass flow rate profile, ρ is the fluid density, A is the hole cross section and C_{dis} is the discharge coefficient. The discharge coefficient is defined as the ratio of actual and theoretical discharge delivered by a nozzle.

Finally, for a complete description of the spray cone, one has also to define the direction of the injected velocity for each parcel, so that the parcels are injected over a specified allowed range. For this, the expression in equation (41) is used.

Figure 39 illustrates the injection of a full cone spray, showing the maximum allowed angle.

Figure 39 – Full-cone spray (adapted from http://www.wired.co.uk)

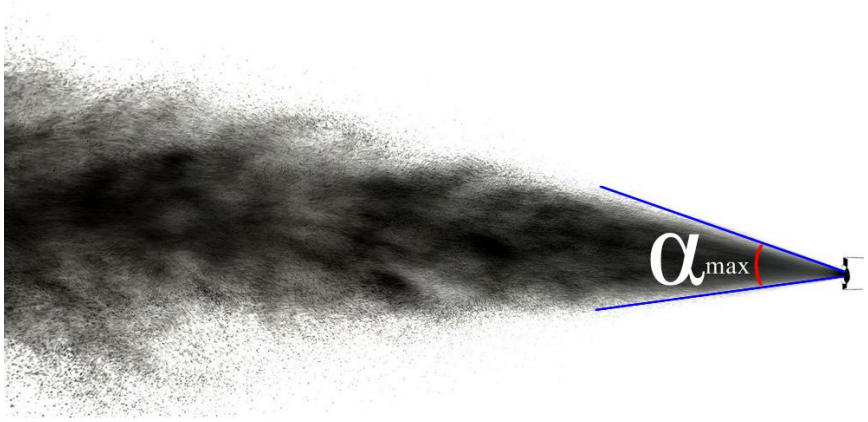

$$\alpha = \frac{d - d_{max}}{d_{min} - d_{max}} \alpha_{max} \tag{41}$$

in which α_{max} is the maximum injection angle allowed, d_{max} is the maximum parcel diameter and d_{min} is the minimum parcel diameter. Thus, the smaller parcels are injected within an angle, while the larger ones go straight.

5.2.1 Momentum and energy equations

As liquid fuel droplets are injected into a domain containing a fluid in the gas phase, these particles are subject of drag forces acting at the liquid-gas interface present at the droplet surface. The drag forces refer to forces acting against the movement of a body, which has a relative motion with respect to a surrounding fluid. This body can be either a solid object or, in the case of sprays, it may be a liquid sphere moving around a gas ambient. The line of action of the drag force (F_D) is parallel to the movement of the droplet and its strength depends on the droplet velocity (V) and diameter (d), as well the viscosity (μ) and density (ρ) of the surrounding gas.

As demonstrated by Fox and McDonald (1998), the Buckingham's theorem can be applied to derive the drag force from its dimensionless parameters, as equation (42) shows:

$$\frac{F_D}{\rho V^2 d^2} = f_1\left(\frac{\rho V d}{\mu}\right) \tag{42}$$

The droplet diameter square (d^2) is proportional to the cross section ($A = \pi d^2/4$) and, thus, equation (43) can be rewritten as:

$$\frac{F_D}{\rho V^2 A} = f_2\left(\frac{\rho V d}{\mu}\right) = f_2(Re) \tag{43}$$

Although equation (43) was written for a spherical droplet, it is valid for any shape. From this, one can then derive the drag coefficient (C_D) in equation (44), which is a dimensionless number to account for the drag or resistance suffered from an object in a fluid environment.

$$C_D = \frac{F_D}{\frac{1}{2}\rho V^2 A} \tag{44}$$

When liquid fuel parcels are injected at high velocities in a quiescent gas environment, they tend to be decelerated by the gaseous surroundings, as the gas tends to be accelerated by the parcels. This resulting exchange of momentum between the liquid and gas phase takes place due to the relative velocity between them. The equation (45), as shown by Vuorinen et al. (2011), denotes this exchange of momentum by evaluating the resulting drag force over a liquid parcel moving with relative velocity u_{res} with respect to the gas phase.

$$\frac{1}{6}\rho_P \pi d^3 \frac{du_P}{dt} = \frac{1}{2}\left(u_g - u_P\right)\left|u_g - u_P\right|\rho_g C_D \frac{\pi d^2}{4} \tag{45}$$

The term on the left side represents the change on the acceleration of the liquid fuel parcel, while the term on the right side denotes the drag force due to its relative motion to the gas phase. The subscript "g" refers to the gas phase and "P" to the liquid parcel of diameter d.

The drag coefficient C_D is calculated assuming spherical parcels and is calculated using the Reynolds number of the gas phase $Re_g = du_{rel}\rho_g/\mu_g$. The correlation for evaluating C_D is presented in equation (46).

$$C_{D,sphere} \begin{cases} \frac{24}{Re_g}\left(1 + \frac{1}{6}Re_g^{\frac{2}{3}}\right) & Re \leq 1000 \\ 0.424 & Re > 1000 \end{cases} \quad (46)$$

Finally, the parcels can be tracked by updating their positions according to equation (47).

$$\frac{dx_P}{dt} = u_P \quad (47)$$

As soon as the liquid parcels get into the domain, besides exchanging momentum, they also exchange heat with the gas phase. The liquid phase exchanges heat with the gas due to diffusive and convective transport and radiation. Increasing the heat, the temperature is also increased until the parcel reaches the boiling temperature and hence evaporates. This is very important for the mixing process, combustion and formation of pollutants since the fuel starts to burn only when it is in the vapor phase. So if one aspires to predict the combined phenomena of direct injection and combustion in internal combustion engines, it is of fundamental importance to describe the evaporation process in a correct manner.

For this, in addition to the assumption of perfect spherical parcels, one may also neglect the effect of radiation, since it is small compared to convection. Further, the evaporation modeling is based on the averaged flow field around the parcels, because the flow among them is not feasible to be calculated. For simplicity, other phenomena as break-up and collisions may be neglected for the calculation of the evaporation process. These assumptions off course have an effect on the solution, but they are quite reasonable since the significant reduction in complexity and computational effort achieved, as well due to the fact, that evaporation models have already showed good agreement with experiments before.

Real fuels are composed of a variety of different components, which impact the evaporation process in different ways. Components with higher molecular weight take more time than lighter components. However, again in order to simplify the models, the standard framework on fuel-spray modeling today usually assumes n-heptane to represent the properties of diesel and iso-octane for the properties of gasoline.

Baumgarten (2006) obtains the following energy balance for a liquid parcel, presented in equation (48):

$$m_P c_{p,l} \frac{dT_P}{dt} + \Delta h_{evap} \frac{dm_{evap}}{dt} = \lambda_g \pi d_P (T_\infty - T_P) \frac{\varsigma}{e^{\varsigma}-1} Nu \quad (48)$$

The terms Nu and ς are shown in equations (49) and (50), respectively.

$$Nu = \frac{\alpha . d_P}{\lambda_g} \quad (49)$$

$$\varsigma = \frac{\dot{m}_{evap}\, c_{p,vap}}{Nu\, \lambda_g \pi d_P} \quad (50)$$

In equation (48), the first term represents the energy necessary to heat up the liquid fuel parcel until a given temperature in an interval dt, where m_p is the mass of the parcel, T_P its temperature and $c_{p,l}$ the specific heat at constant pressure of the liquid fuel. The second term accounts to the energy necessary to evaporate the parcel mass m_{evp} during the interval dt.

The only term on the right side accounts to the heat transfer between the liquid and gas phase. Where T_∞ is the temperature of the gas phase and T_P is the temperature of the parcel. The d_P is the parcel diameter, λ_g is the thermal diffusivity of the gas mixture, Nu is the Nusselt number and ς is a dimensionless correction factor accounting of the reduced heat transfer due to the simultaneous mass transfer from the parcel to the gas phase. Equation (50) shows how ς is evaluated.

The appropriate Nusselt number to consider the effect of the relative velocity between parcel and gas was proposed by Ranz and Marshall (1952) and reads in equation (51):

$$Nu = 2.0 + 0.6 Re^{1/2} Pr^{1/3} \quad (51)$$

in which the Reynolds and Prandtl numbers are calculated as follows in (52) and (53):

$$Re = \rho_\infty u_{rel} d_P / \mu_g \quad (52)$$

$$Pr = \mu_g c_p / \lambda_g \quad (53)$$

This subsection presented the most relevant information regarding the modeling of the conservation of energy and momentum in fuel-sprays. Next, the breakup model used in the present work will be presented.

5.2.2 Breakup model

The breakup model used in the present work is the ReitzDiwakar model, which is going to be addressed in this subsection.

Figure 40 – Schematic representation of the blob-method

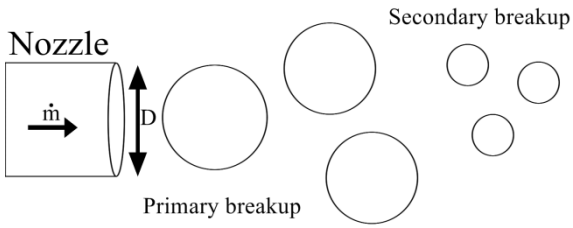

The model was developed by Reitz and Diwakar (1987) and works according to two assumptions. First, atomization and drop breakup near the nozzle within the spray cloud are considered to be indistinguishable processes. Thus, the blob method is used to represent the jet breakup into the first spray droplets. By using this method, a detailed simulation of the phenomena near the nozzle is replaced by the injection of big spherical droplets, which have uniform diameter similar to the nozzle hole size. The velocity of these first droplets is determined by the previously presented equations (39) or (40) and the direction by the equation (41). Figure 40 illustrates how the blob-method works. The injected big droplets are then subject of secondary breakup as they travel into the gaseous medium.

The second assumption is related to the secondary breakup. The ReitzDiwakar model distinguishes between only two droplet breakup regimes: the bag breakup and the stripping breakup. These regimes are illustrated in figure 41.

Figure 41 – Breakup regimes of the ReitzDiwakar model

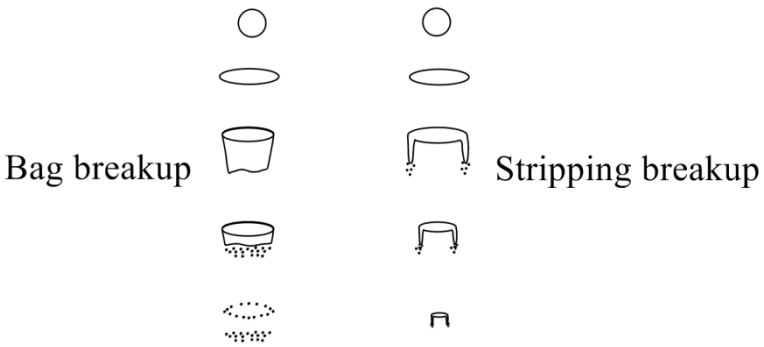

Bag breakup occurs if We_P (Weber number of a liquid parcel) is greater than a certain critical value. Equation (54) shows how We_P is calculated, where ρ_l and D_P are the density and diameter of the liquid parcel, u_{rel} is the relative velocity to the gas phase and ζ is the surface tension. In this breakup regime, the parent particle is firstly stretched perpendicularly to its direction until a given size. After this, aero dynamical forces start acting over the droplet surface parallel to its direction. Since the surface tension acts against these forces in order to avoid breakup, the particle takes the form of a bag with a very thin surface. As the particle continues its movement, the surface tension becomes too weak to support the strength of the aero dynamical forces and the particle breaks up into several product droplets, with much smaller diameter.

$$We_P = \frac{\rho_l u_{rel}^2 D_P}{\sigma} \tag{54}$$

Independent on the breakup regime, the reduction of particle radius is described by the following relation in equation (55):

$$\frac{dr_P}{dt} = \frac{-(r_P - r_{stable})}{t_{br}} \tag{55}$$

in which r_p is the particle radius, r_{stable} the new stable radius of the particle after breakup and t_{br} is the characteristic breakup time. The parameters r_{stable} and t_{br} are calculated according to the breakup regime, as it will be presented below.

Increasing We_P, the stripping breakup may occur. In this regime, the parent droplet is also firstly stretched to a given size. Then, due to the high aero dynamical forces acting over the droplet surface, product droplets of very small diameters are stripped from the parent one. The size of the parent particle is then continuously reduced until at the end only smaller particles are present.

The criteria for occurring bag breakup and stripping breakup are presented in table 7.

Table 7 – Criteria for occurring bag breakup and stripping breakup

Bag breakup ($We_P > We_{crit}$)	
Characteristic breakup time	$t_{br} = C_1\sqrt{\frac{\rho_P r_P^3}{2\sigma}}$
New stable radius	$r_{stable} = \frac{6\sigma}{\rho_g u_{rel}^2}$
Stripping breakup ($We_P/\sqrt{Re} > C_{s1}$)	
Characteristic breakup time	$t_{br} = C_2\frac{r}{u_{rel}}\sqrt{\frac{\rho_P}{\rho_g}}$
New stable radius	$r_{stable} = \frac{\sigma^2}{2\,\rho_g^2 u_{rel}^3 \nu}$

The parameters C_1, C_2, We_{crit} and C_{s1} are model constants and their values and definitions are introduced in table 8.

Table 8 – ReitzDiwakar model constants

Constant	*Value*	*Definition*
C_1	0.785	Time factor for bag breakup
C_2	10	Time factor for stripping
We_{crit}	6	Critical Weber number for bag
C_{s1}	0.5	Weber number factor for stripping

5.3 Test-case: ECN "Spray G"

In order to validate the fuel spray model presented above, a test-case from the engine combustion network (ECN) was chosen. The ECN is an international network of researchers from different institutions, who perform experiments and modeling on the field of engine combustion. Among its objectives are providing valuable experimental data of fuel-spray injection and combustion of different test-cases for validation. Furthermore, the results obtained from computational models and the data used for their validation, can be compared, discussed and improved in open forums organized by the network, thus identifying priorities for future experimental and modeling works. All this information is well-documented and

based in internet libraries maintained by the Engine Combustion Department of Sandia National Laboratories.

Table 9 – Spray G operating conditions of ECN

Fuel	Iso-octane
Injection pressure	20 MPa
Fuel temperature	90 ºC (363 K)
Ambient temperature	300 ºC (573 K)
Ambient density	3.5 kg/m^3
Ambient pressure	6 bar (600 kPa)
Ambient composition	89.71% N_2, 6.52% CO_2, 3.77% H_2O
Injected quantity	10 mg
Injection duration	780 μs
Number of nozzle holes	8 (equally spaced)
Hole diameter	165 μm
Fully included angle	80º

The test-case chosen in this work is the brand new “Spray G”, which is a multi-hole gasoline spray injection case. This choice is justified because this case is the only one from ECN to use iso-octane as fuel, what is consistent with the first part of the current work where the combustion in an iso-octane fueled optical engine was studied. The operating conditions of the Spray G case are summarized in table 9. The figure 42 illustrates the spray cloud formed during the Spray G injection.

Figure 42 – ECN Spray G gasoline injection case

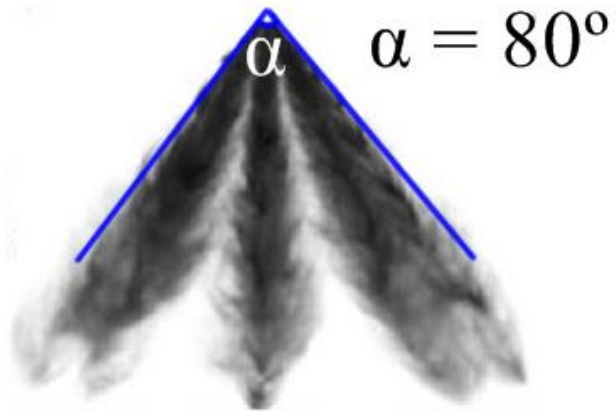

Both experimental and modeling data are available for this test-case, which are going to be used for the validation of the present model. The next subsection will present the numerical setup of the simulations performed here and after this the obtained results will be presented and discussed.

5.4 Numerical setup

Here the case setup of a spray simulation will be presented. Most of information needed for a case setup in OpenFOAM was already addressed in item 4.5 and here only the specifications of the properties regarding the spray injection will be discussed.

As the domain geometry is much less complicated than in the engine case, the *blockMesh* tool is suitable for the grid generation, without the need of a CAD geometry.

The computational domain is a box with dimensions 70 mm in x direction, 70 mm in y direction and 60 mm in z. The grid has equidistant hexahedral cells with a resolution of 0.5 mm, which gives a total of 2.35 million cell elements. Grid dependency studies were also performed for 1 mm and 0.75 mm resolutions. Figure 43 presents the mesh, pointing out the position where the particles are injected into the domain, at the center of the top surface.

Figure 43 – Grid used for spray simulations

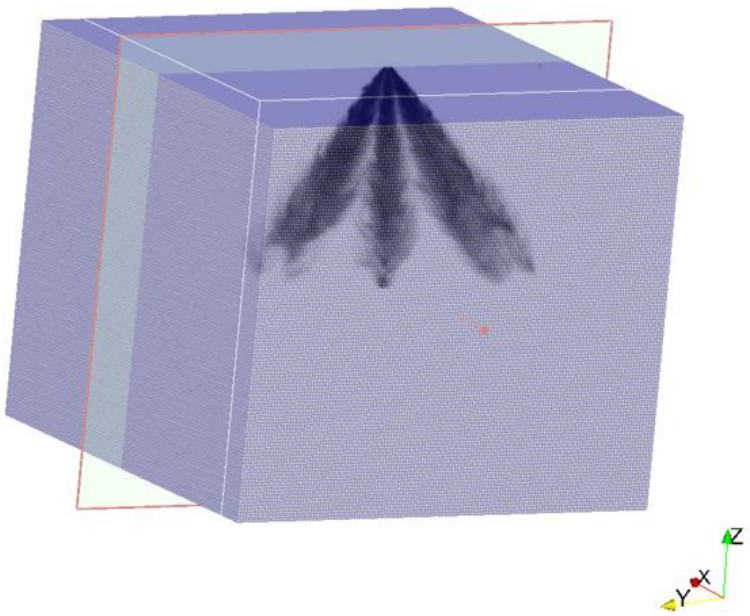

In order to specify the ambient composition required by ECN in this test, volumetric scalar fields for the species N_2, CO_2, and H_2O should be placed at the 0 time folder of the

simulation case, so that the whole domain is initialized with 89.71% N_2, 6.52% CO_2 and 3.77% H_2O by volume. An example of how this is done is shown in frame 8 (appendix) for nitrogen.

In the entry *internalField* a uniform value of 0.8971 for the mass fraction of nitrogen is specified for all the internal cells of the domain. The boundaries are set with zero gradient condition. This should also be done for the other species involved, oxygen and water vapor with their respective values.

In spite of solving the complex chemical kinetics involved in spray-combustion problems, the *sprayFoam* solver uses the CHEMKIN package. Therefore, a folder called *chemkin* has to be placed in the case directory. In the *chemkin* folder are located the files *chem.inp* and *therm.dat*. The first defines the species involved and the reactions mechanisms taking place during the run. As in this work only the phenomena of injection, breakup, evaporation and mixture formation are covered, no reaction mechanism is defined here. The second file defines coefficients for calculating the thermodynamic properties of each species. These two files are shown in frames 9 (appendix) and 10 (appendix) respectively.

The most important dictionary of a spray case is the *sprayCloudProperties*. There are defined all properties with reference to the spray related phenomena, as injected temperature, start and duration of injection, mass flow rate, injection cone angle, heat transfer model, breakup model and so on. Some parts of the *sprayCloudProperties* are sampled in frame 11 (appendix) and 12 (appendix) and explained hereafter.

Frame 11 shows how the injection models are defined. For each nozzle hole one model must be specified. As Spray G owns 8 holes, eight different models are added, named as model1, model2, until model8. The *flowRateAndDischarge* option was chosen for the entry *flowType*. This means that the velocity of the injected parcels will be calculated by a given mass flow rate specified at *flowRateProfileTable*, as given by equation (40). For simplicity, a constant flow rate profile was assumed, so that the total injected mass of each injector is 1.25 mg (1.25 mg times 8 injectors gives the injected mass of 10 mg of table 8). The start of injection is specified to be exactly at the beginning of the run (SOI = 0), duration is assumed to be 0.78 ms and the hole diameter 0.165 mm. Each hole must also have its position and direction specified, so that it forms a fully angle of 80º from equally-spaced sources. Finally, the number of parcels per second must be given. Increasing this number will improve the description of the spray cloud, as so the computational cost will rise. That value should then be adjusted, so that the run has a compromise between good spray description and reasonable computational cost. The value used in the simulations was 20.000.000.

Further, the cone angle formed by each one of the eight spray clouds is defined as 25º, which was obtained from observations from Mie scattering visualizations from experiments. For the droplet diameter distribution, the Rosin-Rammler CDF is here employed.

The Frame 12 (appendix) presents how the models and their constants are specified. As already mentioned, the *RanzMarshall* model is used for the heat transfer and *ReitzDiwakar* for the droplet breakup. The *thermophysicalProperties* is set as shown in Frame 13 (appendix), being important to mention that the address of the files at the chemkin folder must be informed. Besides, the liquid species iso-octane (C8H18) is defined and nitrogen is defined as the inert specie.

To avoid stability problems induced by the high velocities present at the injector nozzle, TVD schemes were used for the solution of the convective terms of the governing equations. The implicit backward scheme was used for the time integration and a relaxation factor of 0.5 was set for the pressure field for a more stable run. Finally, adjustable time step was set to a maximum CFL number of 0.1.

Next, the results obtained from the spray simulations are presented.

5.5 Results and validation

The spray simulation with the setup showed previously takes approximately one day to run using 96 CPUs. In order to show the locations where the results are presented, some figures will be used next. The spray penetration length is calculated as in figure 44.

Figure 44 – Penetration length calculation (adapted from ECN workshop)

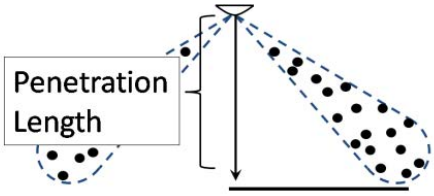

The locations where the iso-octane mixture fraction is taken are shown in figure 45 and figure 46. These locations are defined by members of the ECN network, who are working on the spray G test-case, both with experiments and modeling.

Figure 45 – Profile planes (adapted from ECN workshop)

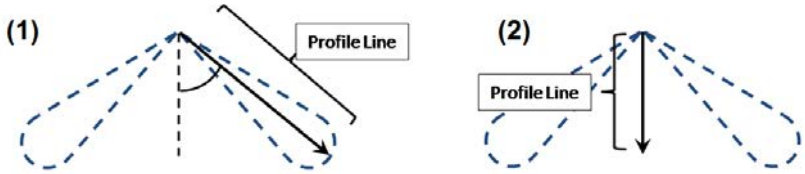

Figure 46 – Cross-section planes (adapted from ECN workshop)

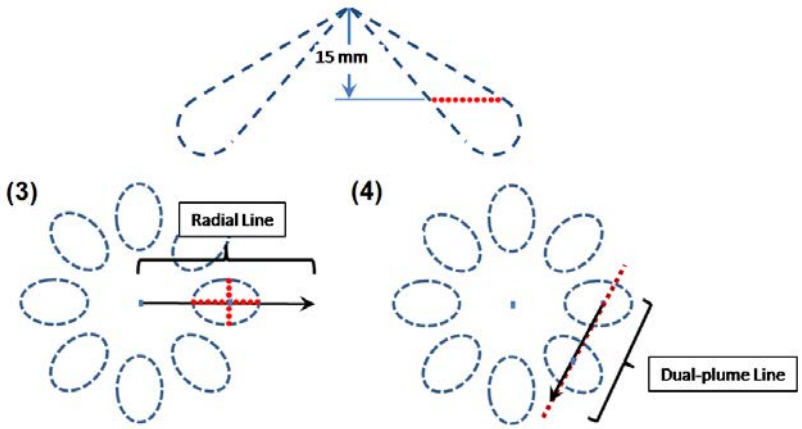

Figure 47 shows the vapour penetration length curve obtained by simulation in comparison with the vapour and liquid penetration length curves obtained by experiments.

Figure 47 – Penetration length (Simulation vs. Experiments)

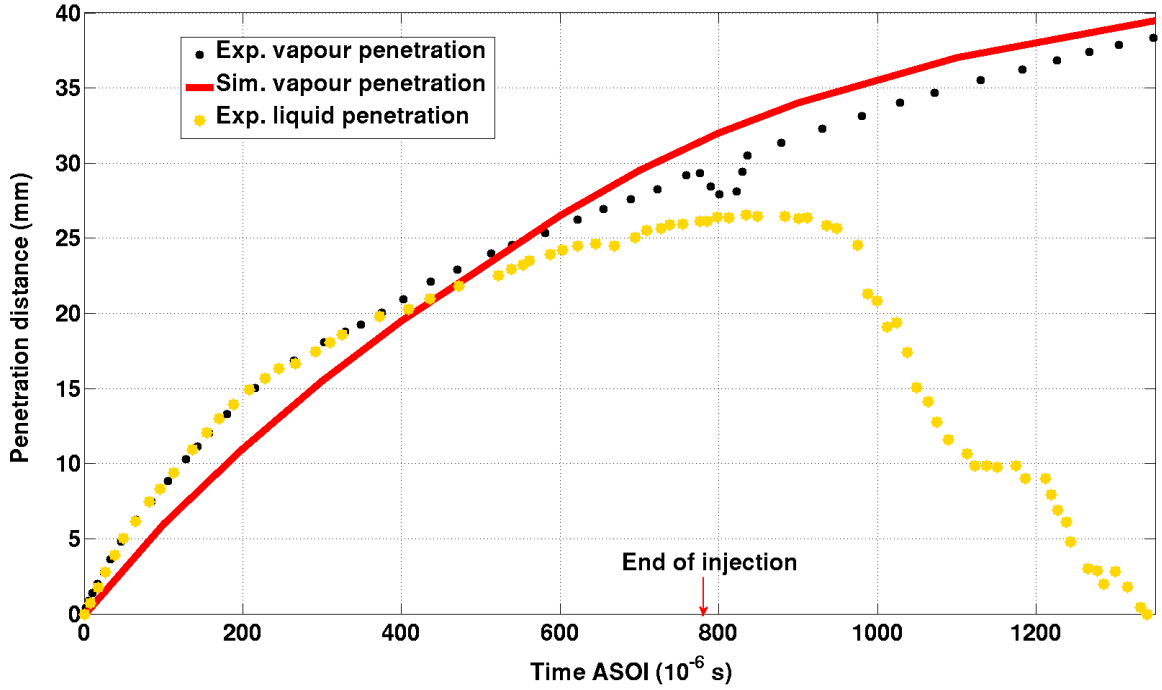

The penetration length curves show that at the beginning the simulation under predicts the experiment. At approximately 500 µs, the vapour penetration length in the simulation hits the experimental value and since then its value is slightly over predicted.

The reason for under prediction at the beginning can be explained by the model assumption of uniform distribution within the spray jet angle of 25º. In reality, this distribution is not uniform and more particles are concentrated in the middle of the jet. This over concentration in the middle makes the jet to flow deeper as in the case with uniform distribution. On the other hand, the over prediction after a certain time can be explained due to the use of a TVD numerical scheme for the solution of the momentum equation. Although it brings the advantage of good stability, the use of TVD schemes with LES can lead to strong dissipation of the present turbulent scales. The presence of only relative large scales observed by flow visualizations is evidence that too much dissipation is taking place. Besides, the mesh grid size of 0.5 mm still may be too coarse to represent the physics of the phenomenon correctly.

Figure 48 shows the spray plumes orientation as defined by the ECN community. The results shown next are taken at the symmetry plane (through jets 1 and 5), which has a transparency of 50% in order to allow the visualization of the jets 2, 3 and 4 as well. A schematic view of the plane location and of the spray orientation is shown in figure 49.

Figure 48 – Spray plume orientation (from ECN Spray G website)

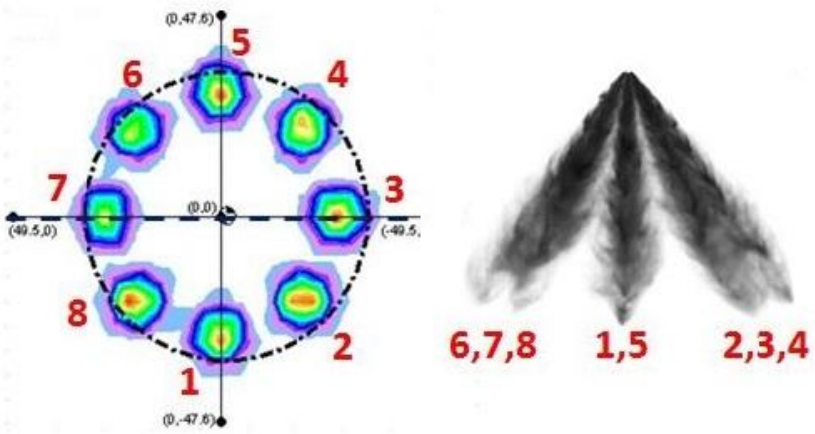

Figure 49 – Schematic view of the observed plane

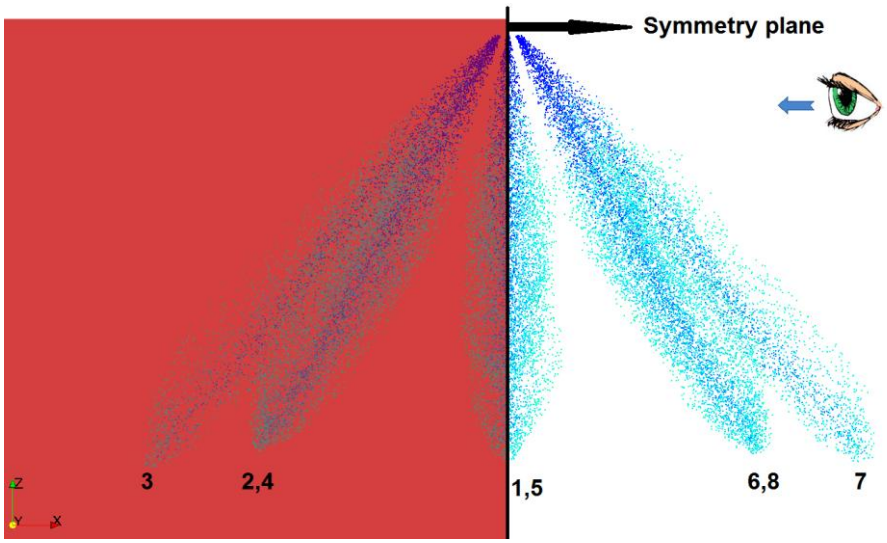

Figure 50 shows the velocity field for magnitude and in axial z direction from 0.002s until 0.012s after the start of injection. Both gas phase and liquid phase are shown, being the liquid droplets represented by Lagrangian particles, which are colored accordingly to their velocities. The injection pressure is 20 MPa, resulting in extreme high fuel droplet velocities just after the injector tip of about 130 m/s. Figure 51 shows mixture fraction of iso-octane in the gas phase and temperature profiles for the same time range, also including the injected parcels in the visualization. The highest mixture fraction values are concentrated close to the jet tip and more susceptible to be in the middle of each spray cloud. Due to the continuous particle breakup process, the droplet diameters become quite small in that regions as long the parcels evolve and thereby in such spots are the droplets more likely to evaporate.

Figure 50 – Velocity field (magnitude and in z direction)

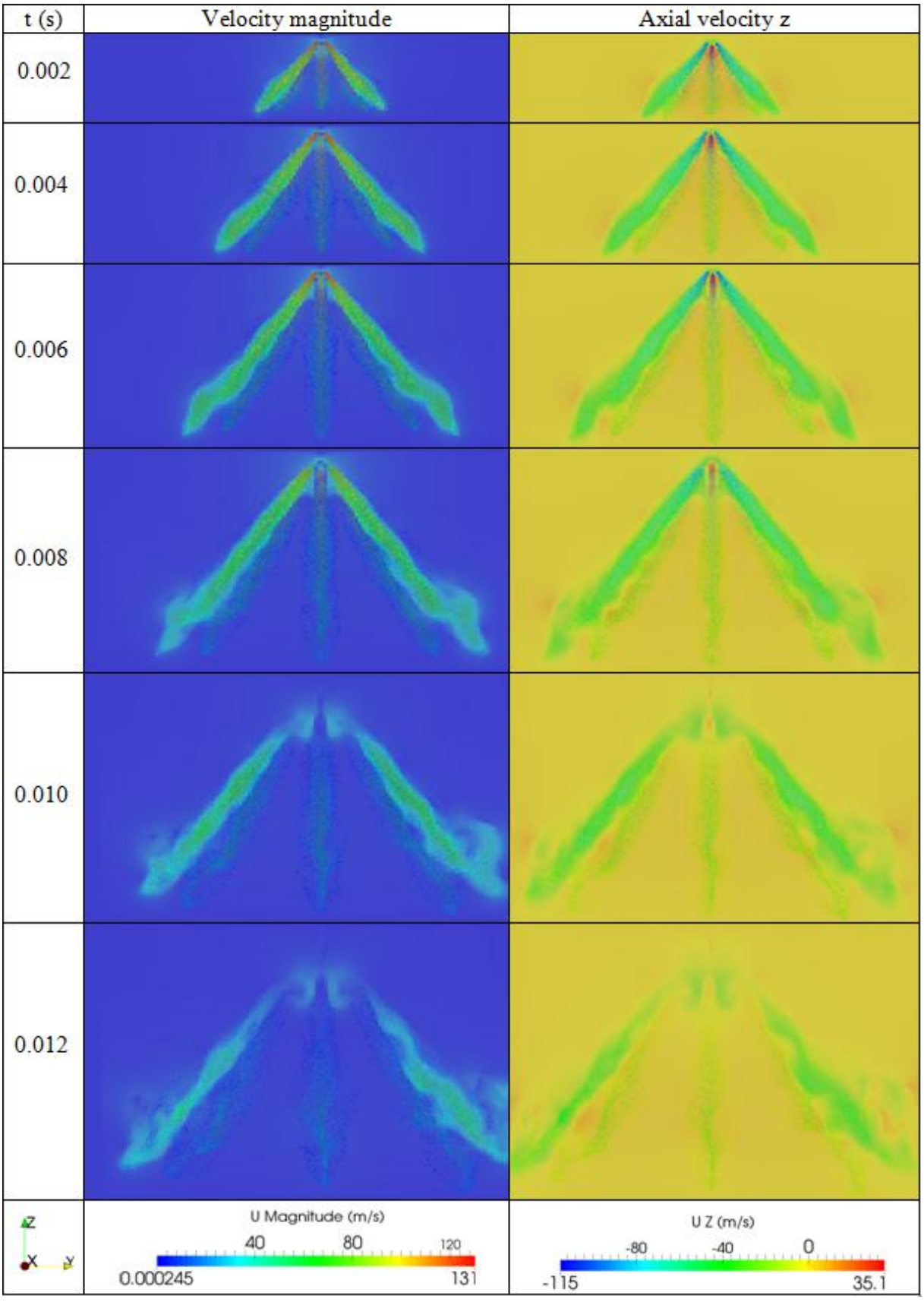

Figure 51 – Mixture fraction and temperature profiles

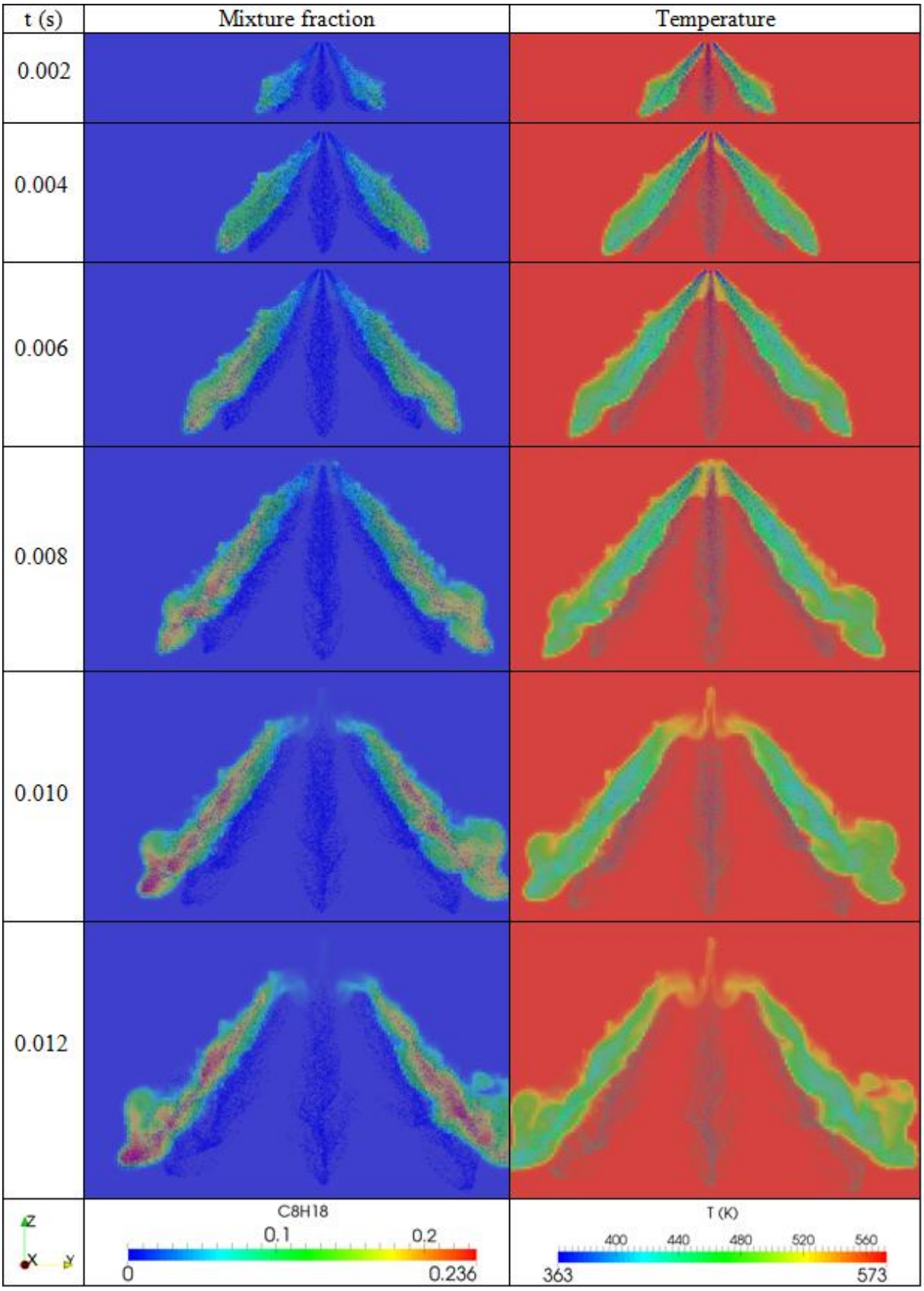

As already explained in previous sections, the present model uses the parcel approach to represent the liquid droplets within the spray. Therefore, since the start of the injection the number of parcels inside the domain increases linearly with the time until the injection end. After this, the number of parcels starts to decrease as long the parcels evaporate. When the number of parcel reaches zero, it means that the entire liquid fuel mass was already transferred to the gas phase. In figure 52, the number of parcels vs. time is plotted.

Figure 52 – Number of injected vs. time

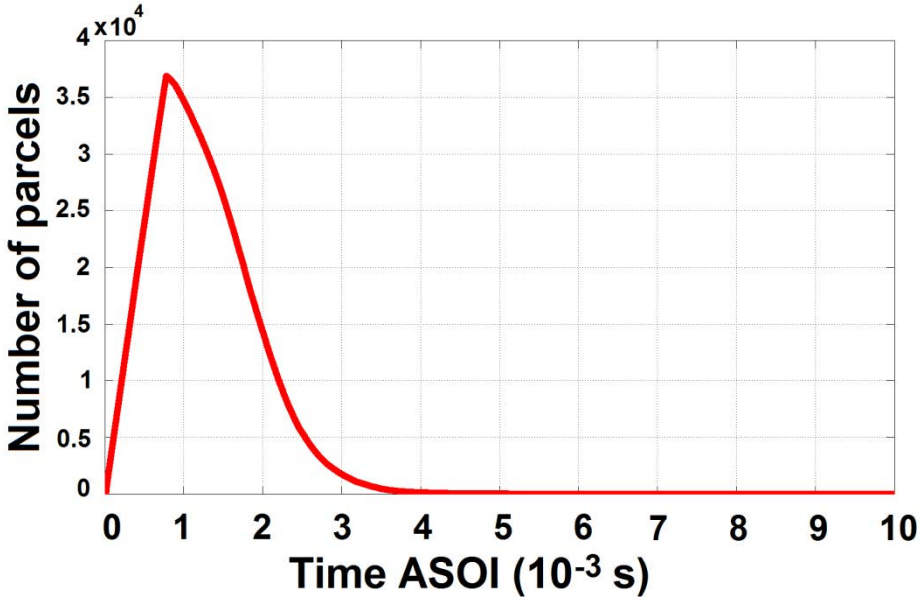

The maximum diameter of the parcels during the injection duration (from 0 until 780 µs) varies around the value of 1e-4 m, which is approximately the value given as maximum diameter to the Rosin-Rammler distribution. In figure 53 the maximum diameter and the Sauter-mean diameter for the parcels are shown. At the injection start, the SMD is about 60 µm, decreasing very fast to something bigger than 20 µm just after the beginning of the simulation. After the injection ending and due to the breakup and evaporation processes, the maximal diameter size decreases abruptly until 45 µm at 900 µs. Since then the parcels continue reducing their diameters within the time until no more parcel, i.e. no more liquid droplet, can be found in the domain.

Figure 53 – SMD and maximum diameter vs. time

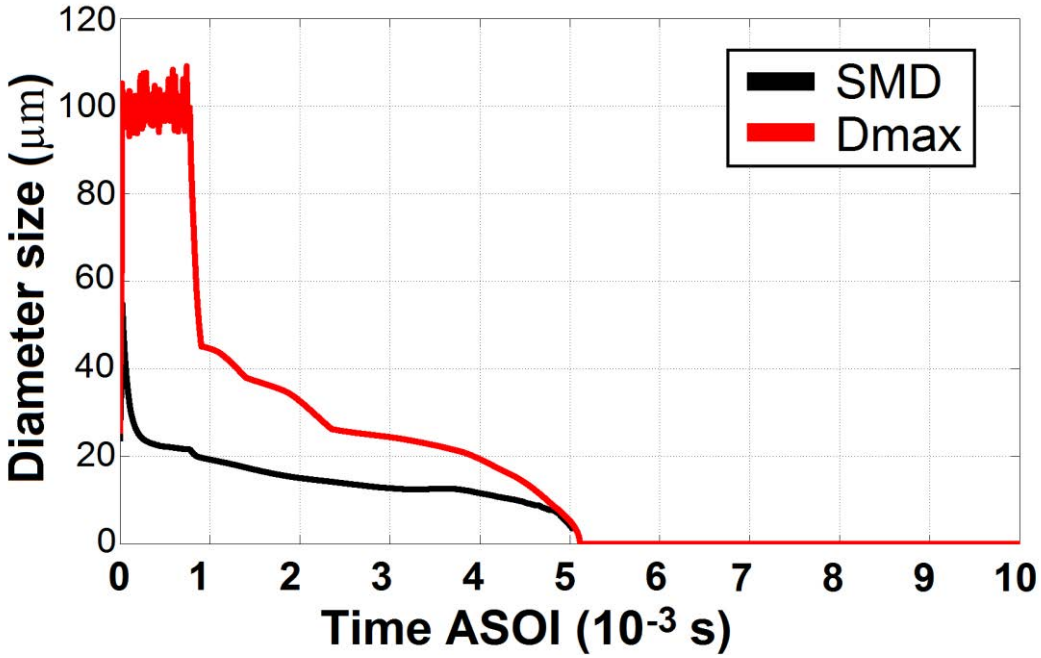

The diameter size distribution of the injected parcels can be visualized in figure 54 (a) and (b), which shows the liquid droplets for the instants 600 µs and 800 µs after start of injection colored accordingly to the diameter. Figure 55 (a) and (b) shows the same at 1000 µs and 1200 µs. The initial diameters have values close to 1e-4 m and as long the jets penetrate further into the gaseous domain, the parcels are subject of bag and stripping breakup and the minimal diameter reaches a very small value of order smaller than 1 µm, making the smallest parcels very likely to evaporate.

Figure 54 – Diameter distribution I

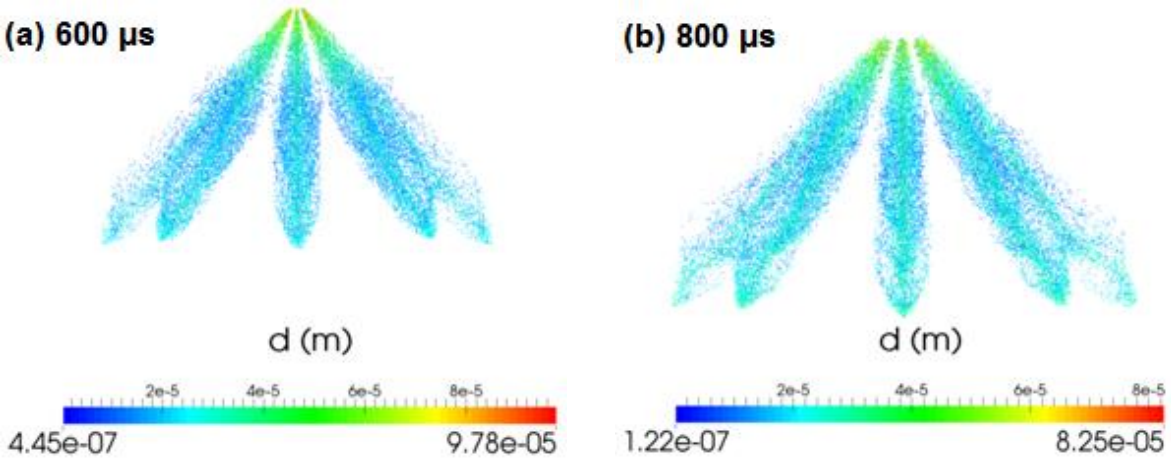

Figure 55 – Diameter distribution II

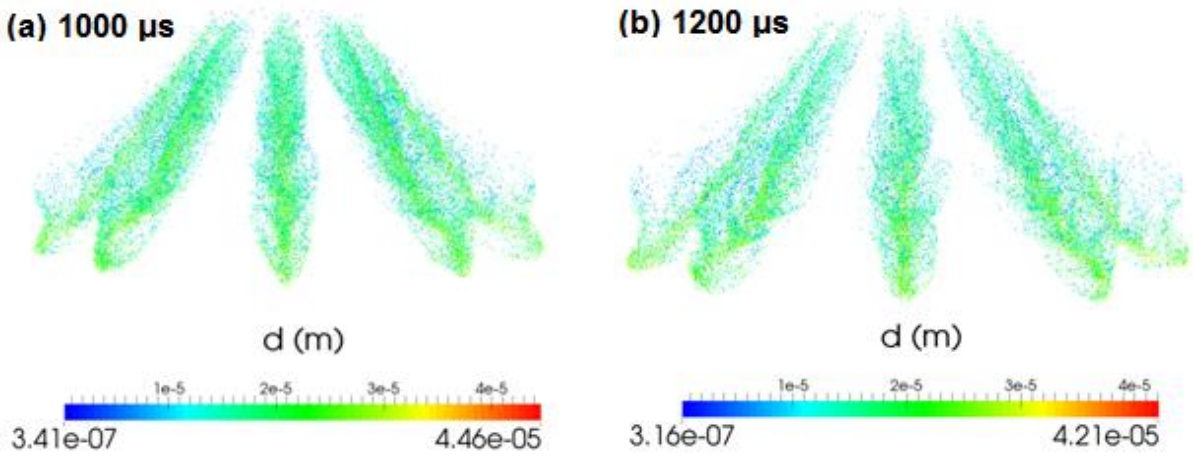

Figure 56 – Velocity vector plot at 400 µs and 800 µs ASOI

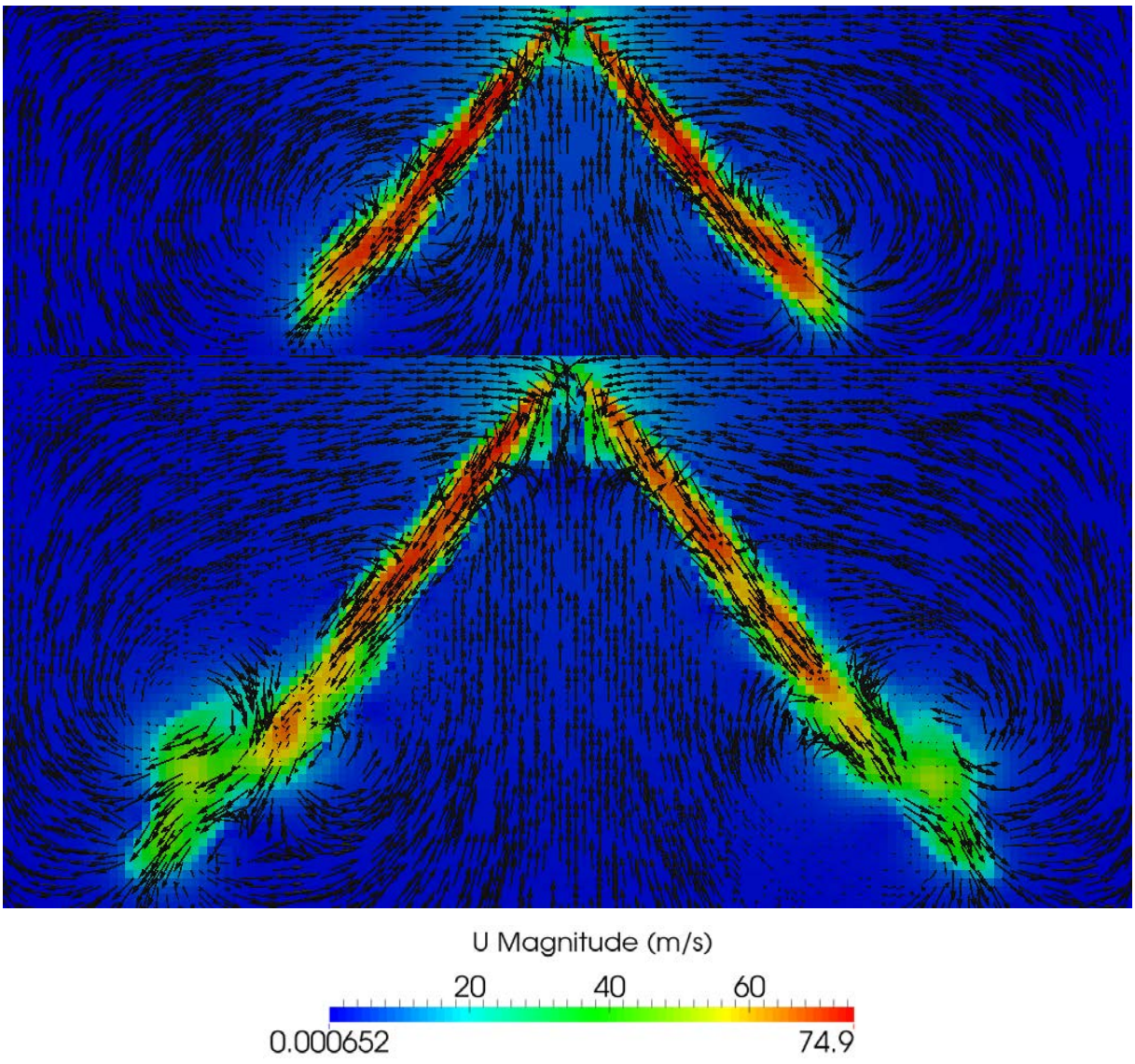

Figure 56 shows the velocity vector plots of the gas phase at 400 µs and 800 µs and figure 57 at 1000 µs and 1400 µs after start of injection. The very high velocity of the injected liquid droplets of more than 100 m/s creates a strong shear layer in the gas medium, which is stationary prior to injection. The parcels then exchange momentum with the gas phase, accelerating it within the spray cone range. This forces the creation of vortices, since the gas outside the spray cloud is weakly influenced by the jet, as one can observe with vector plots at the symmetry plane.

Figure 57 – Velocity vector plot at 1000 µs and 1400 µs ASOI

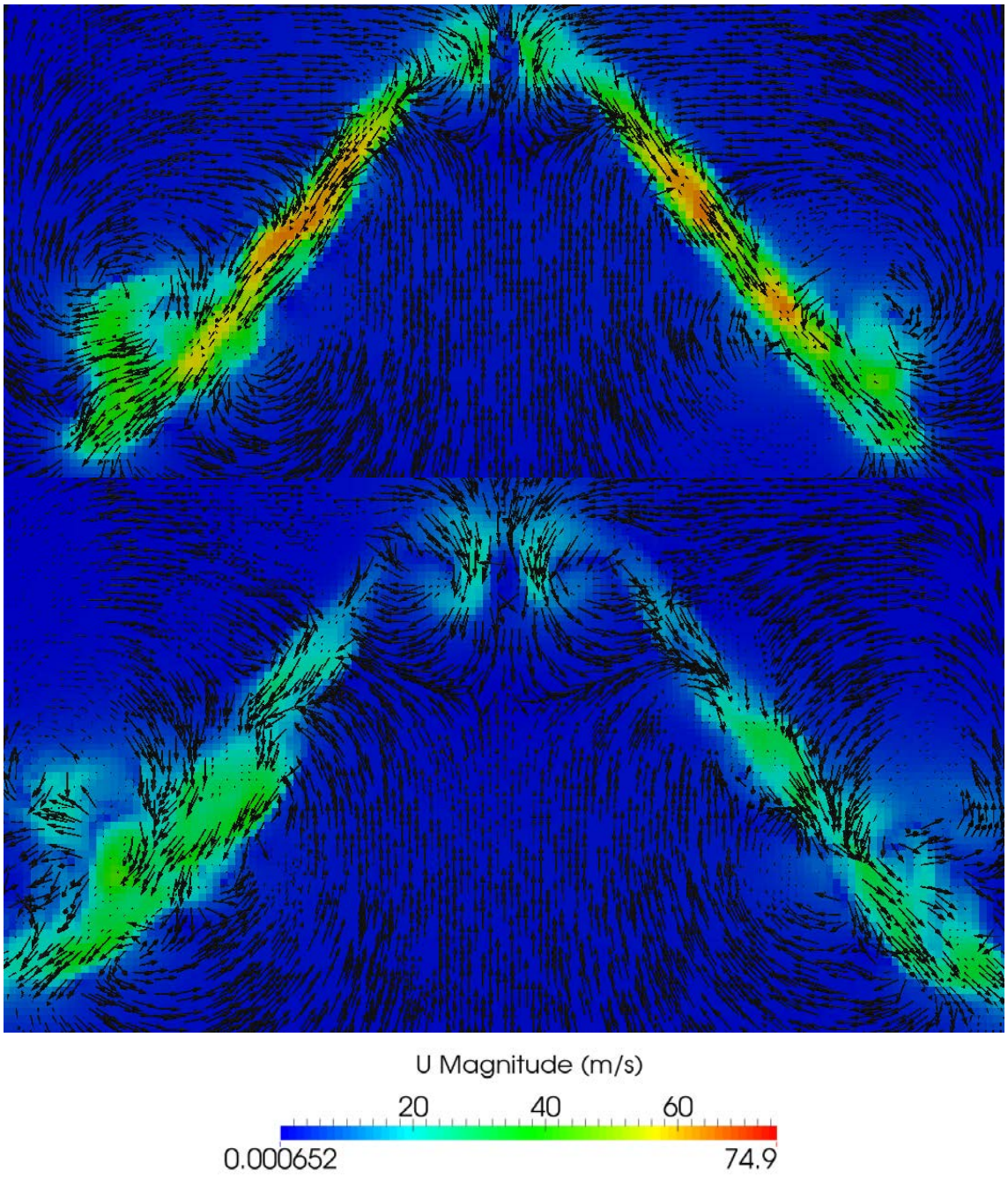

Mixture fraction and temperature of the gaseous phase curves are shown for the previously defined directions for three different instants after start of injection: 0.6 ms, 1.0 ms and 1.4 ms. First, figures 58, 59 and 60 show these results along the jet axis. The initial temperature inside the domain is 573 K and the fuel is injected with a temperature of 363 K. So as long the fuel penetrates further into the domain, the temperature inside it decreases since heat is exchanged between fuel droplets and gas. As seen in the contour plots before, higher iso-octane mixture fraction values are more likely to be found at the spray jet tip.

Figure 58 – Temperature (red) and Iso-octane mixture fraction (black) at 0.6 ms (I)

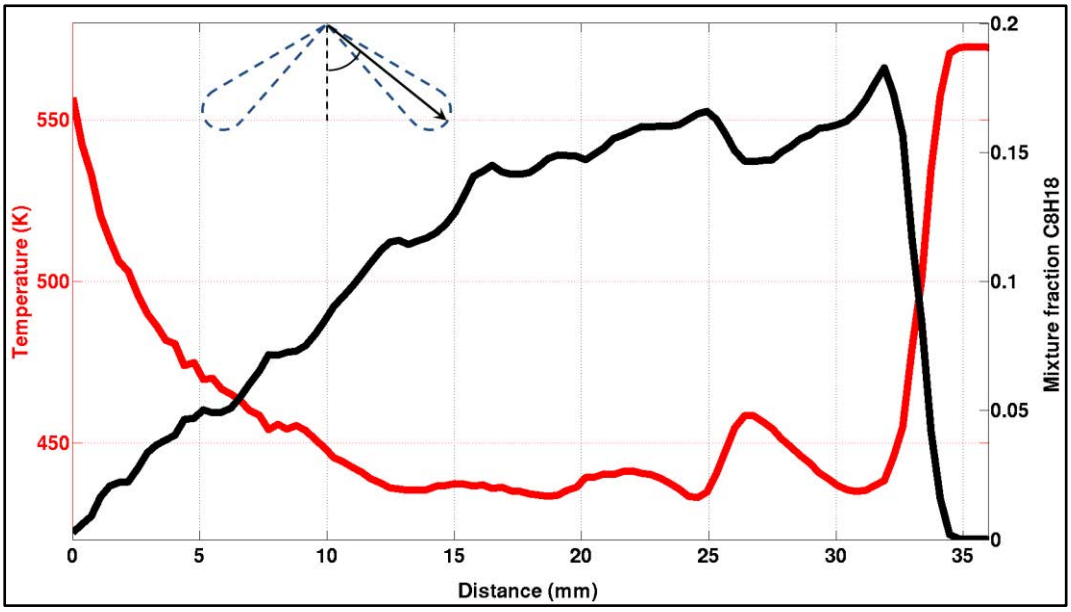

Figure 59 – Temperature (red) and Iso-octane mixture fraction (black) at 1.0 ms (I)

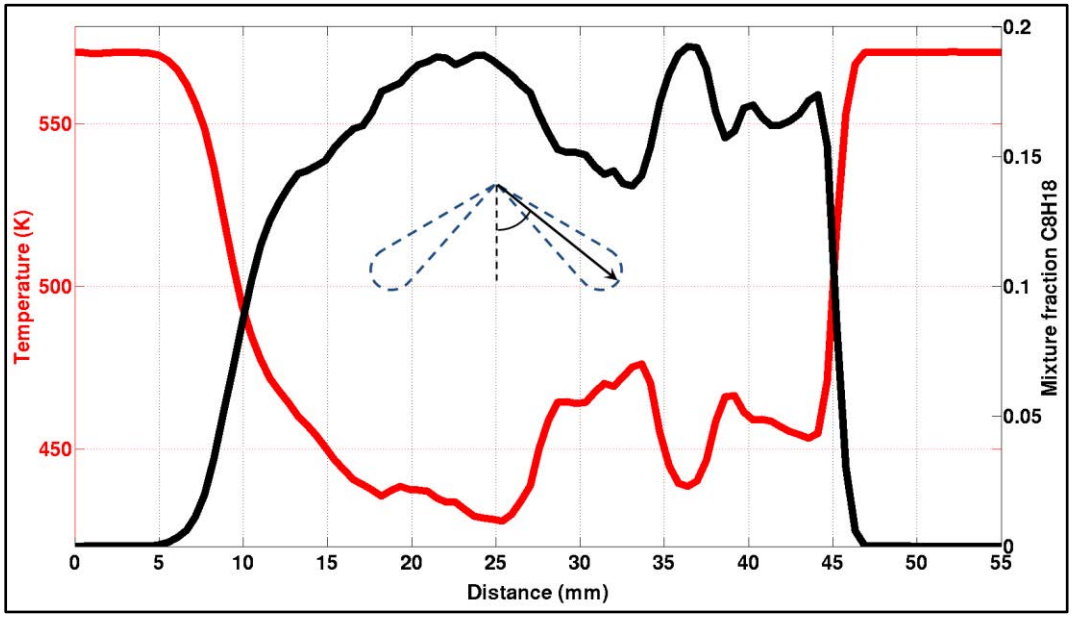

Figure 60 - Temperature (red) and Iso-octane mixture fraction (black) at 1.4 ms (I)

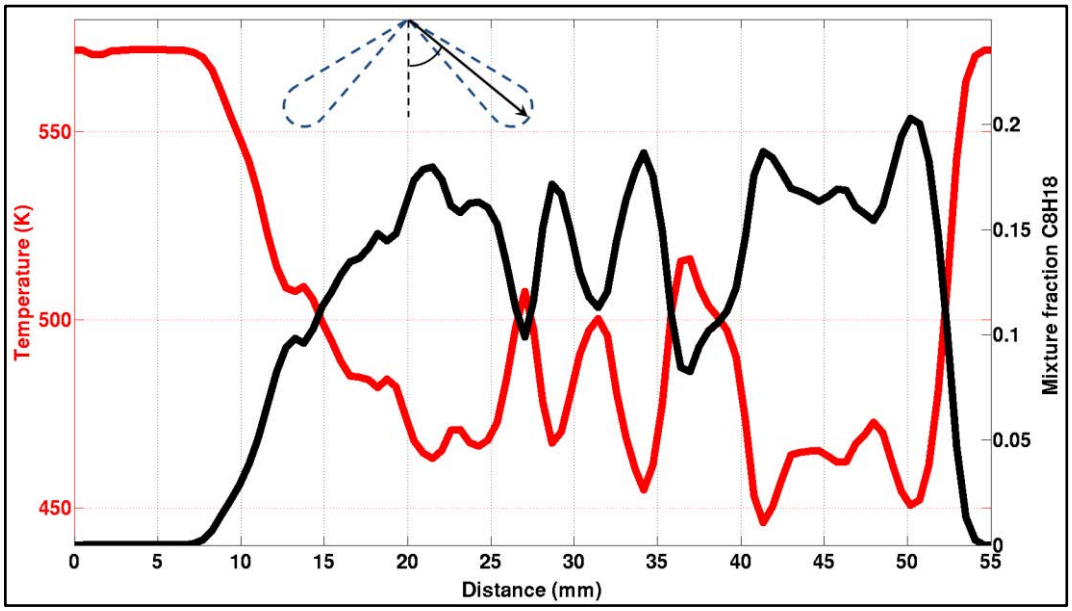

The results along the z axial direction, starting from the injector tip, are shown in figures 61, 62 and 63. At 0.6 ms after start of injection, high mixture fraction and low temperature values are found a few millimeters downstream from the injector nozzle, due to influence of the formed spray cloud. This influence is diminished further downstream, since each jet makes an angle of 40º with the axial direction. At 1.0 ms and 1.4 ms similar behavior is observed, with the difference that further in time the shapes of the curves have enough time to be dispersed within the distance from the origin.

Figure 61 - Temperature (red) and Iso-octane mixture fraction (black) at 0.6 ms (II)

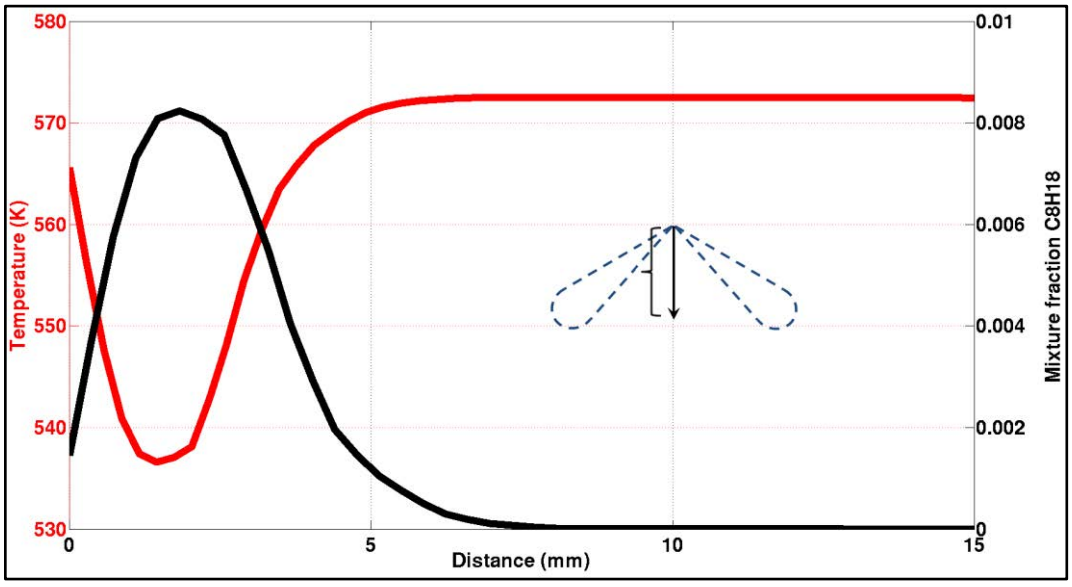

Figure 62 - Temperature (red) and Iso-octane mixture fraction (black) at 1.0 ms (II)

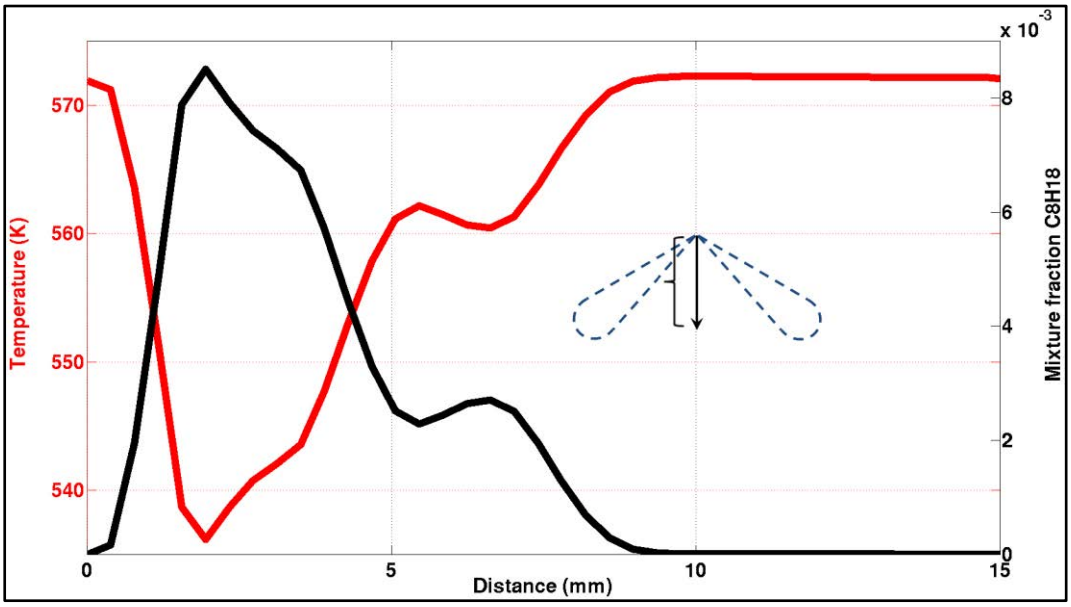

Figure 63 - Temperature (red) and Iso-octane mixture fraction (black) at 1.4 ms (II)

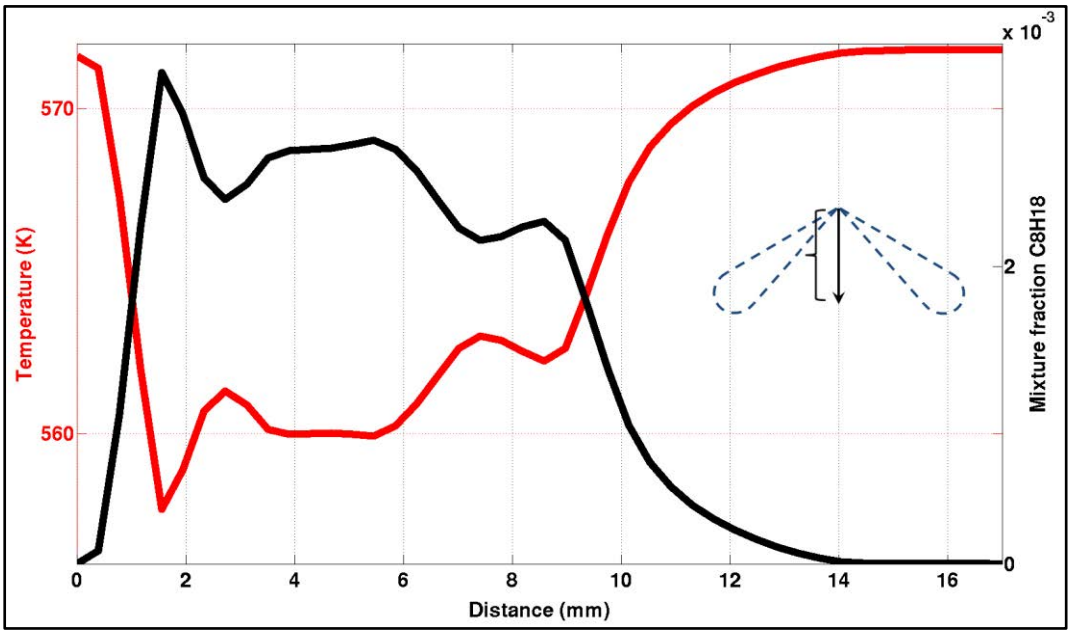

The following results are from cross-section planes at 15 mm downstream from the injector nozzle. In figures 64, 65 and 66 the values are taken from a line which cross the spray plume number 3 in the radial direction. On the other hand, figures 67, 68 and 69 aims to capture the interaction between the spray plumes 2 and 3, with a line crossing the plume center of each of them.

Figure 64 - Temperature (red) and Iso-octane mixture fraction (black) at 0.6 ms (III)

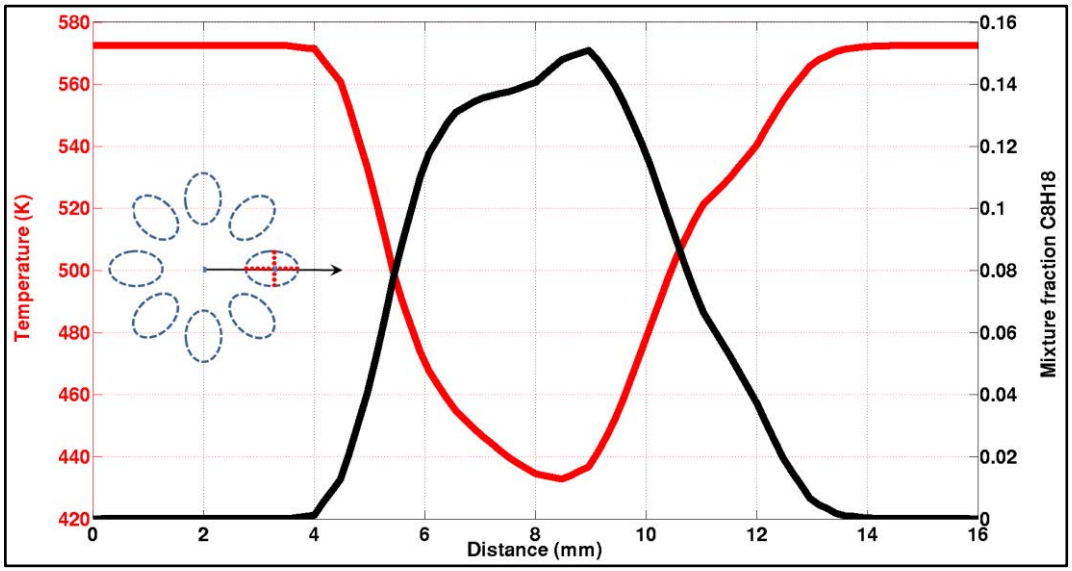

Figure 65 - Temperature (red) and Iso-octane mixture fraction (black) at 1.0 ms (III)

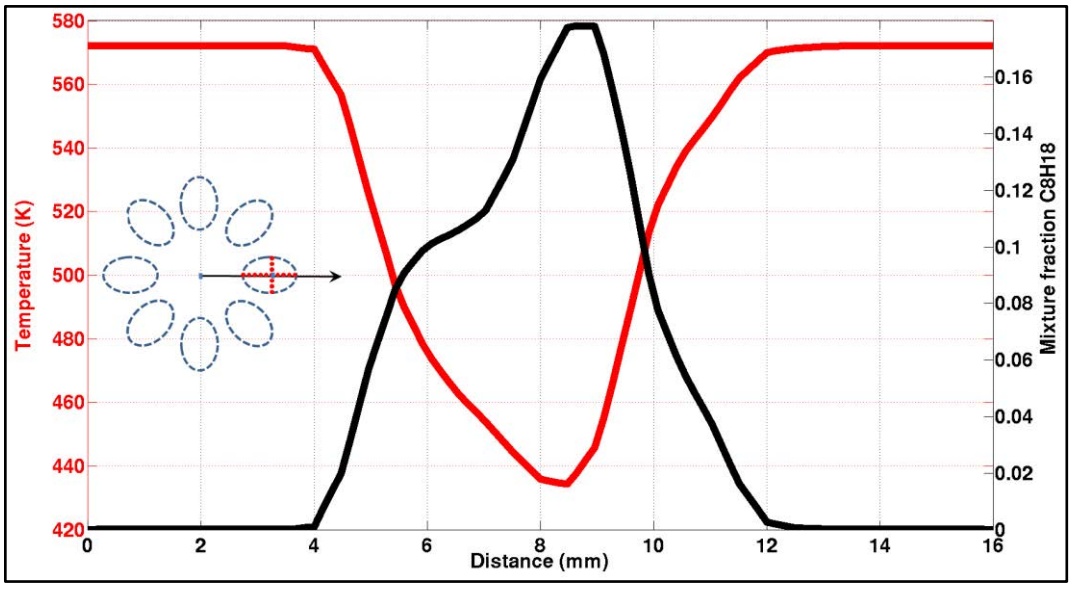

In all three instants along the spray plume 3, one can observe that gaseous iso-octane is more poorly concentrated at the spray plume frontier with the gas phase than in comparison with the middle of the jet. At 0.6 ms ASOI the shapes of both curves are more dispersed along the probe line. At 1.0 ms and 1.4 ms, however, both curves present a sharpener shape. With increasing time, the jet tip has its size increased due to diffusive and convective transport, making the difference between the highest and lowest values for both variables bigger.

Figure 66 - Temperature (red) and Iso-octane mixture fraction (black) at 1.4 ms (III)

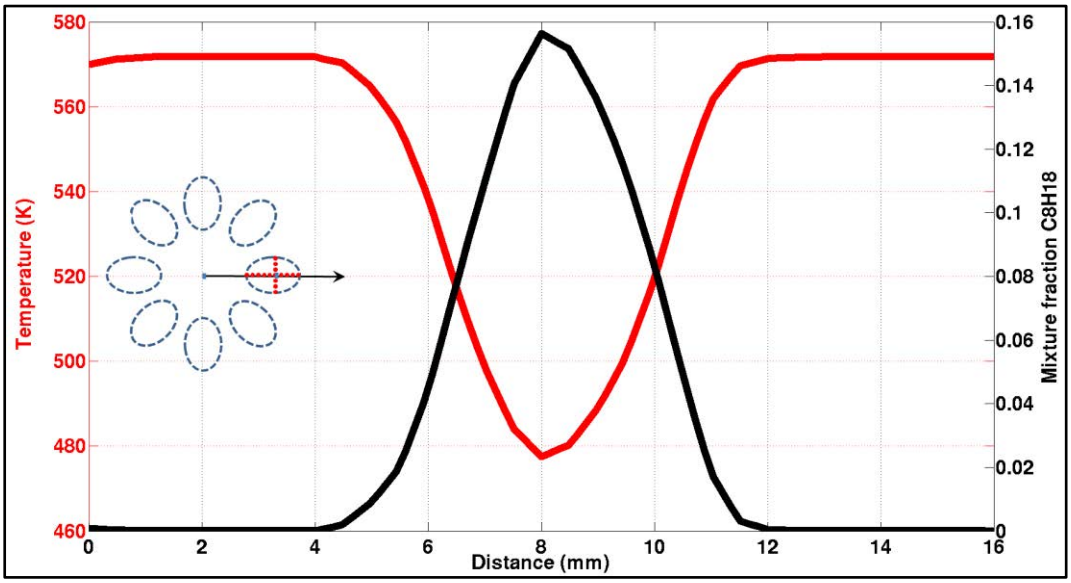

The next three figures show the interaction between spray plumes 2 and 3 from a probe line crossing both of them in a direction nearly perpendicular to the full cone spray radial direction. All of them show two distinct shapes which are related to their respective spray jet. The first shape is related to spray plume 3 and the second to spray plume 2. At 0.6 ms and 1.0 ms, both spray plumes present the highest iso-octane in the gas phase concentrated in the frontier jet/gas, with a slight decrease in the jet center. However, at 1.4 ms the maximum iso-octane mixture fraction values are found at the respective spray plume centers.

Figure 67 - Temperature (red) and Iso-octane mixture fraction (black) at 0.6 ms (IV)

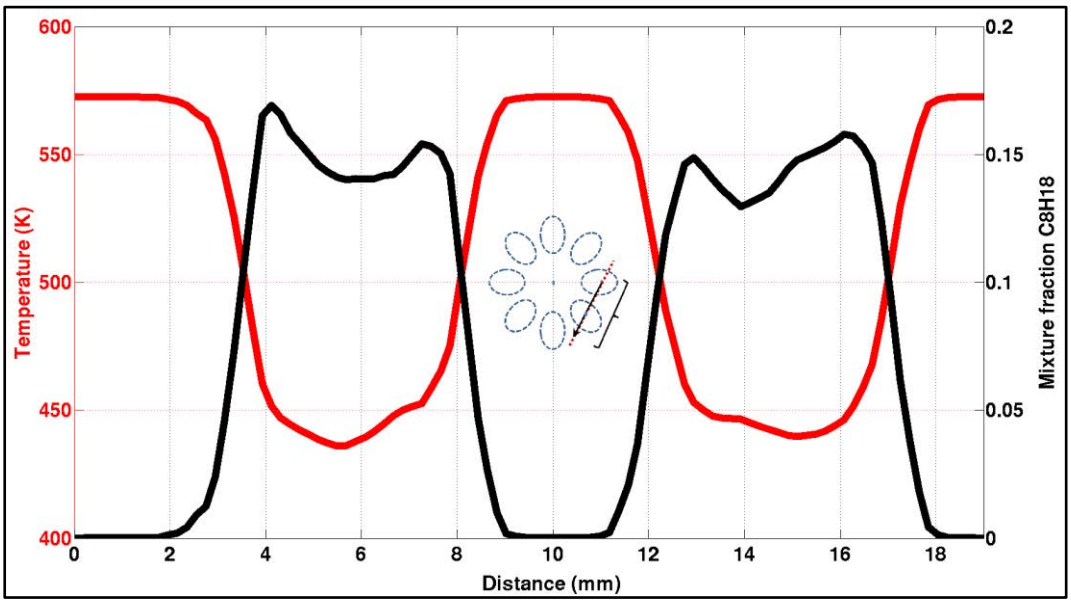

Figure 68 - Temperature (red) and Iso-octane mixture fraction (black) at 1.0 ms (IV)

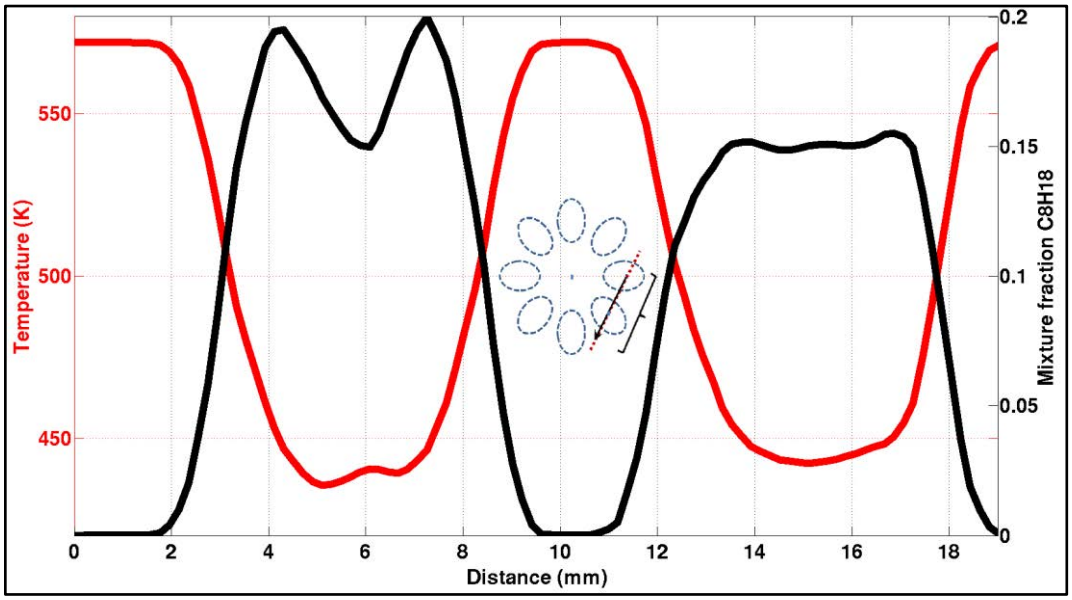

Figure 69 - Temperature (red) and Iso-octane mixture fraction (black) at 1.4 ms (IV)

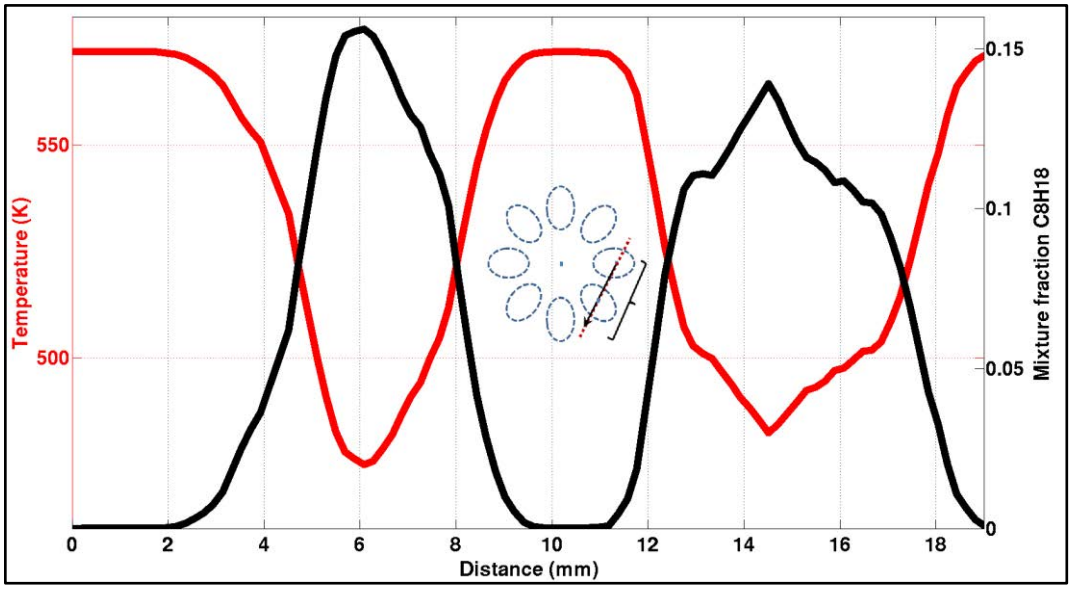

In order to close this section, a mesh sensitivity study was carried out to investigate the influence of the grid size in the spray simulations. For this, the same case was run with coarser grids of 0.75 mm and 1 mm grid sizes. Figure 70 presents the penetration curves for each one of the cases, showing that the coarser the grid is, the less deep the jet penetrates. Figure 71 shows a visualization comparing the penetration length difference in the case with grid size 0.75 mm and the one with grid size 0.5 mm at 0.6 ms ASOI.

Figure 70 – Mesh sensitivity study and comparison

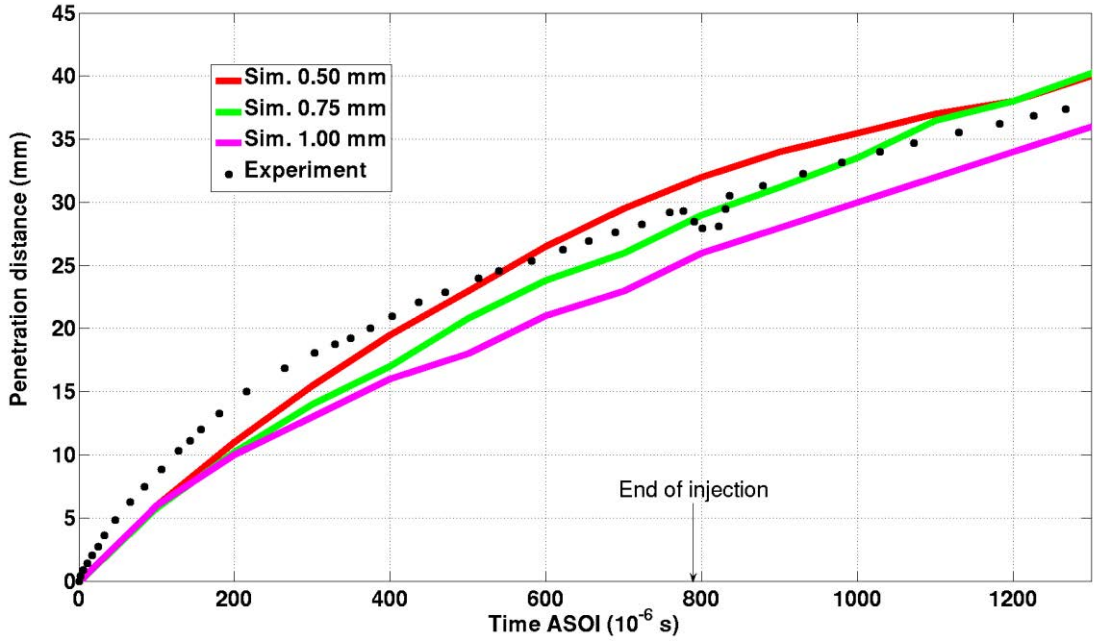

For reasons explained before, all cases under predict the penetration length of the experiment during the initial moments. The case with 0.5 mm grid (red) gets closer to the experimental value just after 0.4 ms and after 0.6 ms starts to over predict it slightly. On the other hand, the case with 0.75 mm grid reaches the experiment curve only at the end of injection at 0.78 ms, slightly over predicting it after 1 ms. The coarsest case (1mm) under predicts the penetration length over the entire simulation duration.

Figure 71 – Effect of different grid resolution on the penetration length at 0.6 ms ASOI

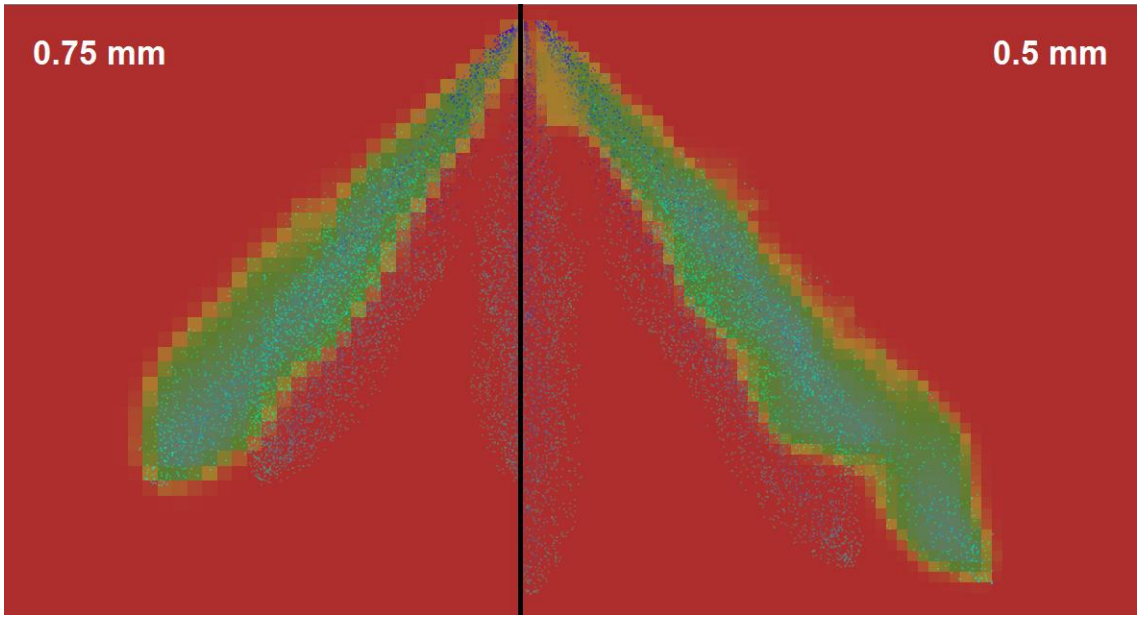

6 CONCLUSIONS

This chapter summarizes the activities conducted within this work, pointing out how the developed tasks meet the aims described in chapter 1 and presenting possibilities of future works from the limitations from the current one. Stratified-charge combustion is an increasing trend for developing state of art gasoline engines and the numerical study of such engines necessitates a solid knowledge of several particular phenomena, which alone demand already a big effort to be accomplished. This is the reason why in this work, the numerical study of the internal combustion engine (port fuel injection) was made separately from the study of fuel sprays. Furthermore, the separation of these subjects allowed a more efficient study and better validation cases for each one of them. That being said, the conclusions of this work were divided in two topics (engine and spray case) and the first possibility for future work is indeed the unification of them in the modeling of direct injection internal combustion engines.

6.1 Engine case

In-cylinder phenomena of a single cylinder spark-ignition research engine were simulated using large-eddy simulation and OpenFOAM-2.3.x. Two complete cold flow cycles were performed and a study on the influence of the top land crevice volume on the combustion efficiency was carried out. High speed flame visualization obtained by experimentalists working with the optical engine from Duisburg showed a luminous front inside the crevice volume. The capability of the present model in switching the reaction source term inside the crevice on and off allowed the investigation of this phenomenon. It was showed that the observed luminous front is indeed a wrinkled flame penetrating into the crevice volume, since its volume must be much increased in research engines to allow optical access. Comparisons from the flame propagation in the combustion chamber from large-eddy simulations against high speed visualization chemiluminescence by experiment showed a very good qualitative agreement with very similar structures in both cases.

The case studied is however not representative of real production engines, since the later present much smaller crevice volumes in order to reduce UHC emissions. Nevertheless, this work points out the importance of modeling the crevice volume on the prediction of emissions or at least the development and use of models to consider its effect. The limitations of the model are the absence of a physical ignition and chemical kinetics methodologies to evaluate engine emissions. Other limitation is the lack of resolution at the walls, fact that doesn't allow

the use of wall functions to evaluate the boundary temperatures. Within the simulations performed in this work, constant values for wall temperatures were assumed.

Therefore, this work succeeded the study of several phenomena regarding the flow and combustions of the Duisburg engine. The comparison of the flame propagation during combustion against experiments revealed very good agreement but future work must be addressed in order to add important features to the model. Important features to be added are high resolution at domain walls in order to calculate their temperatures and the evaluation of reaction mechanisms in order to evaluate emissions.

6.2 Spray case

Fuel-spray injection and its related phenomena (exchange of momentum, heat exchange and evaporation) were simulated using Lagrangian particle tracking and large-eddy simulation with OpenFOAM-2.3.x. For this, the test-case “Spray G” provided by the Engine Combustion Network was performed and the gaseous phase penetration length was validated against experiments. The penetration length obtained by the simulations showed good agreement with the experiment, although improvements should be done in order to consider non uniform concentration of particles within the spray cone and thereby improve predictions. Because this is a brand new test case from the community, other experimental results are not yet available for comparison. However, since the promising position of direct injection in order to make better engines, a lot of researchers are moving their attentions to this specific case and more reliable data should be available soon. The ReitzDiwakar model was used to represent the breakup of particles and the Rosin-Rammler CDF was employed to obtain the size distribution. Furthermore, a mesh sensitivity study was carried out in order to assess the effect of grid resolution on spray simulations, showing that the coarser the grid is, the less deep the jet penetrates.

The spray simulations conducted in this work provided experience on using the numerical tools described here and also a primary notion in order to evaluate models for the description of the complex phenomena related to fuel-spray injection. A further work in this field should consider more studies on grid dependence, effect of initial turbulence, effect of use of different boundary conditions (joint distribution in angular direction, particle size, instantaneous particle velocity), effect of numerical accuracy (TVD, CDS), effect of turbulence model, effect of grid alignment, effect of jet interaction, effect of real transport and finally effect of real evaporation.

7 REFERENCES

AHMADI-BEFRUI, B.; GOSMAN, A.D.; ISSA, R.I.; WATKINS, A.P. (1990). EPISO - An implicit non-iterative solution procedure for the calculation of flows in reciprocating engine chambers. **Computer Methods in Applied Mechanics and Engineering (79)** , 249-279.

ALKIDAS. (1999). Combustion-chamber crevices: the major source of engine-out hydrocarbon emissions under fully warmed conditions. **Progress in Energy and Combustion Science (25)** , 253-273.

AMSDEN, D.C.; AMSDEN, A. A. (1993). The KIVA Story: A Paradigm of Technology Transfer. **IEEE Transactions on Professional Communication (36)** , 190-195.

BAUMGARTEN. (2005). Mixture Formation in Internal Combustion Engines. In C. Baumgarten, **Mixture Formation in Internal Combustion Engines** (p. 294). Heidelberg: Springer.

DENT JC. (1971). A Basis for the Comparison of Various Experimental Methods for Studying Spray Penetration. **SAE paper (710571)** .

DRAKE; FANSLER; LIPPERT. (2005). Stratified-charge combustion: modeling and imaging of a spray-guided direct-injection spark-ignition engine. **Proceedings of the Combustion Institute (30)** , 2683-2691.

ENAUX, B.; GRANET, V.; VERMOREL, O.; LACOUR, C.; PERA, C.; ANGELBERGER, C.; PONSOT T. (2011). LES study of cycle-to-cycle variations in a spark ignition engine. **Proceedings of the Combustion Institute (33)** , 3115-3122.

FOX, R.W.; MCDONALD, A. T. (1998). **Introduction to Fluid Mechanics (5th edition)**. Rio de Janeiro: LTC - Livros técnicos e Científicos Editora S.A.

GALINDO, J.; TISEIRA, A.; FAJARDO P.; NAVARRO R. (2010). Coupling methodology of 1D finite difference and 3D finite volume CFD codes based on the Method of Characteristics. **Mathematical and Computer Modelling** , 1738-1746.

GORYNTSEV et al. (2010). Analysis of cyclic variations of liquid fuel–air mixing processes in a realistic DISI IC-engine using Large Eddy Simulation. **International Journal of Heat and Fluid Flow (31)** , 845–849.

GÜLDER, Ö. (1984). Correlations of Laminar Combustion Data for Alternative S.I. Engine Fuels. **SAE Technical Paper 841000** .

HEYWOOD. (1988). **Internal Combustion Engine Fundamentals**. United States of America: McGraw-Hill, Inc.

HIROYASU H., ARAI M. (1990). Structures of Fuel Sprays in Diesel Engines. **SAE-paper (900475)** .

ISHIZAWA, S. (1996). An experimental study on quenching crevice widths in the combustion chamber of a spark-ignition engine. **Proceedings of the Combustion Institute (26)** , 2605-2611.

ISSA R. I. (1985). Solution of the Implicitly Discretised Fluid Flow Equations by Operator-Splitting. **Journal of Computational Physics** , 40-65.

JASAK, H.; TUKOVIC, Z. (2004). Automatic Mesh Motion for the Unstructured Finite Volume Method. **Elsevier Science** .

KOSMADAKIS; PARIOTIS; RAKOPOULOS. (2013). Heat transfer and crevice flow in a hydrogenfueled. **Hydrogen Energy** , 7477-7489.

LIU, C.H.; VAFIDIS, C.; WHITELAW, J.H.; MARGARY, R. (1990). Flow in the coolant passages of an internal combustion engine cylinder head. **Experiments in Fluids** , 50-54.

MARSHALL W.R., RANZ W.E. (1952). **Internal Combustion Engine Modeling**. New York: Hemisphere Publishing.

MISDARIIS, A.; VERMOREL, O.; POINSOT, T. (2015). A methodology based on reduced schemes to compute autoignition and propagation in internal combustion engines. **Proceedings of the Combustion Institute** , 3001-3008.

NGUYEN T.; JANAS, P.; LUCCHINI, T.; D'ERRICO, G.; KAISER, S.; KEMPF, A. (2014). LES of Flow Processes in an SI Engine Using Two Approaches: OpenFoam and PsiPhi. **SAE International** .

PATANKAR, S V. (1980). **Numerical Heat Transfer and Fluid Flow**. New York: McGraw-Hill.

PATANKAR, S. V.; SPALDING; D. B. (1972). A calculation procedure for heat, mass and momentum transfer in three-dimensional parabolic flows. **Heat and Mass Transfer (15)** , 1787-1806.

PETERSON; REUSS; SICK. (2014). On the ignition and flame development in a spray-guided direct-injection spark-ignition engine. **Combustion and Flame** , 240-255.

RAKOPOULOS, C.D.; KOSMADAKIS, G.M.; DIMARATOS, A.M.; PARIOTIS, E.G. (2011). Investigating the effect of crevice flow on internal combustion engines using a new simple crevice model implemented in a CFD code. **Applied Energy (88)** , 111-126.

REITZ, R.D.; DIWAKAR, R. (1987). Structure of High-Pressure Fuel Sprays. **SAE Technical Paper (870598)** .

REITZ; BRACCO. (1986). Mechanisms of Breakup of Round Liquid Jets. **Enzyclopedia of Fluid Mechanics** , 233-249.

RICHARD, S.; COLIN, O.; VERMOREL, O.; BENKENIDA, A.; ANGELBERGER, C.; VEYNANTE, D. (2007). Towards large eddy simulation of combustion in spark ignition engines. **Proceedings of the Combustion Institute (31)** , 3059-3066.

THE OPENFOAM FOUNDATION. (2014). **Open Foam User's guide**.

VERSTEEG, MALALASEKERA. (1995). **An Introduction to computational fluid dynamics - The finite volume method**. New York: Longman group Ltd.

VUORINEN, V.A.; HILLAMO, H.; KAARIO, O.; NUUTINEN, M.; LARMI, M.; FUCHS, L. (2011). Effect of Droplet Size and Atomization on Spray Formation: A Priori Study Using Large-Eddy Simulation. **Flow Turbulence Combust (86)** , 533–561.

WELLER, H. G. (1998). Application of a flame-wrinkling LES combustion model to a turbulent mixing layer. **Proceedings of the Combustion Institute (27)** , 899-907.

WENTWORTH. (1971). The Piston Crevice Volume Effect on Exhaust Hydrocarbon Emission. **Combust. Sci. Technol.** , 97-100.

WESTBROOK, C. K.; MIZOBUCHI, Y.; POINSOT, T. J.; SMITH, P. J.; WARNATZ, J. (2005). Computational combustion. **Proceedings of the Combustion Institute (30)** , 125-157.

WIERZBA A. (1993). Deformation and Breakup of Liquid Drops in a Gas Stream at Nerly Critical Weber Numbers. **Experiments in Fluids** , 59-64.

APPENDIX – Case dictionaries

Frame 1 – *ThermophysicalProperties* dictionary

```
thermoType
{
    type            hePsiThermo;
    mixture         pureMixture;
    transport       sutherland;
    thermo          janaf;
    equationOfState perfectGas;
    specie          specie;
    energy          sensibleInternalEnergy;
}
mixture
{
    specie
    {
        nMoles              1;
        molWeight       28.9;
    }

     thermodynamics
    {
        Tlow            200;
        Thigh           6000;
        Tcommon         1000;
        highCpCoeffs    ( 3.10205 0.00123963 -4.17512e-07 6.60292e-11 -3.87448e-15 -985.517 5.35187 );
        lowCpCoeffs     ( 3.58378 -0.0007269 1.66985e-06 -1.08452e-10 -4.31951e-13 -1050.53 3.11223 );
    }

    transport
    {
        As              1.67212e-06;
        Ts              170.672;
    }
}
```

Frame 2 – *combustionProperties* dictionary

```
laminarFlameSpeedBMLCorrelation  GuldersEGR;
fuel            IsoOctane;
Su              Su [ 0 1 -1 0 0 0 0 ] 0.434;
SuModel         unstrained;
equivalenceRatio equivalenceRatio [ 0 0 0 0 0 0 0 ] 1;
sigmaExt        sigmaExt [ 0 0 -1 0 0 0 0 ] 100000;
XiModel         algebraic;
XiCoef          XiCoef [ 0 0 0 0 0 0 0 ] 0.62;
XiShapeCoef     XiShapeCoef [ 0 0 0 0 0 0 0 ] 1;
uPrimeCoef      uPrimeCoef [ 0 0 0 0 0 0 0 ] 1;

GuldersEGRCoeffs
{
    Methane
    {
        W 0.422;  eta 0.15; xi 5.18; alpha 2; beta -0.5; f 2.3;
    }
    Propane
    {
```

```
        W 0.446; eta 0.12; xi 4.95; alpha 1.77; beta -0.2; f 2.3;
    }
    IsoOctane
    {
        W 0.4658; eta -0.326; xi 4.48; alpha 1.56; beta -0.22; f 2.3;
    }
}
ignite          yes;

ignitionSites
(
    {
        location        (0.0013 0.00698 0.0017);
        diameter        0.002;
        start           -45;
        duration        10;
        strength        8000;
    }
);

ignitionSphereFraction 1;
ignitionThickness ignitionThickness [ 0 1 0 0 0 0 0 ] 0.001;
ignitionCircleFraction 1;
ignitionKernelArea ignitionKernelArea [ 0 2 0 0 0 0 0 ] 0.001;
```

Frame 3 – *engineGeometry* dictionary

conRodLength	conRodLength [0 1 0 0 0 0 0] 0.161;
bore	bore [0 1 0 0 0 0 0] 0.084;
stroke	stroke [0 1 0 0 0 0 0] 0.09;
clearance	clearance [0 1 0 0 0 0 0] 0.00115;
rpm	rpm [0 0 -1 0 0 0 0] 1500;

Frame 4 – *controlDict* dictionary

applicationClass	sonicDyMEngineFoam;
startFrom	startTime;
startTime	-360;
stopAt	endTime;
endTime	-355;
deltaT	1e-5;
writeControl	adjustableRunTime;
writeInterval	5;
purgeWrite	0;
writeFormat	ascii;
writePrecision	7;
writeCompression	compressed;
timeFormat	general;
timePrecision	6;
runTimeModifiable	true;
adjustTimeStep	true;
maxCo	1;
maxDeltaT	0.25;

Frame 5 – *decomposeParDict* dictionary

```
numberOfSubdomains 96;
method          scotch;
simpleCoeffs
{
    n               (4 1 1);
    delta           0.001;
}
hierarchicalCoeffs
{
    n               (3 2 1);
    delta           0.001;
    order           xyz;
}
manualCoeffs
{
    dataFile        "cellDecomposition";
}
```

Frame 6 – *fvSolution* dictionary

```
solvers
{
    "rho.*"
    {
        solver          diagonal;
    }

    "p.*"
    {
        solver          PBiCG;
        preconditioner  DILU;
        tolerance       1e-09;
        relTol          0;
    }
    "(U|b|Su|c|Xi|ft|hau)"
    {
        solver          PBiCG;
        preconditioner  DILU;
        tolerance       1e-09;
        relTol          0;
    }
    "(e)"
    {
        solver          PBiCG;
        preconditioner  DILU;
        tolerance       1e-09;
        relTol          0;
    }

        • • •
}
PIMPLE
{
    nOuterCorrectors 2;
    nCorrectors     2;
    nNonOrthogonalCorrectors 2;
    transonic on;
    momentumPredictor yes; }
```

Frame 7 – *fvSchemes* dictionary

```
ddtSchemes
{
   default      backward;
}
gradSchemes
{
   default        Gauss linear;
}
divSchemes
{
   default        Gauss limitedLinearCrevice 1 ;
   div(phi,U)      Gauss limitedLinearMachCreviceV 1;
   div(phi,e)     Gauss limitedLinearCrevice  1;
   div(phid,p)     Gauss limitedLinearCrevice  1;
   div(phi,K)      Gauss limitedLinearCrevice  1;
   div((muEff*dev2(T(grad(U))))) Gauss linear;  // Stress Tensor in the momentum equation


   • • •
}
laplacianSchemes
{
   default        Gauss linear corrected 1;
   //Gauss linear corrected;
   laplacian(diffusivity,cellMotionU) Gauss linear corrected 1;
   laplacian(muEff,U) Gauss linear  limited 1;


  • • •
}
interpolationSchemes
{
   default        linear;
}
snGradSchemes
{
   default      corrected;
}
fluxRequired
{
   default        no;
   p;
}
```

Frame 8 – N_2 boundary conditions

```
dimensions      [0 0 0 0 0 0 0];
internalField   uniform 0.8971;
boundaryField
{
   bottom
   {   type          zeroGradient; }
   liner
   {   type          zeroGradient; }
   top
   {   type          zeroGradient; }
}
```

Frame 9 – *chem.inp* file

```
ELEMENTS
 H  O   C  N  AR
END
SPECIE
C8H18 O2 N2 CO2 H2O
END
REACTIONS // left empty because no reactions are taking place
END
```

Frame 10 – *therm.data* file

```
THERMO ALL
   200.000  1000.000  6000.000
O2               ATcT06O  2.   0.   0.   0.G   200.000  6000.000 1000.       1
 3.45852381E+00 1.04045351E-03-2.79664041E-07 3.11439672E-11-8.55656058E-16    2
 1.02229063E+04 4.15264119E+00 3.78535371E+00-3.21928540E-03 1.12323443E-05    3
-1.17254068E-08 4.17659585E-12 1.02922572E+04 3.27320239E+00 1.13558105E+04    4
N2               G 8/02N  2.   0.   0.   0.G   200.000  6000.000 1000.       1
 2.95257637E+00 1.39690040E-03-4.92631603E-07 7.86010195E-11-4.60755204E-15    2
-9.23948688E+02 5.87188762E+00 3.53100528E+00-1.23660988E-04-5.02999433E-07    3
 2.43530612E-09-1.40881235E-12-1.04697628E+03 2.96747038E+00 0.00000000E+00    4
CO2              L 7/88C   1O   2    0    0G   200.000  6000.000 1000.       1
 0.46365111E+01 0.27414569E-02-0.99589759E-06 0.16038666E-09-0.91619857E-14    2
-0.49024904E+05-0.19348955E+01 0.23568130E+01 0.89841299E-02-0.71220632E-05    3
 0.24573008E-08-0.14288548E-12-0.48371971E+05 0.99009035E+01-0.47328105E+05    4
H2O              L 5/89H   2O   1    0    0G   200.000  6000.000 1000.       1
 0.26770389E+01 0.29731816E-02-0.77376889E-06 0.94433514E-10-0.42689991E-14    2
-0.29885894E+05 0.68825500E+01 0.41986352E+01-0.20364017E-02 0.65203416E-05    3
-0.54879269E-08 0.17719680E-11-0.30293726E+05-0.84900901E+00-0.29084817E+05    4
C8H18             P 4/85C  8.H 18.   0.   0.G   200.000  6000.000 1000.       1
 2.09430708E+01 4.41691018E-02-1.53261633E-05 2.30544803E-09-1.29765727E-13    2
-3.55755088E+04-8.10637726E+01 1.25245480E+01-1.01018826E-02 2.21992610E-04    3
-2.84863722E-07 1.12410138E-10-2.98434398E+04-1.97109989E+01-2.51067110E+04    4
END
```

Frame 11 – *sprayCloudProperties* dictionary I

```
    injectionModels
    {
        model1
        {
            type            coneNozzleInjection;
            SOI             0;
            massTotal       1.25e-6;
            parcelBasisType mass;
            injectionMethod disc;
            flowType        flowRateAndDischarge;
            Pinj            constant    20e6;
            outerDiameter   0.165e-3;
            innerDiameter   0;
            duration        0.78e-3;
            position        ( -0.7372e-3 0 -1e-3 );
            direction       ( -0.642788 0 -0.766044 );
            parcelsPerSecond 20000000;
            flowRateProfile table
```

```
        (
            (0              0)
            (0.78e-3        1)
            (0.781e-3       0)
        );

        Cd              constant 1;

        thetaInner      constant 0;
        thetaOuter      constant 12.5;

        sizeDistribution
        {
           type         RosinRammler;

           RosinRammlerDistribution
           {
              minValue      1e-06;
              maxValue      0.00015;
              d             0.00015;
              n             3;
           }
        }
```

● ● ● **model 2, model 3 and so on**

Frame 12 – *sprayCloudProperties* dictionary II

```
dispersionModel none;
patchInteractionModel standardWallInteraction;
heatTransferModel RanzMarshall;
compositionModel singlePhaseMixture;
phaseChangeModel liquidEvaporationBoil;
surfaceFilmModel none;
atomizationModel none;
breakupModel    ReitzDiwakar ;
stochasticCollisionModel none;
radiation       off;

standardWallInteractionCoeffs
{
   type          rebound;
}

RanzMarshallCoeffs
{
   BirdCorrection  true;
}

singlePhaseMixtureCoeffs
{
   phases
   (
      liquid
      {
         C8H18            1;
      }
```

```
        );
    }

    liquidEvaporationBoilCoeffs
    {
        enthalpyTransfer enthalpyDifference;
        activeLiquids    ( C8H18 );
    }

    ReitzDiwakarCoeffs
    {
        solveOscillationEq yes;
        Cbag            6;
        Cb              0.785;
        Cstrip          0.5;
        Cs              10;
    }
}
```

Frame 13 – *thermophysicalProperties* dictionary

```
 thermoType
{
    type              hePsiThermo;
    mixture           reactingMixture;
    transport         sutherland;
    thermo            janaf;
    energy            sensibleEnthalpy;
    equationOfState perfectGas;
    specie            specie;
}

CHEMKINFile     "$FOAM_CASE/chemkin/chem.inp";

CHEMKINThermoFile "$FOAM_CASE/chemkin/therm.dat";

newFormat       yes;

inertSpecie     N2;

liquids
{
    C8H18
    {
        defaultCoeffs   yes;
    }
}
```